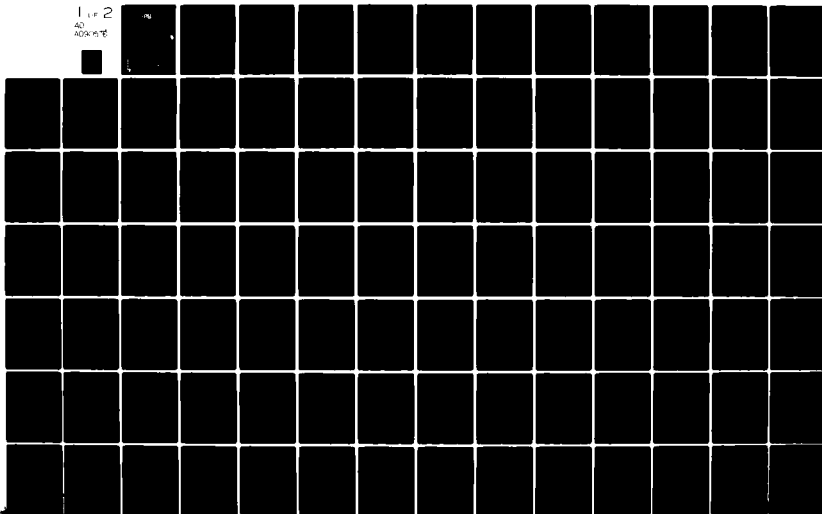


AD-A090 576

AERONAUTICAL RESEARCH ASSOCIATES OF PRINCETON INC NJ F/G 4/2  
1980 STATUS REPORT ON LOW-LEVEL, ATMOSPHERIC TURBULENCE MODEL F--ETC(U)  
JUL 80 W S LEWELLEN, D A OLIVER, R D SULLIVAN N00019-79-C-0366  
ARAP-420 NL

UNCLASSIFIED

1 of 2  
AD  
A090 576



AD A090576

**LEVEL**

1980 STATUS REPORT ON  
LOW-LEVEL, ATMOSPHERIC TURBULENCE  
MODEL FOR MARINE ENVIRONMENTS

July 1980

Final Report  
(25 June 1979 - 25 June 1980)

DTIC  
COLLECTED  
OCT 16 1980

Aeronautical Research Associates of Princeton, Inc.  
50 Washington Road, P.O. Box 2229  
Princeton, New Jersey 08540

Prepared for  
Department of the Navy  
Naval Air Systems Command  
Washington, D.C. 20361

Naval Environmental Prediction  
Research Facility  
Monterey, California 93940

Approved for Public Release  
Distribution Unlimited

80 10 6 165

APPROVED FOR PUBLIC RELEASE:  
DISTRIBUTION UNLIMITED

ARAP Report #420

(A) P-420

(12)

1980 STATUS REPORT ON  
LOW-LEVEL, ATMOSPHERIC TURBULENCE  
MODEL FOR MARINE ENVIRONMENTS .

Final Report  
(25 June 1979 - 25 June 1980)

ETIC  
OCT 16 1980

D

by  
W. S. Lewellen, D. A. Oliver, R. D. Sullivan  
and G. Sandri

Aeronautical Research Associates of Princeton, Inc.  
50 Washington Road, P.O. Box 2229  
Princeton, New Jersey 08540

July 1980

Prepared for  
Department of the Navy  
Naval Air Systems Command  
Washington, D.C. 20361

Under Contract No. N00019-78-C-0366

79

APPROVED FOR PUBLIC RELEASE:  
DISTRIBUTION UNLIMITED

SECURITY CLASSIFICATION OF THIS PAGE (When Data Entered)

REPORT DOCUMENTATION PAGE		READ INSTRUCTIONS BEFORE COMPLETING FORM
1. REPORT NUMBER ARAP Report #420	2. GOVT ACCESSION NO. ADA090576	3. RECIPIENT'S CATALOG NUMBER
4. TITLE (and Subtitle) 1980 STATUS REPORT ON LOW-LEVEL, ATMOSPHERIC TURBULENCE MODEL FOR MARINE ENVIRONMENTS		5. TYPE OF REPORT & PERIOD COVERED Final Report 6/25/79 - 6/25/80
		6. PERFORMING ORG. REPORT NUMBER
7. AUTHOR(s) W. S. Lewellen, D. A. Oliver, R. D. Sullivan, and G. Sandri		8. CONTRACT OR GRANT NUMBER(s) N00019-78-C-0366 79
9. PERFORMING ORGANIZATION NAME AND ADDRESS Aeronautical Research Associates of Princeton, 50 Washington Road, P.O. Box 2229 Inc. Princeton, New Jersey 08540		10. PROGRAM ELEMENT PROJECT, TASK AREA & WORK UNIT NUMBERS Item 0003
11. CONTROLLING OFFICE NAME AND ADDRESS Naval Air Systems Command Washington, D. C. 20361 Code AIR-370G		12. REPORT DATE July 1980
14. MONITORING AGENCY NAME & ADDRESS (if different from Controlling Office) Naval Air Systems Command Washington, D. C. 20361 Code AIR-370G		13. NUMBER OF PAGES
		15. SECURITY CLASS (of this report) Unclassified
		15a. DECLASSIFICATION/DOWNGRADING SCHEDULE
16. DISTRIBUTION STATEMENT (of this Report) standard  <b>APPROVED FOR PUBLIC RELEASE: DISTRIBUTION UNLIMITED</b>		
17. DISTRIBUTION STATEMENT (of the abstract entered in Block 20, if different from Report)		
18. SUPPLEMENTARY NOTES		
19. KEY WORDS (Continue on reverse side if necessary and identify by block number)		
20. ABSTRACT (Continue on reverse side if necessary and identify by block number) This report details the most recent developments to ARAP's program for computing the detailed low-level atmospheric distribution of velocity, temperature, moisture, refractive index, and the turbulent variances of these quantities. Model modifications discussed include the incorporation of an anisotropic length scale and the investigation into the continuation of a simpler integral model. Model calculations show the improved predictions of horizontal turbulent variances made possible by the		

DD FORM 1 JAN 73 1473 EDITION OF 1 NOV 65 IS OBSOLETE

SECURITY CLASSIFICATION OF THIS PAGE (When Data Entered)

SECURITY CLASSIFICATION OF THIS PAGE(When Data Entered)

anisotropic scale formulation, and provide for comparisons with the results of NEPRF's model calculations.

SECURITY CLASSIFICATION OF THIS PAGE(When Data Entered)

## TABLE OF CONTENTS

I. INTRODUCTION	1
II. BACKGROUND	1
III. MODEL DEVELOPMENTS	3
A. Incorporation of Two Scales	3
B. Comments on an Integral Model Based on the Second-Order Closure Equations	4
IV. COMPARISONS BETWEEN THE MODEL PREDICTIONS OBTAINED FROM DR. BURK'S CURRENT MODEL AT NEPRF AND ARAP'S ONE-DIMENSIONAL MODEL	7
V. RECOMMENDATIONS	22
REFERENCES	31
APPENDIX A: Incorporation of an Anisotropic Scale into Second-Order Closure Modeling of the Reynolds Stress Equation	33
APPENDIX B: Transport of Water Vapor through the Atmospheric Boundary Layer	69
APPENDIX C: Micrometeorological Applications of a Second-Order Closure Model of Turbulent Transport	111

Accession For	
NTIS GRA&I	<input checked="" type="checkbox"/>
DTIC TAB	<input type="checkbox"/>
Unannounced	<input type="checkbox"/>
Justification	
By	
Distribution/	
Availability Codes	
Avail and/or	
Dist	Special
A	

## I. INTRODUCTION

This report details the progress made by ARAP over the past year towards the development of a computer model for determining the detailed low-level atmospheric distributions of velocity, temperature, moisture, refractive index, and the turbulent variances of these quantities for marine environments. Since low-level clouds or fog are a frequent occurrence in the marine boundary layer, the prediction of the formation, evolution, and dissipation of these features is a necessary integral part of the desired model. In addition to appropriately modeling the turbulent transport of momentum, heat, and moisture, this necessitates the incorporation of the physics of thermal radiation and moisture change of phase into the boundary layer dynamics.

In the next section we give a very brief review of our research program in marine boundary layer modeling. This is followed by a discussion of model developments and model calculations performed over the period of this contract. Three papers prepared for publication during this period are incorporated as Appendices A, B and C.

## II. BACKGROUND

ARAP's approach to the problem of modeling the atmospheric boundary layer for marine environments has been to use the invariant second-order closure model of turbulence developed by Dr. Coleman duP. Donaldson and his associates at ARAP over the past few years. The fundamentals of this approach are given in Reference 1. A review of the status of this model as applied to a wide variety of turbulent flow problems is given in Reference 2. Particular applications of the model as applied to atmospheric problems, including comparisons with experimental data, are documented in References 2-6.

Reference 7 is a technical report detailing the model development, sample calculations, and verification comparisons made under our initial contract. It describes the addition of humidity and the second-order turbulence correlations involving humidity as variables to our dry atmospheric boundary layer program previously developed for the Environmental Protection Agency. Using the predicted distributions of temperature, humidity, and pressure, a calculation of the modified refractive index,  $M$ , was incorporated in the program. Local minimums in the  $M$  distribution with respect to altitude directly indicate the presence of a radar duct. Since we are predicting the second-order correlations between the turbulent fluctuations in temperature and humidity as well as the average scale of the turbulence, we have

available the information to also compute the structure of the fluctuations in refractivity.

Reference 7 includes the results of several sample calculations; e.g.: (a) a sample calculation using output from FNWC (supplied by J. Kaitala) as upper and surface boundary conditions for our boundary layer program; (b) a comparison of predicted temperature structure parameters with the observations of Wyngaard, et al. (Reference 8); (c) a calculation with boundary conditions roughly corresponding to the conditions observed in the Atlantic Tradewind Experiment by Augstein, Schmidt, and Ostapoff (Reference 9); and (d) a calculation simulating shoreline conditions for either a dry land breeze over the sea or a moist sea breeze over dry land.

The second year of the research called for two major modifications to the model described in Reference 7. These were to (a) increase the dimensions of the program to a two-dimensional, unsteady calculation to permit the prediction of shoreline conditions developing in time, and (b) to incorporate the radiative flux divergence term into the one-dimensional system of equations in a coupled manner. These developments are detailed in Reference 10.

The two-dimensional, unsteady version of the model was used to calculate the typical variation in the coastal planetary boundary layer (Reference 11). The resulting diurnal variation in the sea breeze induced by the strong stability difference in the boundary layer response over the land and that over the water produces a strong asymmetry between the sea-breeze and the land-breeze circulation patterns. In previous sea-breeze models, it was necessary to impose eddy viscosities which were a strong function of time and space to gain this asymmetry. In the present model, it was achieved without the need to introduce any new empirical information.

The incorporation of a coupled radiation model is important under stable atmospheric conditions when the comparative ratio of the divergence of radiation heat flux to that of the turbulent heat flux may reach order one. The primary coupling between the turbulent transport and radiation comes through the humidity distribution. The water vapor content has a strong influence on the long-wave radiative cooling, while the liquid water content strongly controls the short-wave radiative heating. Reference 10 describes the initial radiative model coupled into our program to simulate these effects in the boundary layer.

The third year's effort was divided between exercising our model for verification purposes, and extending its capability. The sample calculations are detailed in References 12 and 13. These sample calculations demonstrate the strong dynamic interaction between turbulent transport and thermal radiation. In general, the agreement between model predictions and field observations is encouraging.



A number of extensions to the model's capability were also made. These include: (1) the removal of the hydrostatic approximation; (2) the incorporation of condensation and radiation into the two-dimensional, unsteady model; and (3) the ability to determine the influence of particle size on the turbulent transport of aerosols. We also investigated, analytically, some of the relationships between parameters governing distinct fronts in the planetary boundary layer, as an aid toward the detailed computation of the structure of such fronts.

Probably the most important result detailed in the most recent contract report (Reference 14) was the calculation of the longitudinal roll-vortex structure which frequently characterizes the large turbulent eddies in the marine, atmospheric boundary layer. Results of this calculation are also detailed in References 15 and 16. From these results it appears that in the middle region of the mixed layer, more than half of the vertical momentum, heat, and humidity flux is carried by the large roll structure rather than the small-scale turbulence.

Limited comparisons with AMTEX and Great Lakes data are included in Reference 14 along with a detailed discussion of the field observation requirements for definitive model verification and a discussion of several improvements in the numerical techniques used.

Appendices A, B and C are three papers written during the present contract period. Appendix A is the result of the major part of our effort devoted to the incorporation of an anisotropic length scale into our boundary layer model. It is being submitted to the Journal of Fluid Mechanics. Appendix B was written for a workshop on water vapor in the atmosphere held at Vail, Colorado, in September 1979. It reviews the problem of modeling the transport of water vapor through the atmospheric boundary layer. It will be published by Academic Press later this year. Appendix C is being published as a paper in a volume on Turbulent Shear Flows resulting from the 2nd International Symposium on that subject held in London, July 1979. This is an expanded version of the paper which appeared in the Symposium proceedings and which was included as an appendix to Reference 14.

### III. MODEL DEVELOPMENTS

#### A. Incorporation of Two Scales

A major part of our effort during the current contract has been

devoted to the incorporation of an anisotropic length scale into our boundary layer model. Physically the modification amounts to recognizing that when there is a significant difference between the horizontal scale of a turbulent fluctuation and its vertical scale two modifications in the model are indicated. First, the pressure scrambling term which we have previously modeled as a simple tendency-towards-isotropy term must be broken into two terms. A term which tends to transfer energy from the component with the shorter length scale to that with the longer length scale must be added to the simple tendency-towards-isotropy term. Second, the dissipation length scale needs to be a weighted average between the two scales. The weighting we have chosen is the inverse of the cube of the respective velocity variances since the dissipation has dimensions of a velocity cubed over the length scale. As detailed in Appendix A, the modification in the model makes a major improvement in predicting the horizontal velocity variance near the surface under unstable conditions. Our standard model leaves  $\sigma_H/u_*$  as a function of  $Z/L$  in the surface layer with no direct dependence on  $Z_i/L$ . Observations, and the modified model, show that just the opposite occurs.

#### B. Comments on an Integral Model Based on the Second-Order Closure Equations

Considerable time was spent during this contract period investigating the development of a numerical model of the planetary boundary layer based on utilizing integrals of the second-order equations. The idea is to make maximum use of a few vertical grid points. To accomplish this it is necessary to position the grid where the variables show the maximum variation and/or make use of layer-averaged equations which are less sensitive to local gradients. We have attempted two different approaches to this problem. One is to introduce parameterized vertical distributions for the mean variables and turbulent correlations of interest and formally integrate the governing equations, including the Reynolds stress equations as well as conservation of mean momentum, energy and species. Preliminary results of this approach were given in our last status report (Reference 14). It shows promise, but has the inherent problem that results are sensitive to the parameterization chosen and when appropriately general vertical distributions are chosen the resulting equations become algebraically cumbersome. In essence this approach reduces the work of the computer but at the expense of the work required for the programmer. In the past year, we have attempted to modify the approach such that it shifts more of the work load back to the machine. The governing equations were transformed to a variable grid coordinate system so that the grid points utilized would remain at fixed fractions of the boundary layer as the boundary layer thickness evolves in time and space. Thus, even under meteorological conditions that lead to

vastly different boundary layer heights all of the grid points will remain useful, helping to define the boundary-layer flow. Integral conditions are used to determine the evolution of the boundary layer thickness.

Numerical tests have shown that five grid points are sufficient to quite reasonably represent a neutral planetary boundary layer when the correct boundary-layer thickness is prescribed and the bottom boundary condition is applied at  $z = 0.1\delta$  where the boundary conditions impose a matching to the logarithmic surface layer. Based on this, a technique has been formulated where a surface layer is used at the bottom of the boundary layer and an inversion layer, if necessary, added at the top so that the finite difference equations are only required to resolve the central bulk of the boundary layer. The grid points in this finite difference region are to be located at fixed fractions of  $\delta$ . The thickness  $\delta$  is to be determined by integral constraints taken across the complete boundary layer.

To this point we have only programmed the integral constraints in the 1-D, neutral case. We want to develop a completely stable algorithm for this limiting case before attacking the general problem. We have attempted several different formulations for this. Currently, the most promising is based on satisfying the integrated momentum and total kinetic energy equations. In the limiting case these integral equations may be written as:

$$\frac{dU_C}{dt} = -u_*^2 + fV_A \quad (1)$$

$$\frac{dV_A}{dt} = -V_*^2 - fU_C \quad (2)$$

$$\frac{dE_A}{dt} = 2U_g u_*^2 - D_A \quad (3)$$

with

$$U_C = \int_{z_0}^{\delta} (U - U_g) dz$$

$$V_A = \int_{z_0}^{\delta} V \, dz$$

$$E_A = \int_{z_0}^{\delta} [(U - U_g)^2 + V^2 + q^2] \, dz$$

$$D_A = \int_{z_0}^{\delta} \frac{2bq^3}{\Lambda} \, dz$$

$$u_{\star}^2 = -\overline{uw_0}$$

$$v_{\star}^2 = -\overline{vw_0}$$

The integrals are composed of a contribution from the surface layer where  $U$ ,  $V$  and  $q$  are given by the asymptotic form derived in Reference 17,

$$U = \frac{u_{\star}}{k} \ln z/z_0$$

$$V = \frac{f}{ku_{\star}} \left\{ \left[ \frac{v_{\star}^2}{f} + z_0 U_g - \frac{u_{\star}}{k} \right] \ln z/z_0 - U_g(z - z_0) + \frac{u_{\star}}{k} [z \ln z/z_0 - 2(z - z_0)] \right\}$$

$$q^2 = q_0^2 = \sqrt{32} (u_{\star}^4 + v_{\star}^4)^{1/2}$$

and a contribution from the remainder of the boundary layer where the variables are defined by the finite difference equations. With the evolution of the integrals determined by equations (1) - (3) the boundary layer thickness may be determined from the equation

$$\delta = H(U_C^2 + V_A^2)/E_A$$

when the shape parameter  $H$  is known. We have not yet found a satisfactory stable algorithm to determine  $H$  while letting it vary in response to changing conditions.

Further work is required to develop a stable model which is generalizable to the more interesting cases with temperature gradients and humidity, but we remain optimistic that the combination of integral constraints and a variable grid tied to the boundary-layer thickness will yield an efficient numerical model.

#### IV. COMPARISONS BETWEEN THE MODEL PREDICTIONS OBTAINED FROM DR. BURK'S CURRENT MODEL AT NEPRF AND ARAP'S ONE-DIMENSIONAL MODEL

Dr. S. Burk has a one-dimensional, atmospheric boundary layer model running at NEPRF which uses a second-order closure turbulence model similar to ARAP's model, but differing in some details. An attempt was made to make detailed comparisons between the predictions obtained from these models. Ideally these comparative calculations should have been carried out for conditions where reliable data on the "correct" results were available. This was done only to a quite limited extent.

The first comparison was for the case of free convection where comparison with laboratory data is available. Figures (1) and (2) show the results for the vertical and horizontal velocity variance. For our ARAP model both the 2-scale and the single-scale results are shown. The NEPRF model should more nearly agree with the single-scale result. The nearly 20% departure of NEPRF's result for the maximum value of  $\sigma_w$  from that predicted by ARAP's model, which agrees with the data, is somewhat surprising. This is particularly true since Mellor and Yamada (Reference 18) have previously reported results from their model, upon which Burk's model is based, to be in agreement with the data. The horizontal variance of both the ARAP single-scale model and the NEPRF model suffer the same deficiency at the surface.

Figure (3) compares the temperature variance for the different models with the laboratory measurements. All of the models agree reasonably with the data in the bottom two-thirds of the layer. In the neighborhood of the inversion the ARAP two-scale results came closest to the data but even it is somewhat lower than the observations. In this region a large part of the temperature fluctuation is

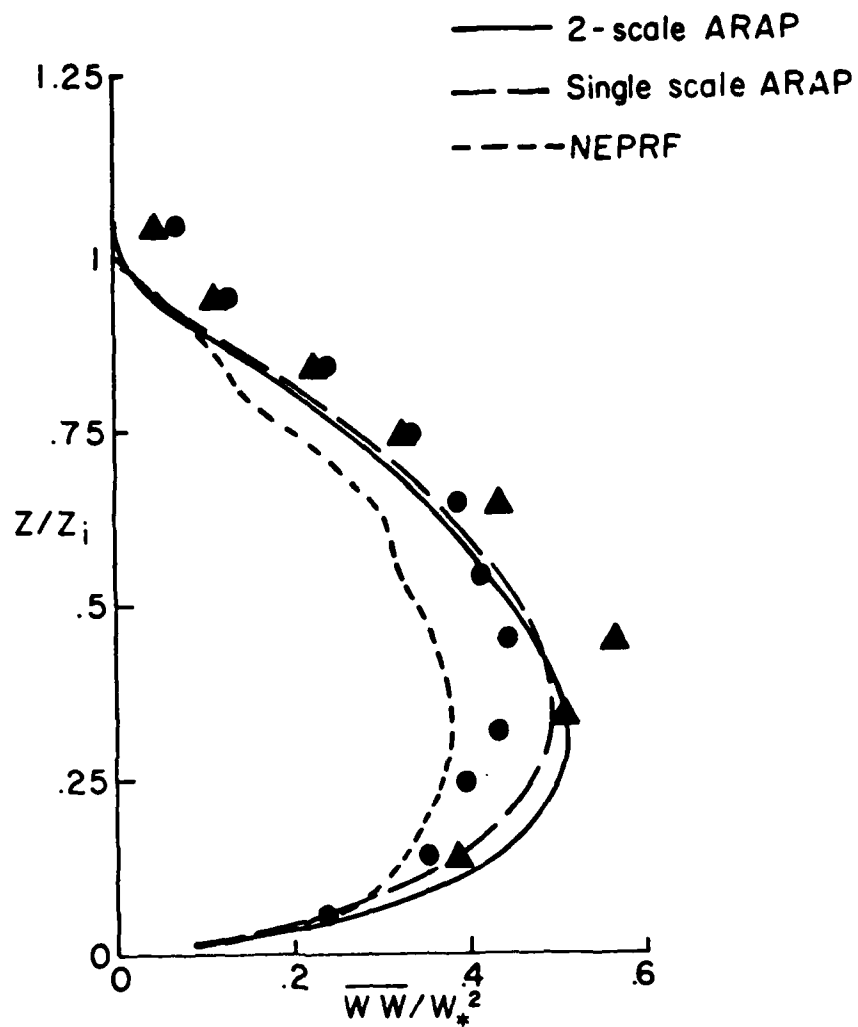


Figure 1 - Vertical velocity variance as a function of normalized height in a free convection layer as predicted by three models. (See Appendix A for a more complete description of the difference between the two ARAP models.)

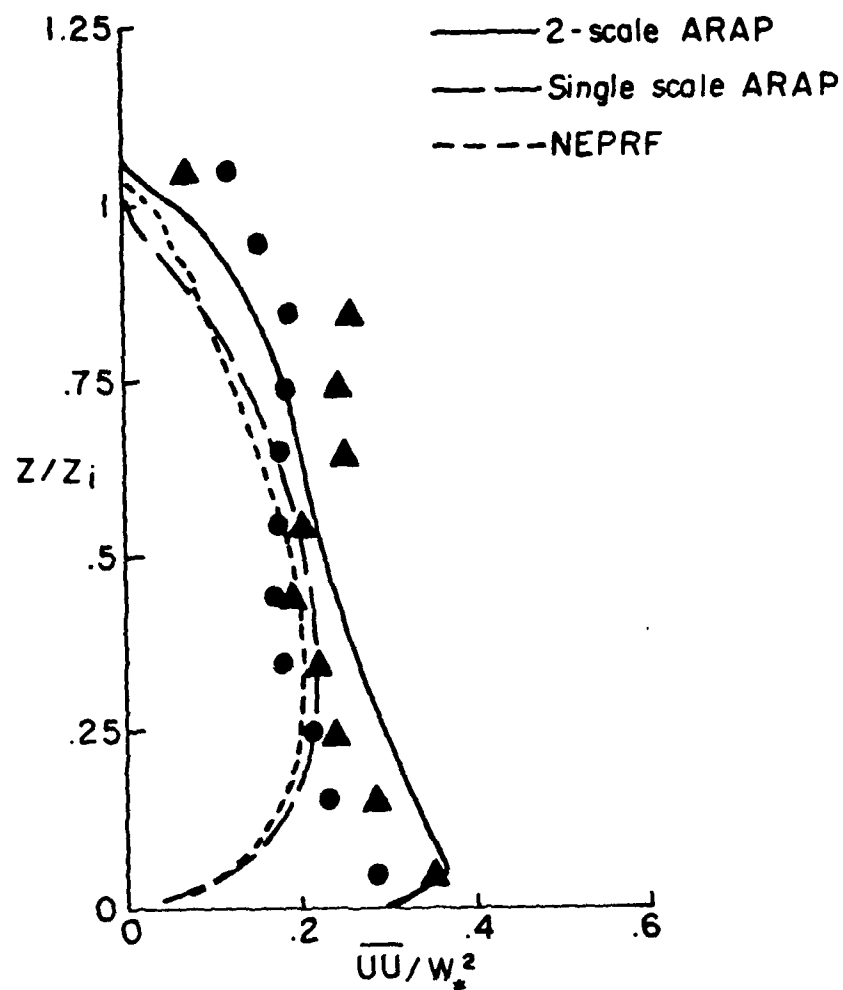


Figure 2 - Horizontal velocity variance as a function of normalized height in a free convection layer as predicted by three models. (See Appendix A for a more complete description of the difference between the two ARAP models.)

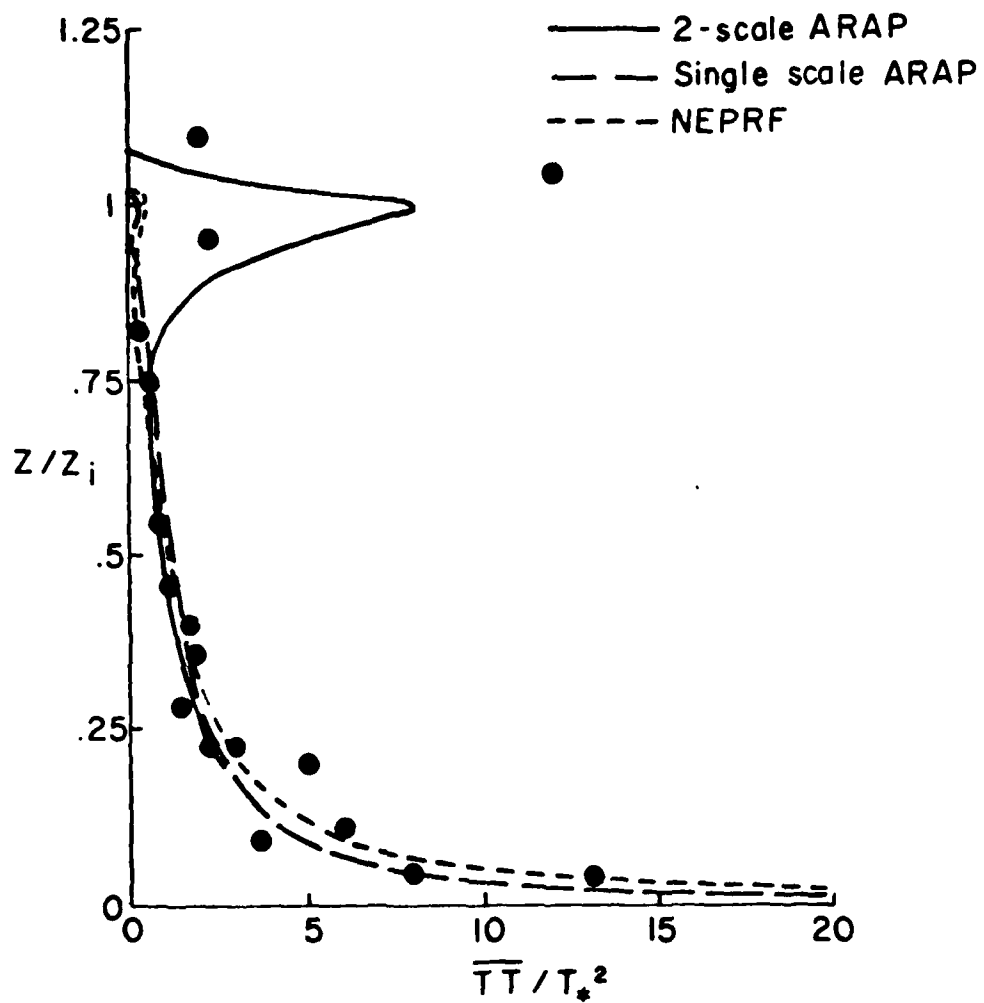


Figure 3 - Temperature variance as a function of normalized height in a free convection layer as predicted by three models. (See Appendix A for a more complete description of the difference between the two ARAP models.)



associated with internal gravity waves which cannot be adequately represented by the 1-D, turbulent model.

The other cases chosen for comparison were attempts to simulate observations for two different days for which data were obtained during the multi-platform Cooperative Experiment in West Coast Oceanography and Meteorology in 1976 (CEWCOM-76) performed off the coast of southern California from 26 September to 12 October (Reference 19). Adequate data was not available to make a rigorous comparison between model predictions and observations as was done in the free convection case. Here we will show comparisons between the two model results (the ARAP model was run only in its single-scale version in this case) and give some indication of how sensitive the results were to boundary conditions which were not completely specified by the data available to us.

Figures (4) - (15) compare the results of the two model predictions for the 3 - 4 October case. Both models are initialized with the profiles available from the 1850 LT sounding [Figure (16)]. Subsequently the sea surface time variation was input as a boundary condition to the model from the reported data. The geostrophic wind was held fixed at 5 m/sec, the upper level lapse rate was set at 2.5°K/Km and a subsidence velocity was set to vary linearly with height (proportionality factor =  $-2 \times 10^{-5} \text{ sec}^{-1}$ ). Latitude was set at 32.75° and the solar angle was set to correspond to 1850 LT with a declination of 0°. The vertical distribution of mean variables and primary turbulent variances and covariances are shown for three times (0350, 1545 and 1850) on October 4th.

The two models give generally similar results, but there are notable quantitative differences. ARAP's model results show a somewhat more rapid drop in mixed layer thickness followed by little change between the last two time breaks. The NEPRF results show a thicker mixed layer at the first time break and smaller thicknesses at the last two time breaks. The height of the inversion as predicted by the ARAP model is a somewhat better representation of the reported inversion height variation, but the mixed layer temperature variation predicted by the NEPRF model is closer to the observation. More fundamentally, both models predict clouds to occur as given by the liquid water distribution in Figure (15), while 4 October was reported as a clear day. The ARAP model predicts denser clouds. Cloud evolution is somewhat unstable in that once clouds appear they lead to increased cooling in the mixed layer through cloud top radiation. This increased cooling leads to increased cloudiness.

The radiational properties of the upper atmosphere were found to be quite important in determining the results of this boundary layer run. Figures (17) - (22) show the results obtained at 1545 when the previous run was repeated with only one change: that of the water vapor content in the total atmosphere above the top of the computational

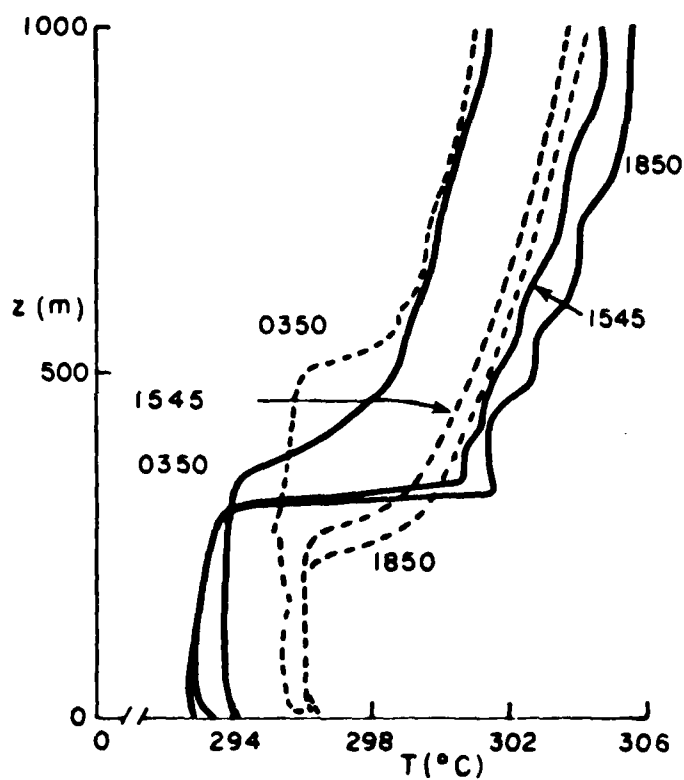


Figure 4 - Comparison between model predictions for mean virtual potential temperatures at three different times on 3 - 4 October (— ARAP model, ---- NEPRF model).

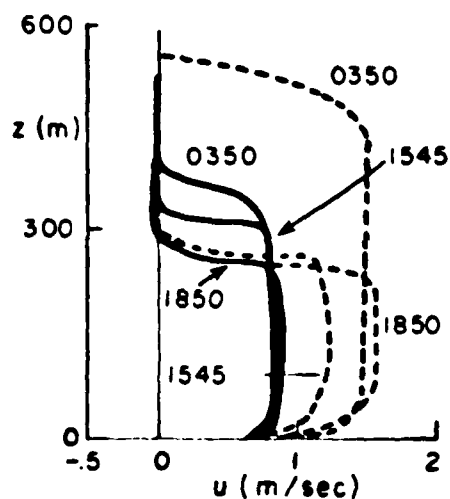


Figure 5 - Comparison between model predictions for mean wind in the geostrophic direction at three different times on 3 - 4 October (— ARAP model, ---- NEPRF model).

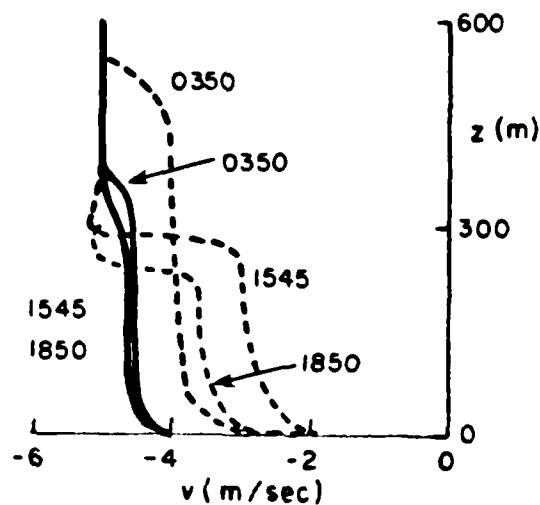


Figure 6 - Comparison between model predictions for mean wind perpendicular to the geostrophic direction at three different times on 3-4 October (— ARAP model, ---- NEPRF model).

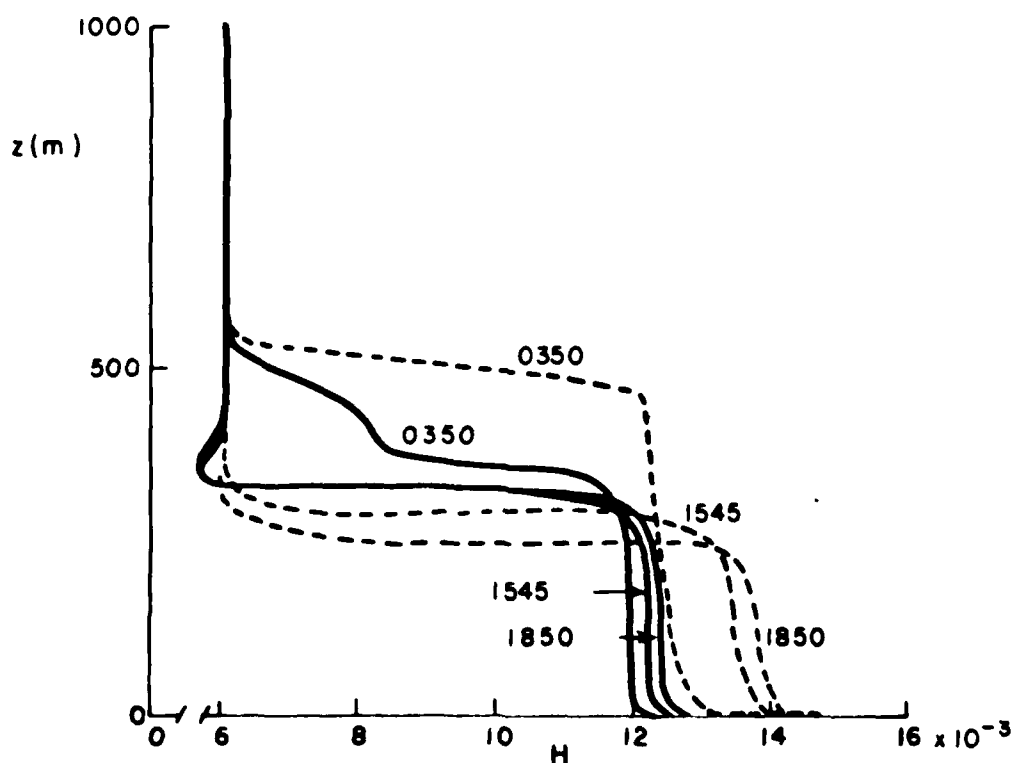


Figure 7 - Comparison between model predictions for mean total water mixing ratio at three different times on 3-4 October (— ARAP model, ---- NEPRF model).

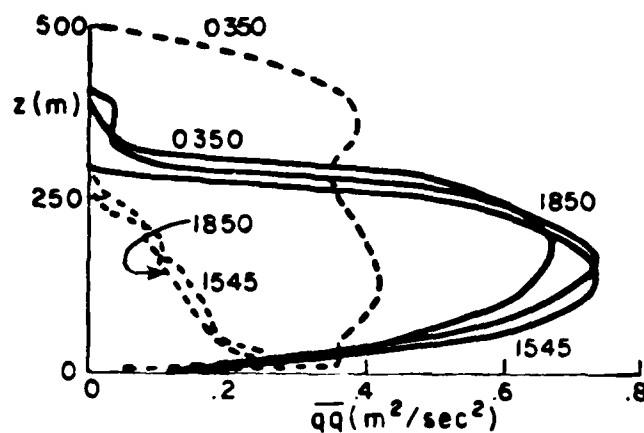


Figure 8 - Comparison between model predictions for total velocity variance at three different times on 3-4 October (— ARAP model, ---- NEPRF model).

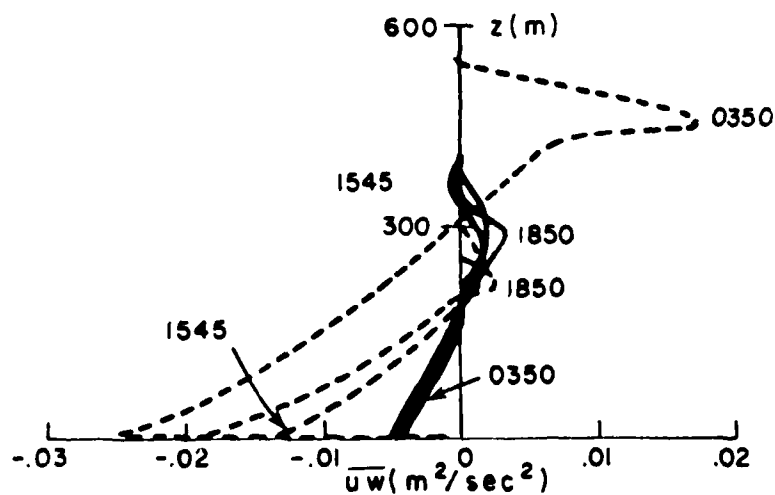


Figure 9 - Comparison between model predictions for covariance of u and w velocities at three different times on 3-4 October (— ARAP model, ---- NEPRF model).

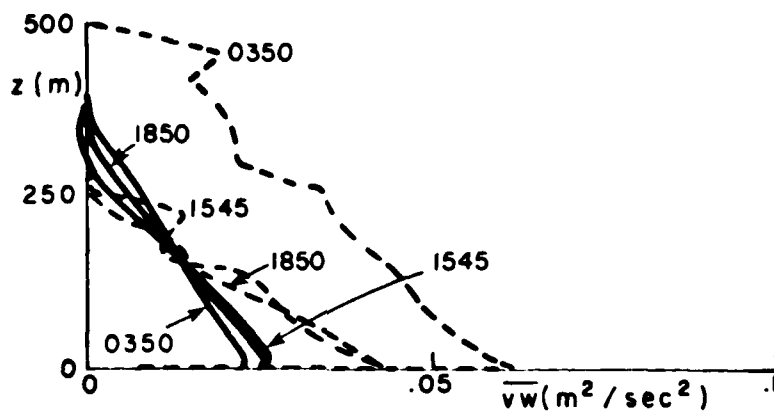


Figure 10 - Comparison between model predictions for covariance of  $v$  and  $w$  velocities at three different times on 3-4 October (— ARAP model, ---- NEPRF model).

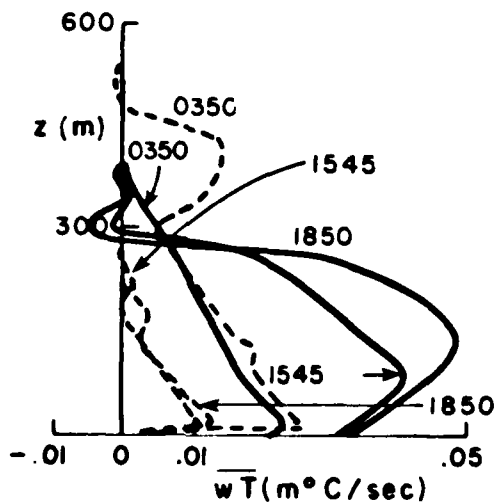


Figure 11 - Comparison between model predictions for covariance of  $w$  and the virtual potential temperature at three different times on 3-4 October (— ARAP model, ---- NEPRF model).

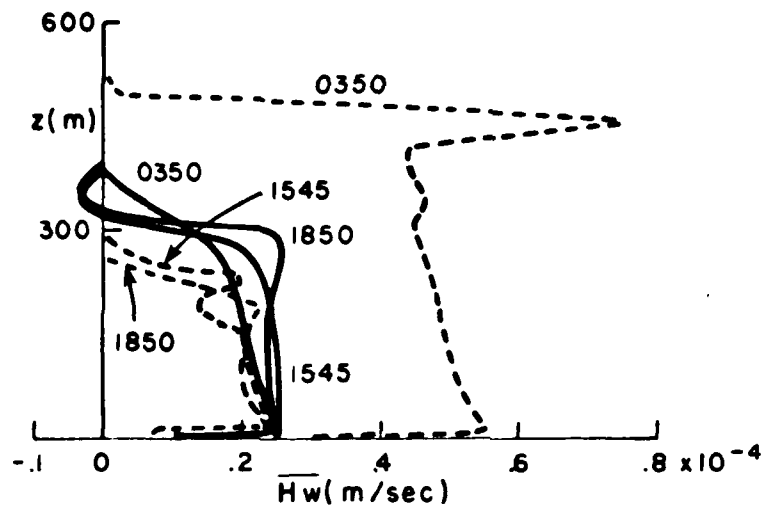


Figure 12 - Comparison between model predictions for covariance of  $w$  and the total water mixing ratio at three different times on 3-4 October (— ARAP model, ---- NEPRF model).

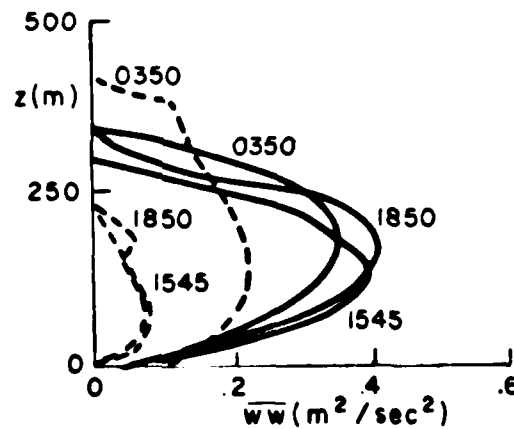


Figure 13 - Comparison between model predictions for vertical velocity variance at three different times on 3-4 October (— ARAP model, ---- NEPRF model).

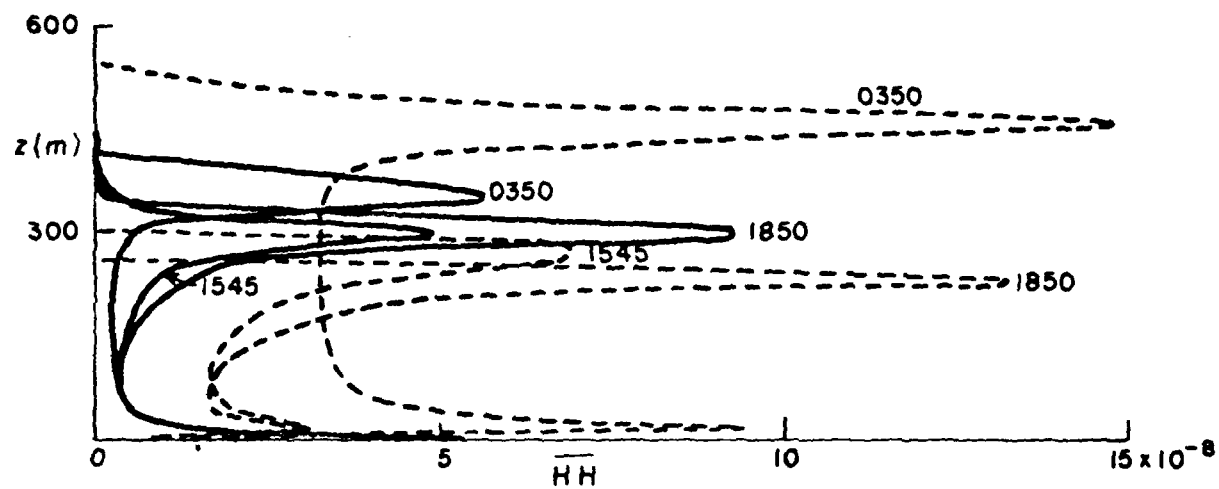


Figure 14 - Comparison between model predictions for variance of total water mixing ratio at three different times on 3-4 October (— ARAP model, ---- NEPRF model).

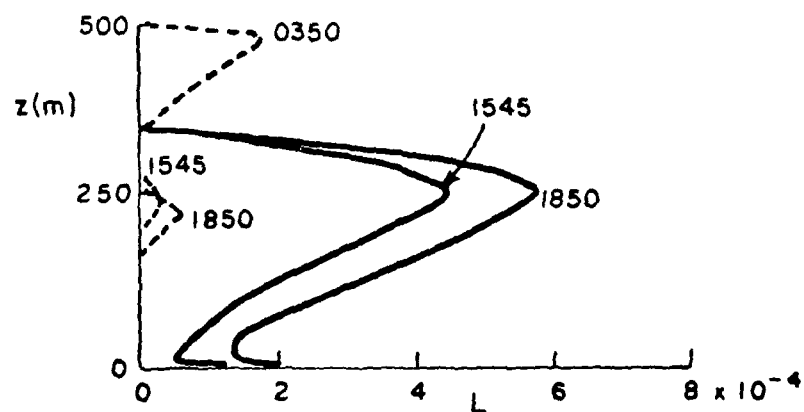


Figure 15 - Comparison between model predictions for mean liquid water content at three different times on 3-4 October (— ARAP model, ---- NEPRF model).

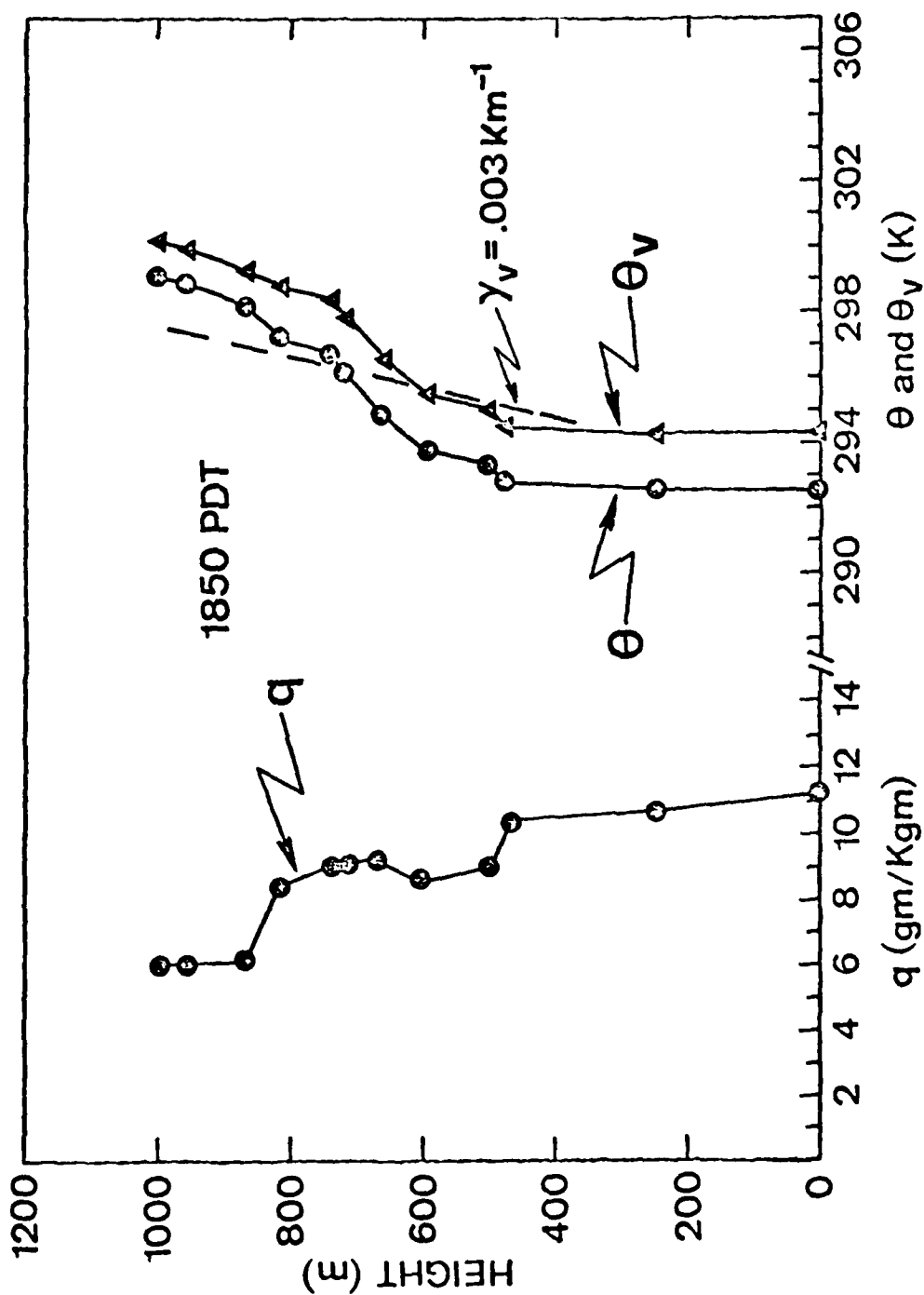


Figure 16 - Potential temperature, virtual potential and water vapor mixing ratio used to initialize the run for the predictions given in Figures 4 - 15.



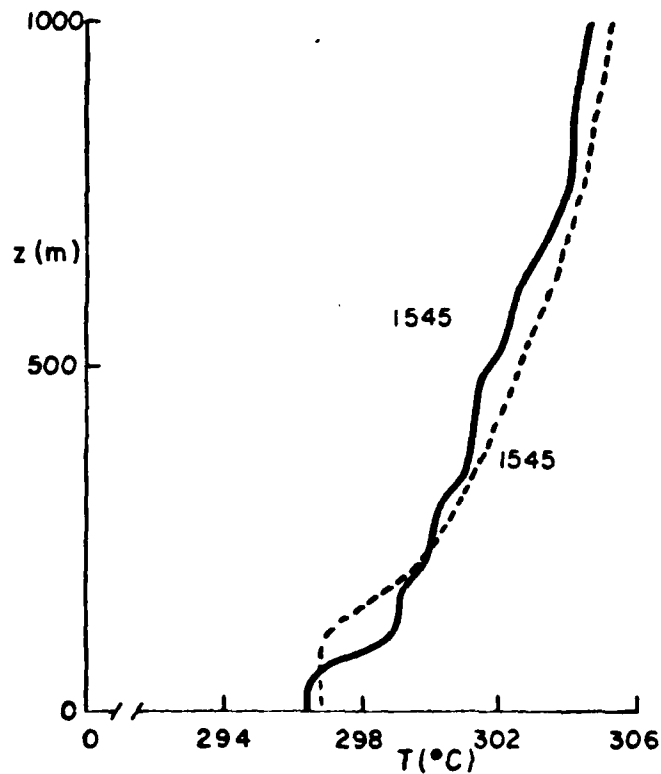


Figure 17 - Comparison between model predictions for mean virtual potential temperature at one time for the same conditions as in Figure 4, except for an increase in upper atmospheric water vapor.

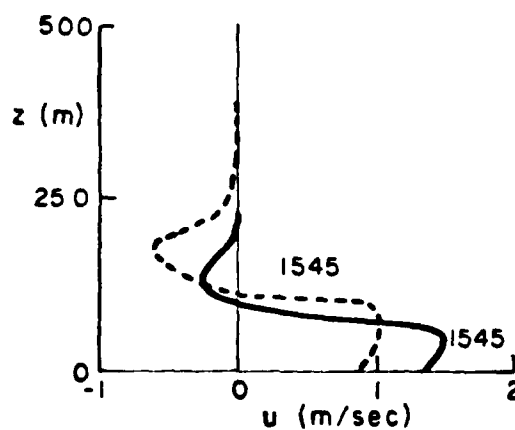


Figure 18 - Comparison between model predictions for mean wind in the geostrophic direction at one time for the same conditions as in Figure 5, except for an increase in upper atmospheric water vapor.

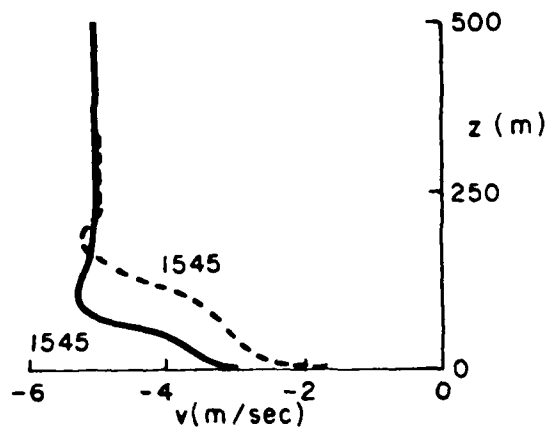


Figure 19 - Comparison between model predictions for mean wind perpendicular to the geostrophic direction at one time for the same conditions as in Figure 6, except for an increase in upper atmospheric water vapor.

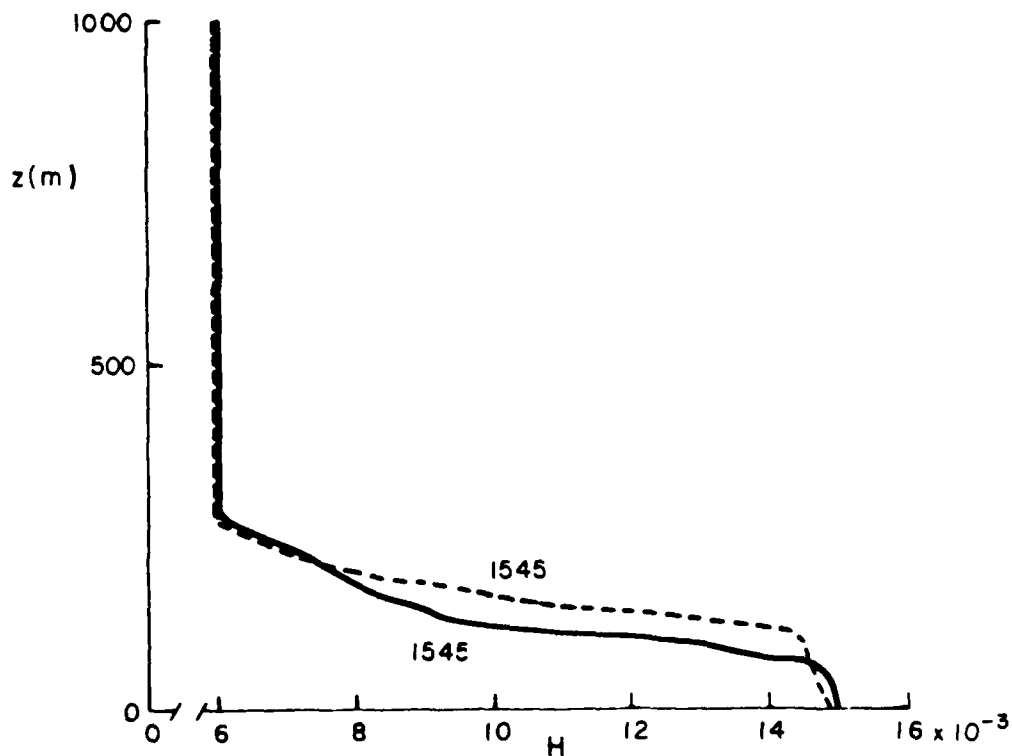


Figure 20 - Comparison between model predictions for mean total water mixing ratio at one time for the same conditions as in Figure 7, except for an increase in upper atmospheric water vapor.

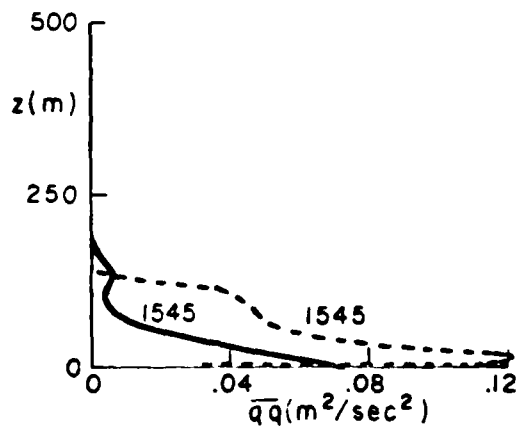


Figure 21 - Comparison between model predictions for total velocity variance at one time for the same conditions as in Figure 8, except for an increase in upper atmospheric water vapor.

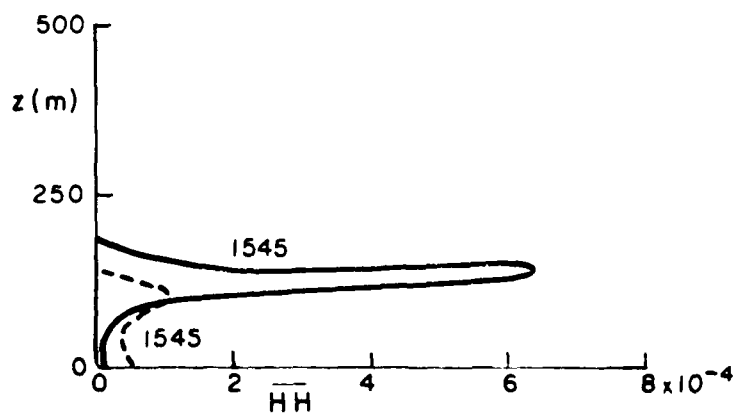


Figure 22 - Comparison between model predictions for variance of total water mixing ratio at one time for the same conditions as in Figure 14, except for an increase in upper atmospheric water vapor.

domain. A change in the parameter HU (defined as the average mass density of H<sub>2</sub>O vapor in the atmosphere above the computational domain divided by the surface density of H<sub>2</sub>O) from 10<sup>-3</sup> to 10<sup>-1</sup> essentially wipes out all cloudiness. It also reduces the inversion height by a factor of 2 to 3. We could have used this parameter to try to make the model results match the limited available data but this was not the intent. We are interested in discerning differences between the two models.

Figures (23) - (34) compare the results for 9 October with the 0350 PDT sounding used to initialize the run. In this case the subsidence was set equal to zero and the geostrophic wind was held constant at 8 m/sec while the sea surface temperature dropped 1.3°C over a 14 hour period. The upper level humidity parameter HU was held at 10<sup>-3</sup>. The two model predictions agree somewhat better in this case than in the last. Again the ARAP model leads to somewhat denser clouds, and the accompanying effects of increased cooling, increased instability, and increased turbulence. At 1610 the temperature variation shown for the ARAP model appears to be somewhat closer to the reported data with a mixed layer vertical potential temperature of approximately 289 and an inversion height of approximately 280 m.

In summary the NEPRF model and the ARAP 1-D, single-scale model give generally similar predictions. However, quite significant quantitative differences do occur, particularly in cases involving clouds. In all the cases tested, ARAP's model lead to higher values of liquid water content. The data compared with herein is not adequate to clearly distinguish which is more accurate.

## V. RECOMMENDATIONS

The current objectives of our research are threefold. They are: (1) to improve the basic physics of the model; (2) to exercise the existing model to exemplify phenomena which may be predicted to occur and to test model validity; and (3) to simplify the numerics to make the model more convenient to use. Five specific tasks have been chosen for the next contract period to provide a balanced program toward meeting these objectives.

The first task is to improve the cloud physics of the model. The current model is based on quite simple physics. Thermodynamic equilibrium is assumed to exist between liquid and gas phase water at all times. The liquid which exists is assumed to be in the form of small droplets of specified size. The droplet size is constant in

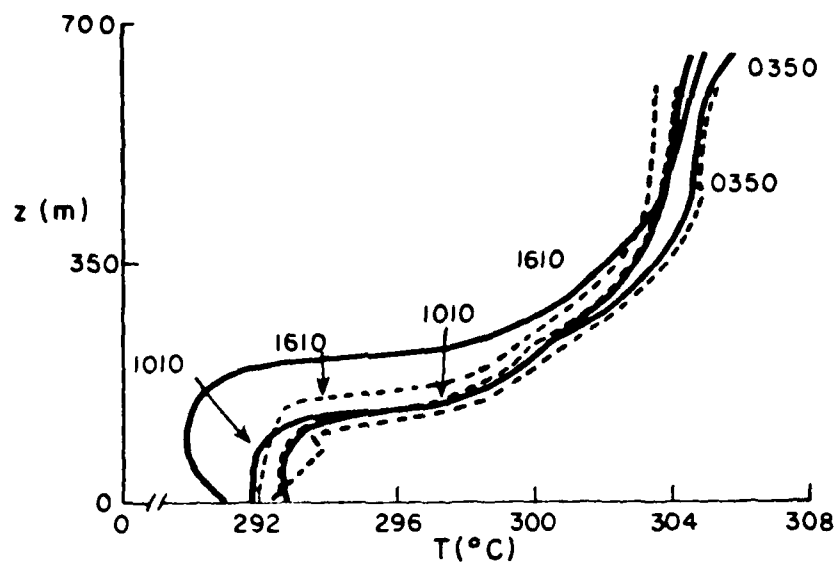


Figure 23 - Comparison between model predictions for mean virtual potential temperatures at three different times on 9 October (— ARAP model, ---- NEPRF model).

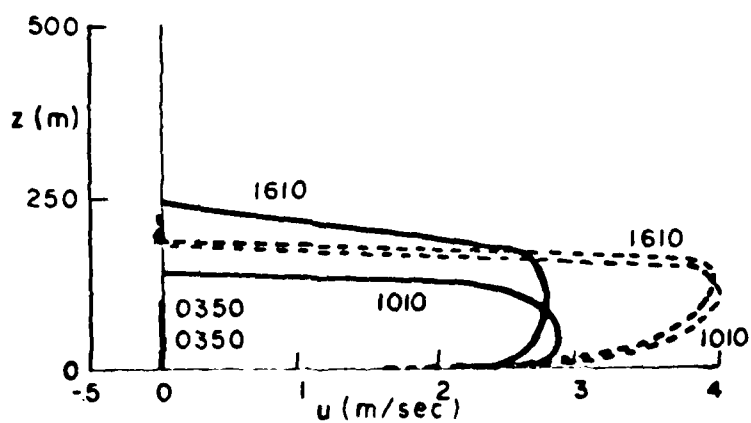


Figure 24 - Comparison between model predictions for mean wind in the geostrophic direction at three different times on 9 October (— ARAP model, ---- NEPRF model).

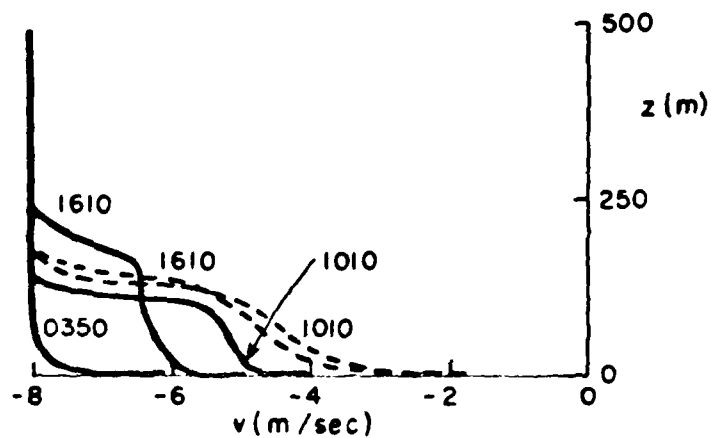


Figure 25 - Comparison between model predictions for mean wind perpendicular to the geostrophic direction at three different times on 9 October (— ARAP model, ---- NEPRF model).

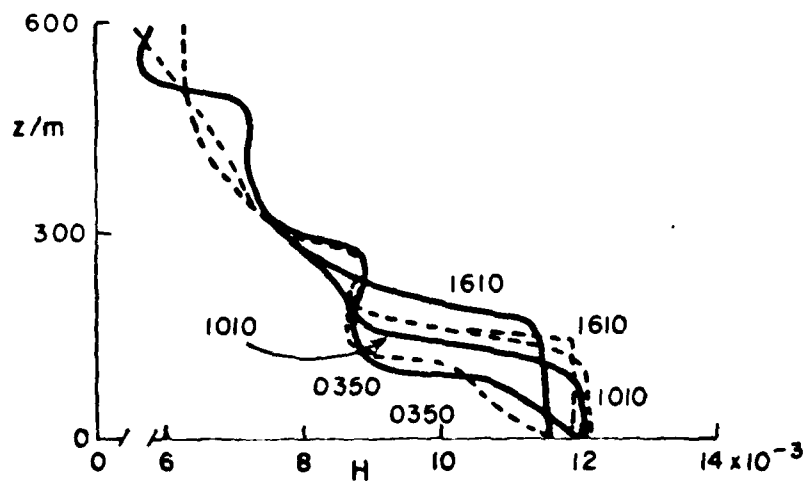


Figure 26 - Comparison between model predictions for mean total water mixing ratio at three different times on 9 October (— ARAP model, ---- NEPRF model).

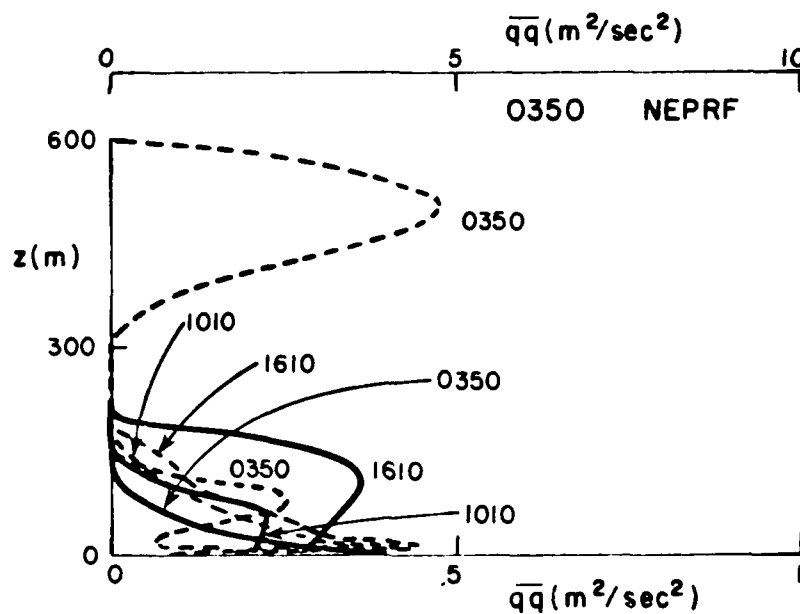


Figure 27 - Comparison between model predictions for total velocity variance at three different times on 9 October (— ARAP model, ---- NEPRF model).

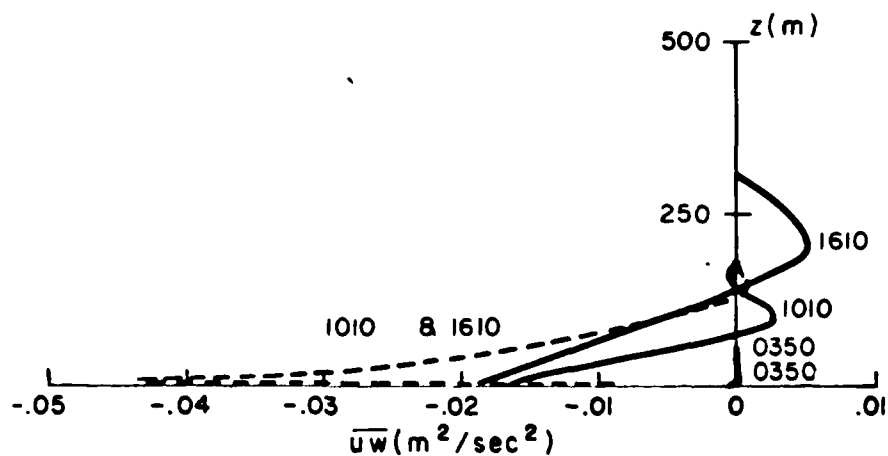


Figure 28 - Comparison between model predictions for covariance of  $u$  and  $w$  velocities at three different times on 9 October (— ARAP model, ---- NEPRF model).

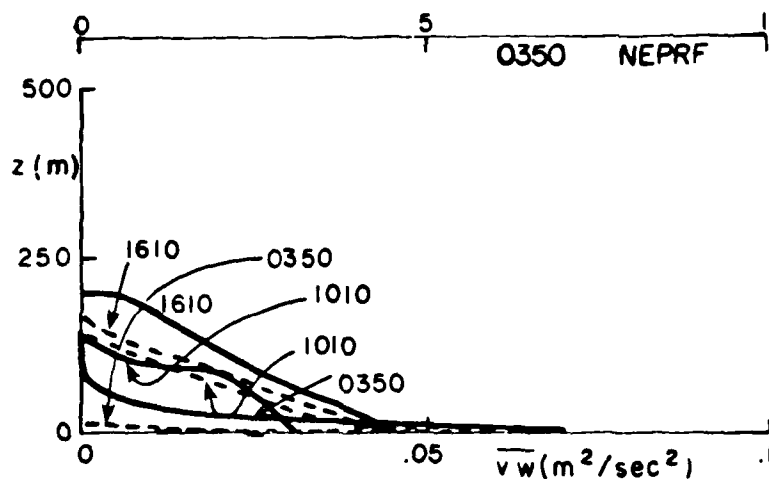


Figure 29 - Comparison between model predictions for covariance of  $v$  and  $w$  velocities at three different times on 9 October (— ARAP model, ---- NEPRF model).

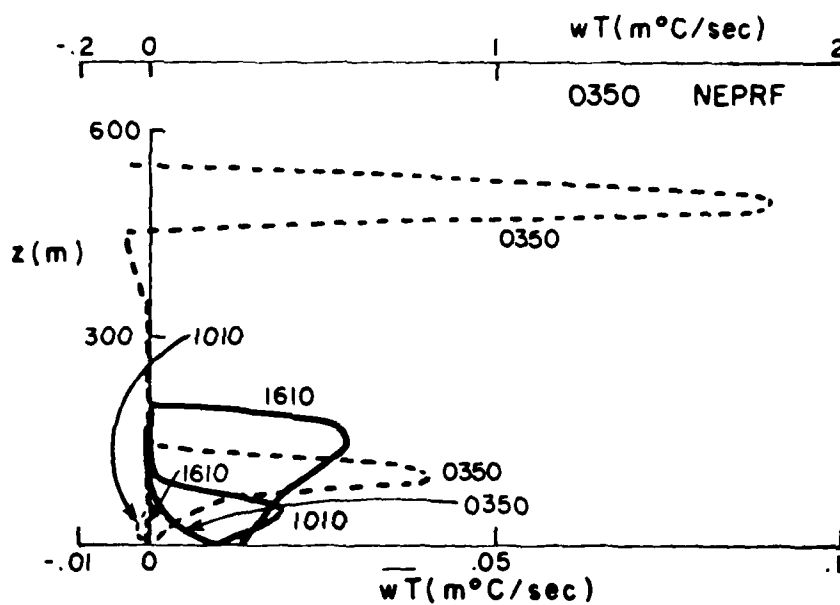


Figure 30 - Comparisons between model predictions for covariance of  $w$  and the virtual potential temperature at three times on 9 October (— ARAP model, ---- NEPRF model).



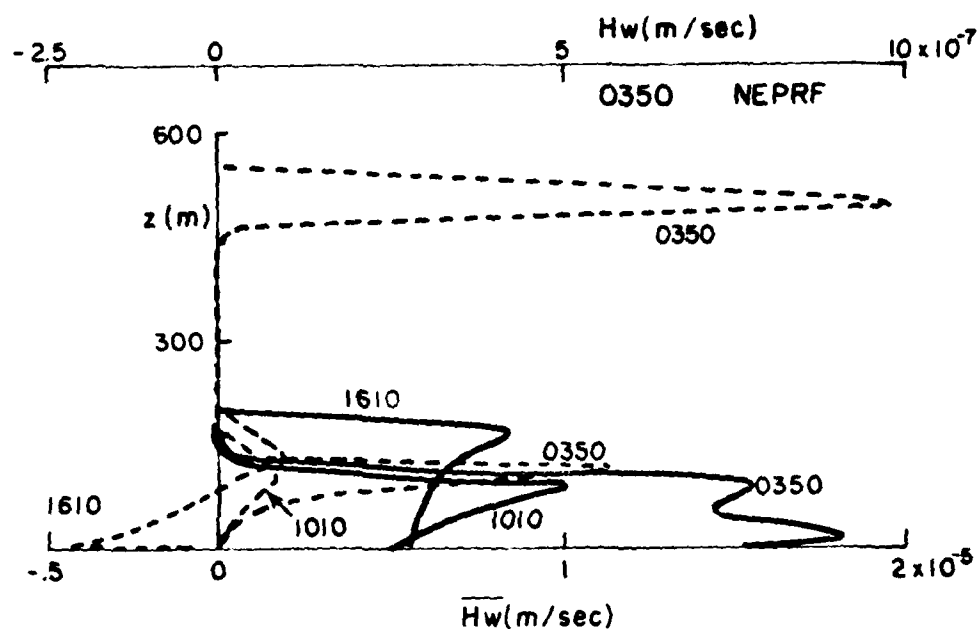


Figure 31 - Comparison between model predictions for covariance of  $w$  and the total water mixing ratio at three different times on 9 October (— ARAP model, ---- NEPRF model).

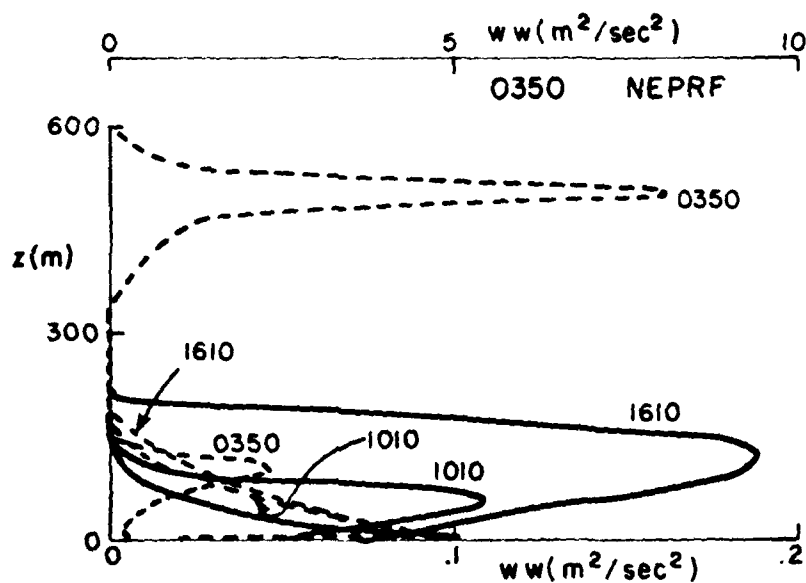


Figure 32 - Comparison between model predictions for vertical velocity variance at three different times on 9 October (— ARAP model, ---- NEPRF model).

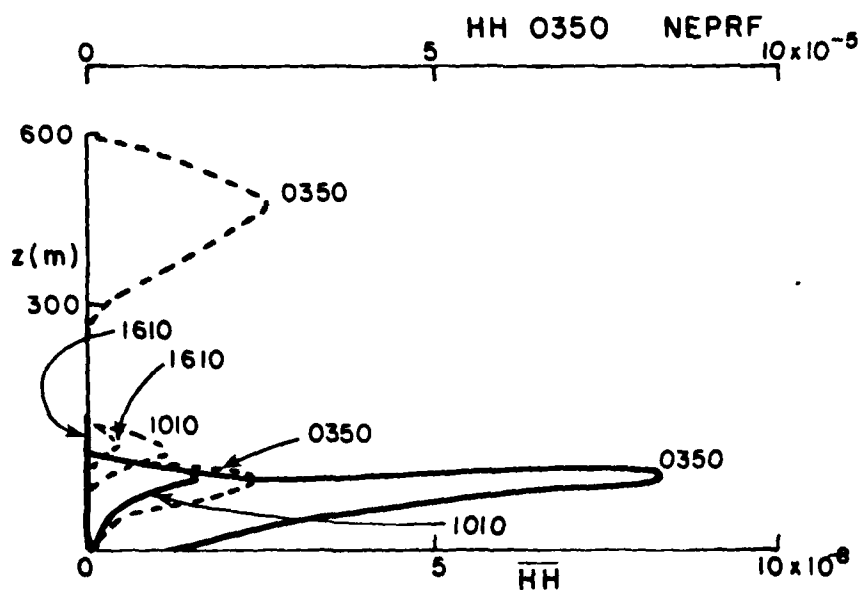


Figure 33 - Comparison between model predictions for variance of total water mixing ratio at three different times on 9 October (— ARAP model, ---- NEPRF model).

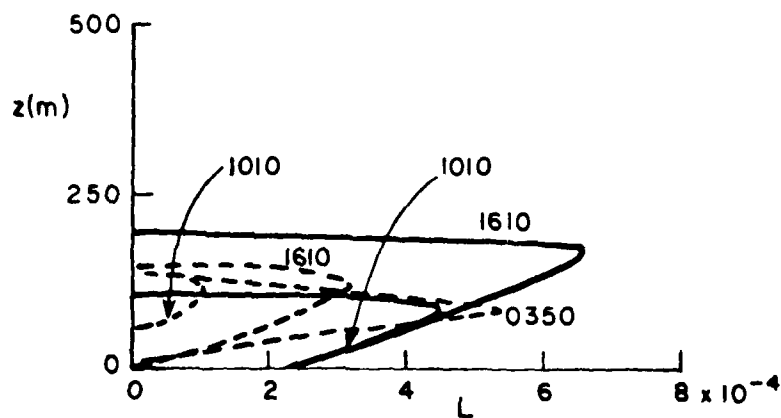


Figure 34 - Comparison between model predictions for mean liquid water content at three different times on 9 October (— ARAP model, ---- NEPRF model).

space and time. Only the number density varies as the liquid water content varies. In actuality, we would expect the droplet size distribution to be controlled by a complex interaction between the turbulent fluctuations in relative humidity and the ambient concentration of condensation nuclei. Since the droplet size distribution is such an important variable in determining visibility within a fog of given liquid water content, we would like to incorporate, at least, some droplet growth dynamics within our model. We will attempt to make use of the analytical and experimental studies performed by other NASC contractors on fog droplet dynamics. The important interaction between thermal radiation and droplet size will also be included.

The second task is to continue development of the integral model. The biggest disadvantage of our ARAP model is its numerical complexity. It requires both a considerable amount of computer time and a considerable degree of indoctrination for a new individual to make appropriate choices of all of the input variables. Our current investigation of the construction of a simpler numerical model, based on utilizing integrals of the second-order closure equations, has convinced us that this method has the potential to make our model significantly more convenient to use with little loss in accuracy. From a practical point of view, it appears that the accuracy of the simpler model will generally be controlled more by uncertainties in the meteorological inputs than in the differences in model errors between the simpler model and the full model.

The third task is to make comparisons between the results of other mixed layer models, such as Lilly's (Reference 20), and the results from both our full second-order closure model and our integral model to be developed under the second task. Several parameterized models of the unstable marine boundary layer have appeared in the literature. We propose to examine the differences predicted by the most promising of these and the predictions of our full second-order closure model. This will permit a checking of such things as the entrainment parameterization used in the models.

The fourth task is to perform specific calculations with the existing program to examine the different characteristics between warm-water fog and cold-water fog. We have used our model to perform example calculations involving fog (Reference 12), but have not made a systematic investigation of the differences between warm-water and cold-water fogs. Observations seem to suggest that warm-water fogs are found more often than cold-water fogs. Is this an anomaly of the observations or is there a fundamental bias in the physics which makes the warm-water fog more persistent? By using our model to examine the interaction between radiative and turbulent transport within a fog bank, we should be able to answer this question.

It appears appropriate at this time, after more than five years

of development, to write a critical review of our ARAP marine boundary layer model. The plan under Task 5 would be to review the model formulation and verification tests, and detail the current model's capabilities and weaknesses. This task would not lead directly towards the accomplishment of any of the three previously stated objectives but it should enhance the transferability of our research results to others.

## REFERENCES

1. Donaldson, Coleman duP.: "Construction of a Dynamic Model of the Production of Atmospheric Turbulence and the Dispersal of Atmospheric Pollutants", in Workshop on Micrometeorology, pp. 313-392.
2. Lewellen, W. S.: "Use of Invariant Modeling", in Handbook of Turbulence, edited by W. Frost, Plenum Press, 1977, pp. 237-290.
3. Lewellen, W. S., and Teske, M. E.: "Predictions of the Monin-Obukhov Similarity Functions from an Invariant Model of Turbulence", J. Atmos. Sciences, Vol. 30, 1973, pp. 1340-1345.
4. Lewellen, W. S., Teske, M. E., and Donaldson, Coleman duP.: "Turbulence Model of Diurnal Variations in the Planetary Boundary Layer", Proceedings of the 1974 Heat Transfer and Fluid Mechanics Institute, edited by L. R. Davis and R. E. Wilson, Stanford University Press, 1974, pp. 301-319.
5. Lewellen, W. S., Teske, M. E., and Donaldson, Coleman duP.: "Examples of Variable Density Flows Computed by a Second-Order Closure Description of Turbulence", AIAA J., Vol. 14, March 3, 1976, pp. 382-387.
6. Lewellen, W. S., and Teske, M. E.: "Second-Order Closure Modeling of Diffusion in the Atmospheric Boundary Layer", Boundary Layer Meteor. J., Vol. 10, 1976, pp. 69-90.
7. Lewellen, W. S., and Teske, M. E.: "Development of a Low-Level Atmospheric Turbulence Model for Marine Environments", ARAP Report No. 255, September 1975.
8. Wyngaard, J. E., Izumi, Y., and Collins, S. A.: "Behavior of the Refractive-Index-Structure Parameter Near the Ground", J. Optical Soc. of America, Vol. 61, December 1971, pp. 1646-1650.
9. Augstein, E., Schmidt, H., and Ostapoff, F.: "The Vertical Structure of the Atmospheric Planetary Boundary Layer in the Undisturbed Trade Winds Over the Atlantic", Boundary Layer Meteor. J., Vol. 6, 1974, pp. 129-150.
10. Lewellen, W. S., Oliver, D. A., Teske, M. E., and Williamson, G. G.: "Status Report on a Low-Level Atmospheric Turbulence Model for Marine Environment", ARAP Report No. 289, September 1976.
11. Lewellen, W. S., and Teske, M. E.: "A Second-Order Closure Model of Turbulent Transport in the Coastal Planetary Boundary Layer",

Presented at Conference on Coastal Meteorology, Virginia Beach, Virginia, September 21-23, 1976.

12. Oliver, D. A., Lewellen, W. S., and Williamson, G. G.: "The Interaction Between Turbulent and Radiative Transport in the Development of Fog and Low-Level Stratus", J. Atmos. Sciences, Vol. 35, 1978, pp. 301-316.
13. Lewellen, W. S., Oliver, D. A., Teske, M. E., Segur, H., and Cote, O.: "1977 Status Report on Low-Level, Atmospheric Turbulence Model for Marine Environments", ARAP Report No. 320, November 1977.
14. Lewellen, W. S., Teske, M. E., Oliver, D. A., Sheng, Y. P., and Segur, H.: "1979 Status Report on Low-Level, Atmospheric Turbulence Model for Marine Environments", ARAP Report No. 385, March 1979.
15. Teske, M. E., and Lewellen, W. S.: "Horizontal Roll Vortices in the Planetary Boundary Layer", Presented at the AMS Fourth Symposium on Turbulence, Diffusion and Air Pollution, Reno, Nevada, January 15-18, 1979.
16. Lewellen, W. S., Teske, M. E., and Sheng, Y. P.: "Micro-meteorological Applications of a Second-Order Closure Model of Turbulent Transport", Presented at the Second Symposium on Turbulent Shear Flows, Imperial College, London, July 2-4, 1979.
17. Lewellen, W. S.: "Influence of Body Forces on Turbulent Transport Near a Surface", J. Appl. Math Phys. (ZAMP), Vol. 28, 1977, pp. 825-234.
18. Mellor, G. L., and Yamada, T.: "A Turbulence Model Applied to Geophysical Fluid Problems", in Symposium on Turbulent Shear Flows, Pennsylvania State University, 1977, pp. 6.1 - 6.14.
19. Davidson, K. L., Schacher, G. E., Fairall, C. W., and Houlihan, T. M.: "Observations of Atmospheric Mixed-Layer Changes Off the California Coast (CEWCOM-76)", in Proceedings of the Second Conference on Coastal Meteorology, American Meteorological Society, 1980, pp. 63-70.
20. Lilly, D. K.: "Models of Cloud-Topped Mixed Layers Under a Strong Inversion", Quart. J. Roy. Meteor. Soc., Vol. 94, 1968, pp. 292-309.

APPENDIX A

Incorporation of an Anisotropic Scale  
into Second-Order Closure Modeling of the  
Reynolds Stress Equation

by  
W. S. Lewellen and G. Sandri

(To be submitted for publication to the Journal of  
Fluid Mechanics.)

## 1. INTRODUCTION

Modeling turbulent flow is a formidable challenge. Although the Navier-Stokes equations provide a true representation of an incompressible viscous fluid, the wide range of scales which occur at high Reynolds numbers serves to preclude using these equations to represent the flow in direct calculations except in rare instances. A variety of approaches have been offered by researchers to circumvent this problem with various degrees of success. An approach which has yielded at least some degree of success has been to extend the number of variables which describe the fluid to include the second-order turbulent correlations of the primary variables. This extended set of correlations is governed by an extended set of conservation laws, the Reynolds stress equations, obtained by taking exact second-order moments of the instantaneous Navier-Stokes equations. Second-order closure is obtained by modeling the higher-order correlations which appear in the Reynolds stress equations in terms of the describing field of first- and second-order correlations.

We will not attempt to give a review of all of the models offered in the literature to close the Reynolds stress equations. Past reviews have been given by Reynolds (1976), Launder and Spalding (1972), Lewellen (1977), Mellor and Herring (1973). Although no complete, up-to-date review of this research area is available, we believe the model offered herein is the first attempt to incorporate some influence of an anisotropic scale into a numerical model. The investigation by Hanjalic, Launder



and Schiestel (1979) of multiple-time-scale concepts is probably the most closely related work appearing in the literature.

There is a vast amount of information contained in the details of a typical turbulent motion because of the wide range of scales exhibited. The process of ensemble averaging necessarily smooths over a lot of this information. But it is a prediction of the means, variances and covariances of the primary variables which is generally most desired in engineering models. The desire is to provide a model which provides an invariant relationship between these variables for turbulent flows with different boundary conditions. It appears unlikely that relationships between the first- and second-order moments at a single point can be uniquely defined without resorting to information about two-point averages, since turbulence is a property of the macroscopic flow field rather than a local property of the fluid. Thus a critical feature of any second-order-closure model is how this macroscopic scale information is folded into the model. Two basic approaches are currently used. Either the macroscale is prescribed over the flow domain by bulk constraints, or a modeled differential equation is used with all of the nonlocal information supplied through the prescribed boundary conditions. In either case, all macroscale lengths are assumed to be related to each other by a fixed (for each model) ratio. This is tantamount to assuming that the frequency spectral distributions of all the different correlations are similar when properly normalized. This assumption, of course, is not universally valid.

The shape of the normalized spectral distributions can have significant variations. What we propose herein is a modest step towards allowing the model to use shape information. In particular, we develop a model in the next section which permits the ratio of the length scale in one direction to the length scale in the direction perpendicular to the first to vary throughout the flow. The development of the model is followed by an evaluation of the new model coefficients from data obtained in the atmospheric unstable mixed layer. This flow is chosen because of the strong variation in the ratio of the vertical length scale to the horizontal length scale which is found in the observations of the surface layer in such a flow.

## 2. MODELING CHOICES

The Reynolds stress equation for an incompressible fluid with a slightly variable density in the presence of a gravitational field may be written rigorously as

$$\begin{aligned}
 \frac{\partial \overline{u_i u_j}}{\partial t} + U_k \frac{\partial \overline{u_i u_j}}{\partial x_k} = & - \overline{u_i u_k} \frac{\partial U_j}{\partial x_k} - \overline{u_j u_k} \frac{\partial U_i}{\partial x_k} + g_i \frac{\overline{u_j \theta}}{T_0} \\
 & + g_j \frac{\overline{u_i \theta}}{T_0} + \nu \frac{\partial^2 \overline{u_i u_j}}{\partial x_k^2} - \frac{\partial}{\partial x_k} (\overline{u_k u_i u_j}) \\
 & - \frac{\partial \overline{u_i p}}{\partial x_j} - \frac{\partial \overline{u_j p}}{\partial x_i} + \frac{p}{\rho} \left( \frac{\partial u_i}{\partial x_j} + \frac{\partial u_j}{\partial x_i} \right) \\
 & - 2\nu \frac{\partial u_i}{\partial x_k} \frac{\partial u_j}{\partial x_k}
 \end{aligned} \tag{1}$$

Closure of the system of equations at this second-order level requires that the last five terms in this equations be modeled. The first three of these represent turbulent diffusion terms. We will discuss these last. We believe that the last two terms, the pressure-strain correlation and the dissipation, are generally more important.

In modeling the pressure-rate of strain correlation,  $P_{ij} = p \left( \frac{\partial u_i}{\partial x_j} + \frac{\partial u_j}{\partial x_i} \right)$ , we allow for tendency-towards-isotropy, as proposed by Rotta (1957) and generally followed in second-order-closure modeling, on the broad basis that pressure fluctuations randomize directivity since the pressure is a scalar variable. Several refinements to Rotta's tendency-towards-isotropy model have been proposed in the literature. These generally involve the use of the mean strain. We have not

included such a term in our considerations here for two reasons. First, we want the model to reduce to our previously developed single scale model (Lewellen, 1977) in the limit of an isotropic scale and, second, So and Peskin (1980) report that their tests show the previously suggested refinements to be of questionable value for a general model.

The presence of a wall or stratification certainly can introduce a bias into the fluctuations. This directionality, which can be characterized for our purposes by the normalized vector  $\hat{g}_i$  ( $\hat{g}_i \hat{g}_i = 1$ ), suggests that a tendency towards axisymmetry about  $\hat{g}_i$  can also be included in modeling the pressure-rate of strain correlation. The most general symmetric, second-rank tensor which can be formed using the normal or "vertical vector" is

$$t_{ij} = A\delta_{ij} + B\hat{g}_i\hat{g}_j \quad (2)$$

where  $A$  and  $B$  are arbitrary scalars. We note that the form given for  $t_{ij}$  can also be deduced from the assumption that  $P_{ij}$  should be modeled as a linear combination of tendency-towards-isotropy and tendency-towards-axial symmetry.

The tensor that we wish to model,  $P_{ij}$ , has zero trace as a consequence of the continuity equation

$$\frac{\partial u_i}{\partial x_i} = 0 \quad (3)$$

and thus yields no net contribution to the energy equation. Thus,  $P_{ij}$  represents only rearrangement (or scrambling) among the three energy components. We require that the model that we choose for  $P_{ij}$  should have the same property; i.e.,

$$\tau_{kk} = 0 \quad (4)$$

It follows that we have the relationship

$$3A + B = 0 \quad (5)$$

We can therefore rewrite  $\tau_{ij}$  as

$$\tau_{ij} = 2A \left( \frac{1}{2} \delta_{ij} - \frac{3}{2} \hat{g}_i \hat{g}_j \right) \quad (6)$$

A factor of two has been inserted in order to observe the identity

$$\tau_{ij} = 2A \left[ \hat{g}_i \hat{g}_j - \frac{1}{2} (\delta_{ij} - \hat{g}_i \hat{g}_j) \right] \quad (7)$$

The tensor  $\hat{g}_i \hat{g}_j$  is the projector on the vertical direction while the tensor  $\delta_{ij} - \hat{g}_i \hat{g}_j$  is the projector on the horizontal direction. Our tendency model thus has automatically the property that a source or sink acts on the vertical component of energy depending upon the sign of  $A$  and a counterbalancing sink or source acts (isotropically) on the two horizontal components of energy.

We can write our proposed model for the pressure-rate of strain correlation as

$$\begin{aligned} P \left( \frac{\partial u_i}{\partial x_j} + \frac{\partial u_j}{\partial x_i} \right) = & - \frac{1}{\tau_1} \left\{ \left( \overline{u_i u_j} - \frac{q^2}{3} \delta_{ij} \right) \right. \\ & \left. - \frac{q^2}{\tau_2} \left( \hat{g}_i \hat{g}_j - \frac{1}{2} [\delta_{ij} - \hat{g}_i \hat{g}_j] \right) \right\} \quad (8) \end{aligned}$$

To complete the modeling of this term, we must relate the two time scales to determinable characteristics of the turbulence. At this point, we also introduce the constraint that our two-scale model reduce to our standard single-scale model when the horizontal and vertical length scales are equal. At the other extreme when the vertical length scale is much smaller than the horizontal,  $\tau_1$  should be dominated by the ratio of the vertical length scale to the vertical velocity variance. An expression for  $\tau_1$ , which provides for a smooth transition between these two limiting time scales is

$$\frac{1}{\tau_1} = (1 - \xi) \frac{q}{\Lambda_H} + C_1 \xi \frac{\sigma_w}{\Lambda_V} \equiv \frac{q}{\Lambda_H} F_P \quad (9)$$

with

$$\xi = 1 - (\Lambda_V/\Lambda_H)^{2/3}$$

and

$$\sigma_w = (\hat{g}_i u_i u_j \hat{g}_j)^{1/2} \quad (10)$$

This expression introduces a new constant  $C_1$ . The exponent  $2/3$  could be left free at this point but is chosen in anticipation of the results of the expansion about  $\Lambda_V/\Lambda_H \rightarrow 0$  in the next section. The time scale for the tendency-towards-axial symmetry should depend upon how anisotropic the components of the Reynolds stress are. The form we choose is

$$\frac{1}{\tau_2} = \frac{q}{\Lambda_H} F_P \xi^* \left[ \frac{1}{3} - D \frac{\sigma_w^2}{q^2} \right] \quad (11)$$

which introduces two more constants,  $\xi^*$  and  $D$ .

Since the principal contributions to dissipation occur as a result of the small eddy motions, most researchers agree that dissipation should be modeled as an isotropic loss term. We add to this the requirement of a smooth transition between appropriate choices for the two limiting cases to take as our choice

$$\nu \left( \frac{\partial u_i}{\partial x_k} \frac{\partial u_j}{\partial x_k} \right) = \left[ (1 - \xi) \frac{q^3}{\Lambda_H} + C_2 \xi \frac{\sigma_w^{3/2}}{\Lambda_V} \right] \frac{b}{3} \delta_{ij} = \frac{bq^2}{3\tau_3} \delta_{ij} \quad (12)$$

This introduces an additional constant,  $C_2$ . We choose to hold  $b$  fixed at  $1/8$ , its previous standard value. A simpler choice for dissipation would have been to model it as proportional to  $\tau_1^{-1}$ , but this would not appear to give the correct dependence on  $\sigma_w$  in the limit of  $\Lambda_V/\Lambda_H \rightarrow 0$ .

The diffusion terms in Eq. (1) are combined and modeled simply as

$$\begin{aligned} \frac{\partial}{\partial x_k} (\overline{u_k u_i u_j}) &= \frac{1}{\rho} \frac{\partial \overline{u_i p}}{\partial x_j} - \frac{1}{\rho} \frac{\partial \overline{u_j p}}{\partial x_i} \\ &= \nu_c \frac{\partial}{\partial x_k} \left\{ \hat{g}_k \hat{g}_\ell q \Lambda_V \left[ 1 - \xi + C_1 \xi \frac{\sigma_w}{q} \right] + (\delta_{k\ell} - \hat{g}_k \hat{g}_\ell) q \Lambda_H \right\} \frac{\partial \overline{u_i u_j}}{\partial x_k} \end{aligned} \quad (13)$$

We have refrained from introducing any new model coefficients in the diffusion terms and have stuck to the philosophy of a simple transition from the previous standard model when  $\Lambda_V = \Lambda_H$  to a vertical diffusion which depends only on  $\sigma_w$  and  $\Lambda_V$  when  $\Lambda_V \ll \Lambda_H$ . Models which attempt to incorporate more of the physics of these diffusion terms have been put forward

by others, but difficulty with the accurate determination of the required model coefficients risks any real gains of introducing additional complexity at this point.

For the thermal equations, we adopt a parallel strategy. The two relevant modeled terms are the "pressure scrambling" of the heat flux

$$\left\langle T' \frac{\partial p'}{\partial x_i} \right\rangle = - \frac{A}{\tau_1} \overline{u_i' T'} \quad (14)$$

and the dissipation of the temperature variance

$$-2k \left\langle \frac{\partial T'}{\partial x_i} \frac{\partial T'}{\partial x_i} \right\rangle = - \frac{2bs}{\tau_1} \overline{T'^2} \quad (15)$$

The diffusion terms are taken as in Eq. (13).



### 3. EVALUATION OF NEW MODEL COEFFICIENTS

The new formulation given in the last section introduces four new model coefficients  $C_1$ ,  $C_2$ ,  $\xi^*$  and  $D$ . These coefficients will be determined using the data available from measurements in the unstable surface layer. Spectral distributions taken in the surface layer under such unstable conditions clearly show the ratio between the horizontal and the vertical scale changing with height. Figure 1 from Kaimal (1978) shows the vertical scale increasing with height while the horizontal scale remains essentially constant. Data taken under these conditions should provide valid information for determining the coefficients in our new model.

The constant in the dissipation time scale can be evaluated by considering the limit of free convection. In this limit we expect the turbulent kinetic energy equation to show an essential balance between buoyant production and viscous dissipation. This assumes that the remaining diffusion terms are less important than these two terms. Data as analyzed by Wyngaard (1979) tend to confirm this assumption. This balance may be represented as

$$\frac{2g\overline{w'\theta'}}{T_o} = \frac{2bq^3}{\Lambda_H} (1 - \xi) + C_2 \xi \frac{\Lambda_H}{\Lambda_V} \frac{\sigma_w^3}{q^3} \quad (16)$$

The free convection limit corresponds to  $z/L \rightarrow -\infty$ . Now if we also consider  $z/z_i \rightarrow 0$  then we can expect  $\Lambda_V/\Lambda_H \rightarrow 0$ . Then Eq. (16) reduces to

$$\frac{2g\overline{w'\theta'}}{T_o} = \frac{2bC_2 \sigma_w^3}{\Lambda} \quad (17)$$

Data in this intermediate height range ( $z/L \rightarrow -\infty$ ,  $z/z_i \rightarrow 0$ ) appear to satisfy the correlation

$$\frac{\sigma_w}{u_*} = (1.3) 3^{1/3} (-z/L)^{1/3} \quad (18)$$

This is equivalent to

$$\sigma_w^3 = (1.3)^3 3z \overline{kg w' \theta'}|_0 \quad (19)$$

When this is used in Eq. (17)

$$C_2 = \frac{\Lambda}{Kbz} \left[ 3(1.3)^3 \right]^{-1} \quad (20)$$

and if we stick with  $k = 0.39$ ,  $b = 0.125$ , and  $\Lambda = 0.65z$

$$C_2 = 2.0 \quad (21)$$

The coefficient  $C_1$  in  $\tau_1$  can be evaluated by appealing to the  $\overline{u'w'}$  component of the Reynolds stress Eq. (1). If we again assume a local equilibrium this leads in the neutral case to

$$\sigma_w^2 U' = \frac{g}{\Lambda_0} \left[ 1 - \xi + C_1 \xi \frac{\Lambda_0}{\Lambda} \frac{\sigma_w}{q} \right] u_*^2 \quad (22)$$

Measurements show (Panofsky, 1974) that  $\sigma_w \approx 1.25u_*$  and

$U' = u_* / kz$ , i.e.,

$$\frac{g}{u_* \Lambda_0} \left[ (1 - \xi) + C_1 \xi \frac{\Lambda_0}{\Lambda} \frac{\sigma_w}{q} \right] = \frac{(1.25)^2}{(0.39)z} \quad (23)$$

For this to hold when  $\Lambda_0/\Lambda \gg 1$  ( $\xi \rightarrow 1$ )

$$C_1 = \frac{1.25}{0.39} \frac{\Lambda}{z} = \frac{0.65(1.25)}{0.39} = 2.0 \quad (24)$$

It thus appears appropriate to take  $C_1 = C_2 = 2$ .

The remaining coefficient D can be estimated by again appealing to the free-convection, surface-layer limit and considering the equation for any one of the normal components of the Reynolds stress. To the same approximation as Eq. (16), the equation for  $\overline{w'w'}$  may be written as

$$-\frac{2g}{T_0} \frac{\overline{w'\theta'}}{\tau_1} = -\frac{1}{\tau_1} (w^2 - q^2/3) - \frac{\xi^*\xi}{\tau_1} q^2 \left( \frac{1}{3} - D \frac{\overline{ww}}{q^2} \right) - \frac{2}{3} \frac{q^2}{\tau_3} \quad (25)$$

When this is combined with the energy equation Eq. (16), the buoyancy term can be eliminated to yield

$$0 = -\frac{1}{\tau_1} (w^2 - q^2/3) - \frac{\xi^*\xi}{\tau_1} q \left( \frac{1}{3} - D \frac{\overline{ww}}{q^2} \right) + \frac{4}{3} \frac{q^2}{\tau_3} \quad (26)$$

In this free convection surface limit we have already seen that  $\xi \rightarrow 1$ ,  $\tau_1 \rightarrow \Lambda/2\sigma_w$  and  $\tau_3 \rightarrow (\Lambda/2\sigma_w^3)q^2$ , so that Eq. (26) can be further reduced to

$$0 = -\frac{2\sigma_w}{\Lambda} \left[ (\sigma_w^2 - q^2/3) + \xi^* q^2 \left( \frac{1}{3} - D \frac{\sigma_w^2}{q^2} \right) \right] + \frac{8}{3} \frac{b\sigma_w^2}{\Lambda} \quad (27)$$

Therefore if we wish to permit  $q^2/\sigma_w^2$  to become large, it is necessary to have  $\xi^* = 1$ . In this limit it is necessary to keep the product of  $(1 - \xi)q^2/\sigma_w^2$  in evaluating D.

$$0 = -\sigma_w^2(1 - D) + q^2/3(1 - \xi) + \frac{4b}{3} \sigma_w^2 \quad (28)$$

$$D = 1 - \frac{q^2}{3\epsilon_w^2} (1 - \xi) - \frac{4b}{3} \quad (29)$$

If we take  $\Lambda_0 = 0.2z_i$  then the two separate correlations of Wyngaard for  $\epsilon_H/u_*$  and  $\epsilon_w/u_*$  asymptotically lead to  $(q^2/\epsilon_w^2)(\Lambda/\Lambda_0)^{2/3} = 3/4$ . Thus when Eq. (10) is used for  $\xi$ , this leads to

$$D = 1 - \frac{1}{4} - \frac{1}{6} = \frac{7}{12} \quad (30)$$

Note this expansion would not have proceeded smoothly if some other exponent rather than 2/3 had been used in Eq. (10).

No new coefficients have been introduced into the diffusion terms.

#### 4. ALGORITHMS FOR SCALE DETERMINATION

The use of separate scales for the horizontal fluctuations and the vertical fluctuations compounds the problem of specifying the model. The single isotropic scale used in our previous model may best be associated with the vertical scale in the present model.

Rather than attempt to modify the scale equation, the equation we have used to determine  $\Lambda$  (Lewellen, 1977) will now be used for  $\Lambda_v$ .

$$\begin{aligned} \frac{D\Lambda_v}{Dq} = & 0.35 \frac{\Lambda_v}{q^2} \frac{\overline{u_i u_j}}{\overline{u_i u_j}} \frac{\partial \overline{u_i}}{\partial x_j} + 0.075q + 0.3 \frac{\partial}{\partial x_i} \left( q \Lambda_v \frac{\partial \Lambda_v}{\partial x_i} \right) \\ & - \frac{0.375}{q} \left( \frac{\partial q \Lambda_v}{\partial x_i} \right)^2 + \frac{0.8 \Lambda_v}{q^2} \epsilon_i \frac{\overline{u_i \epsilon}}{\overline{\epsilon}_0} \end{aligned} \quad (31)$$

Alternatively, we can allow the vertical scale to be determined by whichever of the three following bounds govern locally:

$$\begin{aligned}
 \text{i)} \quad & \frac{d\Lambda}{dz} \leq 0.65 \\
 \text{ii)} \quad & \Lambda \leq 0.25z \\
 \text{iii)} \quad & \Lambda \leq c_w \frac{g}{T_0} \frac{\partial \theta}{\partial z}^{-1/2}
 \end{aligned} \tag{32}$$

The first of these recognizes that changes in the vertical scale cannot occur abruptly. When this first condition is combined with the boundary condition that the vertical scale is zero immediately adjacent to a surface, it yields  $\Lambda = 0.65z$ . The second condition recognizes that the vertical scale cannot exceed a certain fraction of the vertical spread of the region of turbulence. The last condition recognizes that the potential energy involved with the vertical fluctuations in a stably stratified fluid cannot exceed the kinetic energy in the fluctuation. These conditions involve only a slight variation from those used for our single scale model (Lewellen, 1977).

The horizontal scale cannot be specified in quite so straightforward a manner. It must not satisfy either the first or last of the conditions in Eq. (32). It will satisfy the second condition if the two scales are equal in the center of the flow domain. Sufficiently close to the surface, the horizontal scale should also approach zero since the horizontal velocity fluctuation is constrained to approach zero. The rate at which this occurs will depend on the surface roughness as

the surface shear stress serves to transfer energy from the larger scale horizontal fluctuation to the small scale fluctuations produced by the large vertical gradients in the larger scale fluctuations. Although Figure 1 shows  $\Lambda_H$  remaining essentially constant while  $\Lambda_V$  decreases with decreasing  $z$ , there is a gradual increase in the horizontal energy level at high frequency corresponding to a slight decrease in average  $\Lambda_H$  with decreasing  $z$ .

Even in the neutral surface layer, there can be considerable variation in how  $\Lambda_V/\Lambda_H$  behaves close to a surface. Some of the implications of this can be seen by examining the equilibrium turbulent kinetic energy equation in the neutral limit. If diffusion is neglected, as in the last section, this equation may be written in terms of the current model as

$$2\overline{uwu'} = - \frac{2bq^3}{\Lambda_H} \left[ (1 - \xi) + 2\xi \frac{\Lambda_H}{\Lambda_V} \frac{\sigma_w^3}{q^3} \right] \quad (33)$$

After some rearrangement, this may be rewritten as

$$\frac{\sigma_w^3}{q^3} = \frac{\Lambda_V}{\Lambda_H} (1 - \xi) \left[ \frac{\Lambda_V}{kbz} \left( \frac{u_*}{\sigma_w} \right)^3 - 2\xi \right]^{-1} \quad (34)$$

If the values of  $k$ ,  $b$ ,  $\alpha$ , and  $\sigma_w/u_*$  used in evaluating Eqs. (17) - (29) are used here, this yields an equation for  $\sigma_w/q$  as a function of  $\Lambda_V/\Lambda_H$

$$\frac{\sigma_w}{q} = \left( \frac{\Lambda_V}{\Lambda_H} \right)^{5/9} \left[ 4.83 + 2 \left( \frac{\Lambda_V}{\Lambda_H} \right)^{2/3} \right]^{-1/3} \quad (35)$$

Thus, for  $\Lambda_H/\Lambda_V$  varying from 1 to 3, this leads to  $\sigma_w/q$  varying from 0.53 down to 0.3. In homogeneous shear flow in a

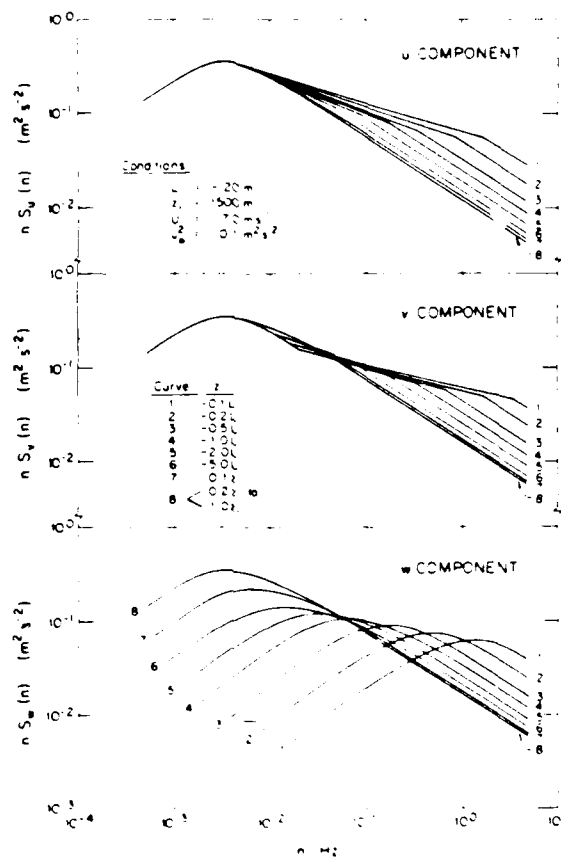


Figure 1. Evaluation of the velocity spectra with height as given by a composite plot of a number of runs (Kaimal, 1978)

wind tunnel, Champagne et al. (1970) reported a value of  $\sigma_w/q = 0.49$  while Hinze (1959) reported a value of 0.31 in turbulent pipe flow. Values between these have been reported for other wind tunnel and atmospheric studies. These differences are in the right direction to be consistent with variations in the anisotropic natures of the eddy scales. That is,  $\Lambda_v/\Lambda_H$  should be closer to one in the homogeneous shear flow case than for pipe flow.

The third bound of Eq. (32) does not apply to  $\Lambda_H$ . Rather in a stably stratified flow, we expect the occurrence of a natural horizontal scale associated with the ratio of the mean horizontal velocity to the Brunt-Väisälä frequency.

We are not proposing a specific recipe for determining  $\Lambda_H$  for all situations. The derivation of a dynamic equation for  $\Lambda_H$  would involve considerations similar to those carried out for the two-point correlation tensor (Sandri, 1978). This requires considerably more work. The prescriptions used in the next section will demonstrate the type of specifications we believe are required.

## 5. COMPARISON WITH EXPERIMENTAL DATA

We will first compare the new model results with atmospheric surface data. This will be done using a superequilibrium version of the model. Then complete numerical solutions will be used to compare model results with data taken across the full height of the unstable free convection layer.



a) Surface Layer Comparisons

When the turbulent layer immediately adjacent to a surface is considered, the time scale of the turbulence is sufficiently small that the ensemble mean values can be assumed to be at their steady-state values. When this condition is combined with the assumption of horizontal spatial homogeneity and high Reynolds number, the momentum and energy equations reduce to the conditions that the vertical momentum and heat flux remain constant with respect to variations in height. The Reynolds stress equations can then be solved for the relationships between the turbulent correlations and the mean velocity and temperature gradients. This can be done with the turbulent diffusion terms included but, since our model plays down the relative role of these diffusion terms, we choose to first compare the model results with the data with these diffusion terms neglected. This constitutes what Donaldson (1973) has termed the superequilibrium approximation.

When the superequilibrium approximation is applied, Eq. (1) reduces to

$$0 = - \overline{u_i' w'} \frac{d\bar{u}_j}{dz} - \overline{u_j' w'} \frac{d\bar{u}_i}{dz} - \frac{1}{\tau_1} \left( \overline{u_i' u_j'} - \delta_{ij} \frac{q^2}{3} \right) \\ - \frac{1}{\tau_2} \left[ \hat{g}_i \hat{g}_j - \frac{1}{2} (\delta_{ij} - \hat{g}_i \hat{g}_j) \right] + g_i \frac{\overline{u_j \theta}}{T_0} + g_j \frac{\overline{u_i \theta}}{T_0} - \frac{q^2}{3\tau_3} \delta_{ij} \quad (36)$$

To complete the system of equations, we must also add the heat flux and temperature variance equations:

$$0 = - \overline{u_i w} \frac{dT}{dz} - \overline{w \theta} \frac{d\bar{u}_i}{dz} + \frac{g}{T_0} \overline{\theta^2} \delta_{ij} - \frac{Aq \overline{u_i \theta}}{\Lambda_H} F_p \quad (37)$$

$$0 = - \overline{w \theta} \frac{dT}{dz} - \left( \frac{bsq}{\Lambda_H} F_p \right) \overline{\theta^2} \quad (38)$$

When the last three equations are normalized using the surface shear stress velocity,  $u_*$ , as the characteristic velocity, the ratio of the heat flux to  $u_* \theta_*$  as the characteristic temperature, and the Monin-Obukhov length,  $L = -(T_0 u_*^2 / g \theta_*)$ , as the characteristic length, they may be written in component form to yield seven algebraic equations to solve for the seven normalized variables:

$$\phi = \frac{kz}{u_*} \frac{\partial u}{\partial z}, \quad \phi_H = \frac{kz}{\theta_*} \frac{\partial \theta}{\partial z}, \quad \frac{\sigma_w}{u_*}, \quad \frac{\sigma_u}{u_*}, \quad \frac{\sigma_v}{u_*}, \quad \frac{\overline{u \theta}}{u_* \theta_*},$$

and  $\frac{\overline{\theta^2}}{\theta_*^2}$  as a function of  $z/L$  and  $\Lambda_H/L$ .

For our comparisons on the unstable side ( $z/L < 0$ ), we will assume

$$\Lambda_v \approx \alpha z \quad (39)$$

and

$$\Lambda_H \approx \left[ \frac{1}{\epsilon z_i} + \frac{e^{-\gamma z/L}}{\alpha z} \right]^{-1} \quad (40)$$

with  $\gamma$  arbitrarily chosen to provide a relatively rapid transition between a neutral value equal to  $\alpha z$  for very small  $z$  and the constant value proportional to the mixed layer height at larger  $z$ . As argued in the last section, the actual transition, i.e.,  $\gamma$ , should depend on the surface roughness in any given case. On the stable side ( $z/L > 0$ ),  $\Lambda_v$  is equal to  $\alpha z$  or  $0.2L$ , whichever is smaller, but no limit is placed

on  $\Lambda_H$ . It is permitted to grow proportional to  $z$  for all  $z/L > 0$ . Again, the more precise variation of  $\Lambda_H$  should depend on surface roughness with a transition from the surface small scale eddies to the larger internal wavelengths associated with the ratio of the mean horizontal velocity to the Brunt-Väisälä frequency. Even after the transition,  $\Lambda_H$  will continue to grow proportional to  $z$  because, as will be seen,  $\partial u / \partial z$  is constant with respect to variations in  $z/L$  after the critical Richardson number is reached.

Figures 2, 3, and 4 show that there is not much variation between the previous single-scale model results for  $\phi$ ,  $\phi_H$  or  $\sigma_w/u_*$  and the results for the current two-scale model. Either provides a creditable representation of the data. The principal difference shows up in the horizontal variances. The single-scale model predicts a variation with respect to  $z/L$  only which is not observed in the data. Rather the data are found to be relatively independent of  $z/L$  and to depend on the mixed layer height instead. Figure 5 shows the dependence of  $\sigma_H/u_*$ ,  $\left[ \sigma_H = \frac{1}{2} \left( \sigma_w^2 + \sigma_v^2 \right)^{\frac{1}{2}} \right]$  on  $z_i/L$  and  $z/L$  as predicted by the present model. The single-scale model would show no dependence on  $z_i/L$ .

In the present model modification, we have not adjusted any coefficients in the temperature correlation equations. However, Figures 6 and 7 show that the modification does provide a modest improvement in representing the data for  $\overline{u\theta}/u_*\theta_*$  and  $\overline{\theta'^2}/\theta_*^2$ . The peak in these correlations, which we previously

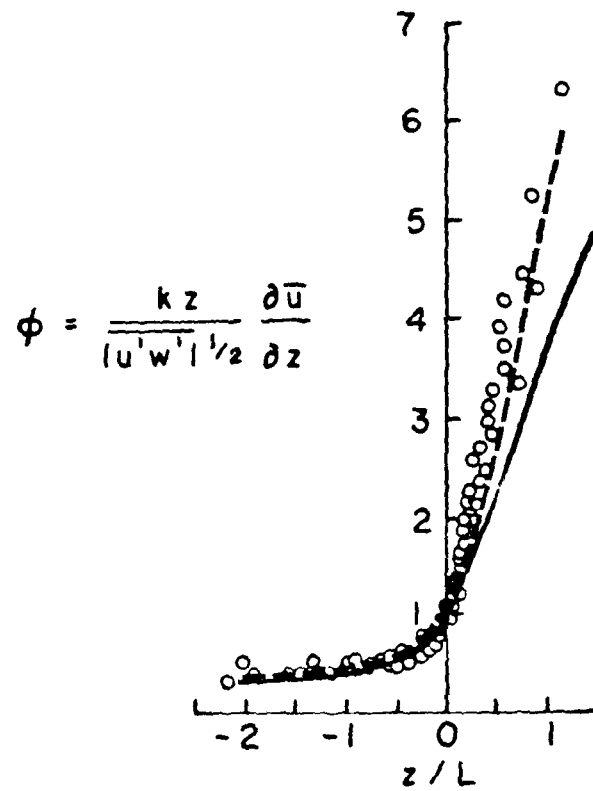


Figure 2. Normalized velocity gradient as a function of the Monin-Obukhov similarity variable [ ---- (Lewellen and Teske, 1973) single scale model; — two-scale model; data from Businger, et al. (1971)]

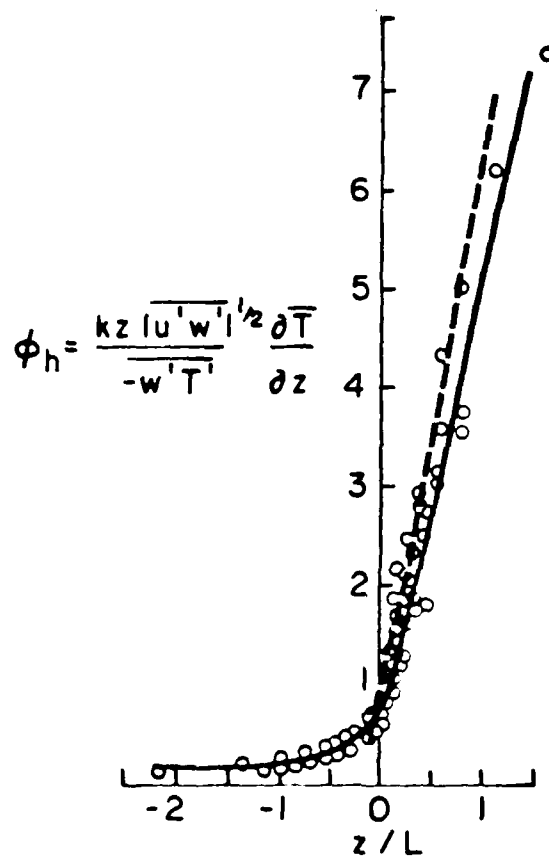


Figure 3. Normalized temperature gradient as a function of the Monin-Obukhov similarity variable [----(Lewellen and Teske, 1973) single scale model; — two-scale model; data from Businger, et al. (1971)]

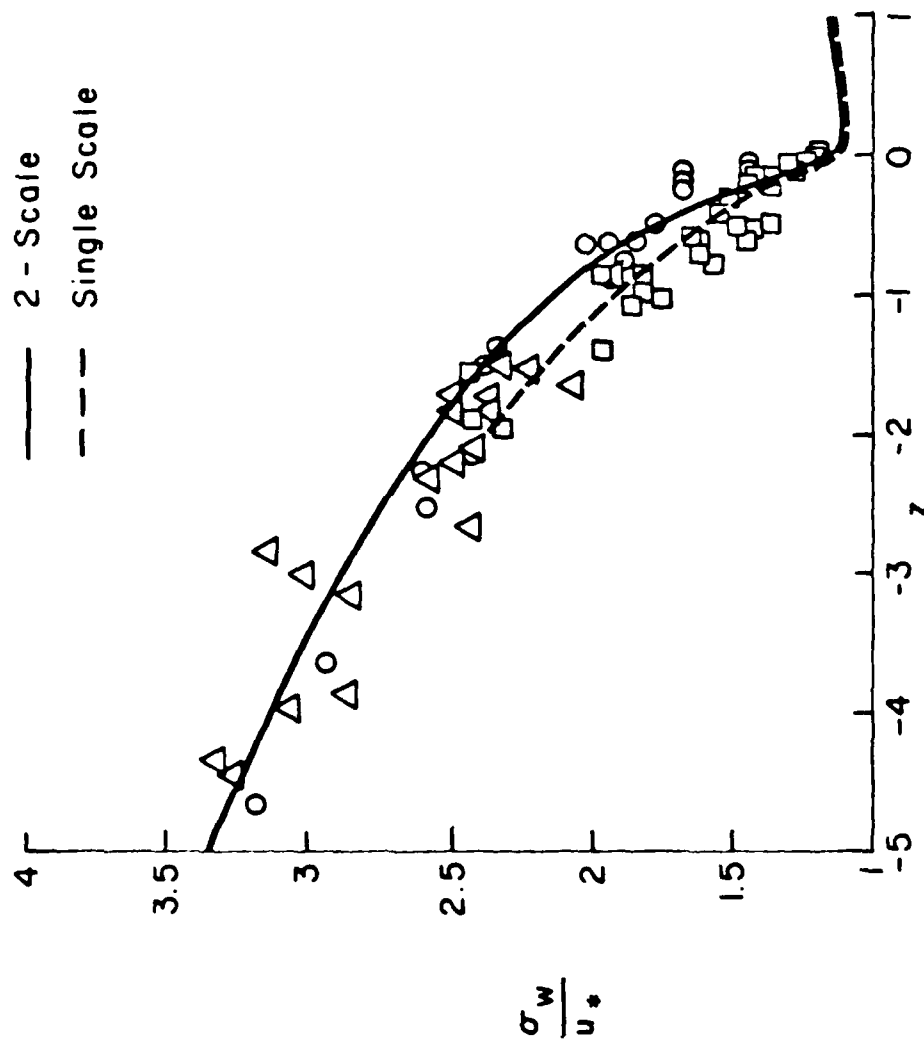


Figure 4. Dimensionless rms vertical velocity fluctuations as a function of the Monin-Obukhov similarity variable [--- (Lewellen and Teske, 1973) single-scale model; — two-scale model; data from Wyngaard, et al. (1971)  $\square$  and Wyngaard(1979)  $\Delta$   $\circ$ ]

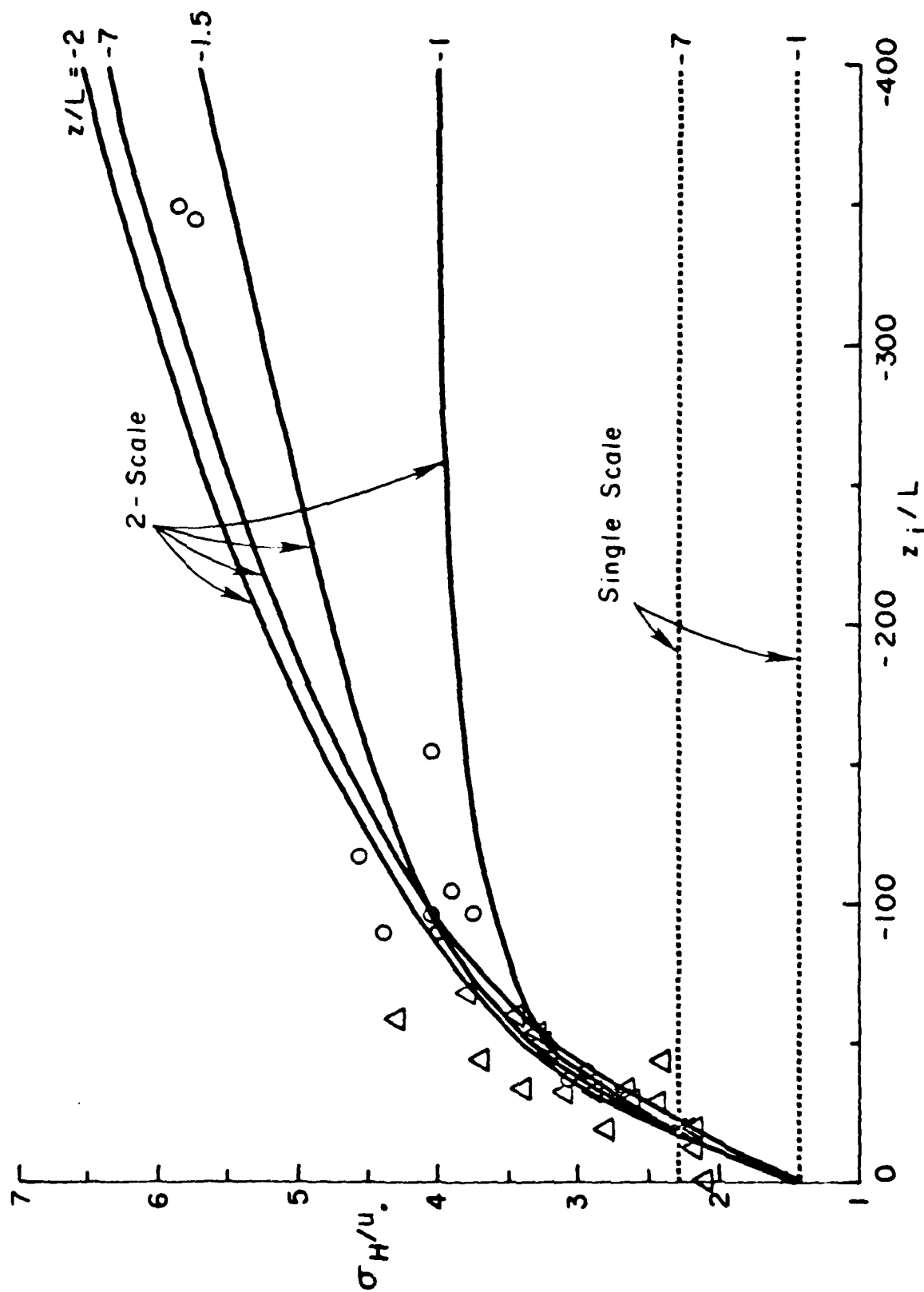


Figure 5. Dimensionless rms horizontal velocity fluctuation as a function of the ratio of the mixed layer height to the Monin-Obukhov length [Data from Wyngaard (1979)]

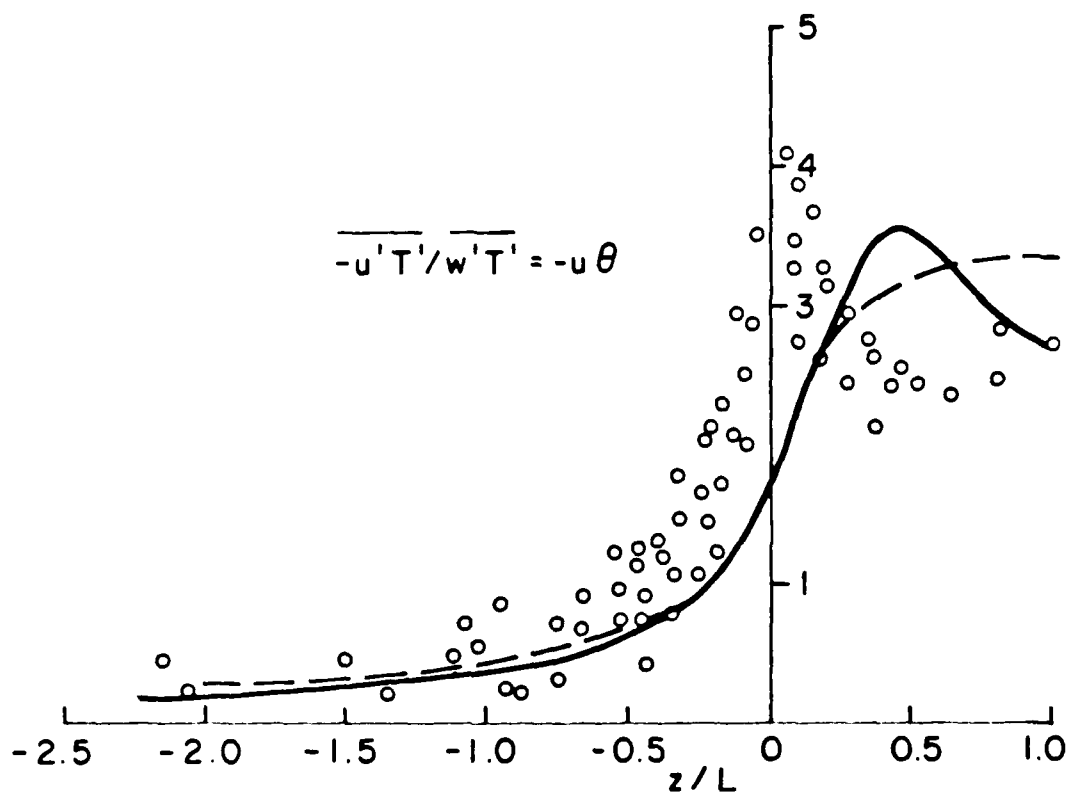


Figure 6. Ratio of the horizontal to the vertical heat flux as a function of the Monin-Obukhov similarity variable [---- (Lewellen and Teske, 1973) single-scale model; — two-scale model; data from Wyngaard, et al. (1971)]



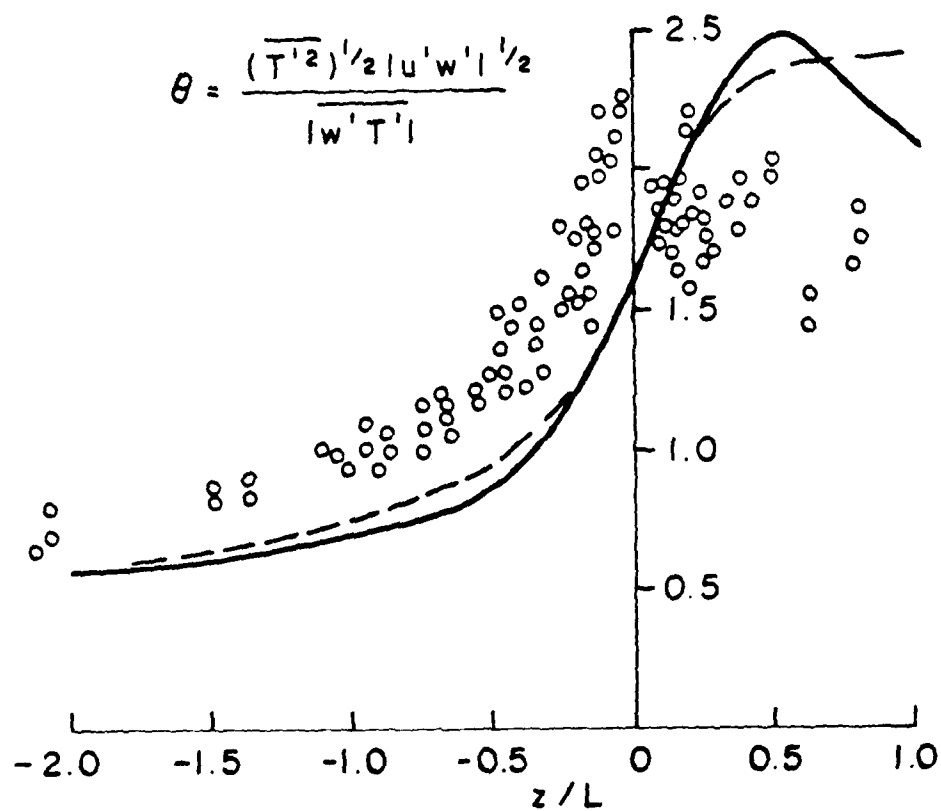


Figure 7. Dimensionless rms temperature fluctuations as a function of the Monin-Obukhov similarity variable [---- (Lewellen and Teske, 1973) single scale model; — two-scale model; data from Wyngaard, et al. (1971)]

felt was due to experimental error near  $z/L = 0$  where  $\theta_* = 0$ , is partially reproduced with the present model, although it is shifted towards positive  $z/L$ .

b) Unstable Mixed Layer Comparison

The next test of the two-scale model was to repeat the calculations of turbulence in an unstable mixed layer (Lewellen, Teske and Donaldson, 1976) using a numerical code which computes the full second-order closure set as a function of  $z$  and  $t$ . Horizontal homogeneity is assumed. For this free convection problem, a constant positive heat flux is applied at the surface and a stable temperature lapse rate is assumed at the top of the domain. With the mean velocity set to zero, a free convection mixed layer forms adjacent to the surface. The thickness of this mixed layer increases with time, but the velocity variances exhibit similarity as a function of  $z/z_i$  when normalized by the characteristic velocity

$$w_* = [(g \overline{w\theta}_0 z_i)/T_0]^{1/3} \quad (41)$$

with  $z_i$  the depth of the mixed layer. Figures 8, 9 and 10 compare the model results with data from Willis and Deardorff (1974). Both models represent the vertical velocity variance very well. The major difference is in the horizontal velocity variance. The two-scale model provides a much better representation of  $\sigma_H$  near the surface and some improvement near the inversion. It also provides improvement in the representation of the temperature variance near the inversion.

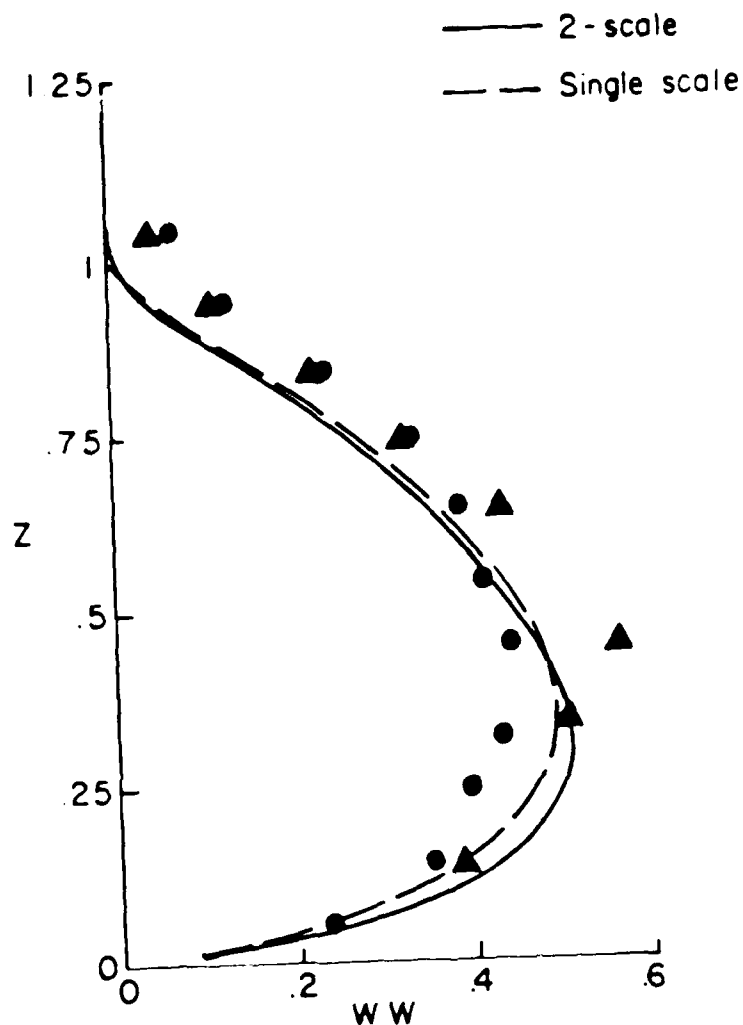


Figure 8. Comparison of free convection prediction and experiment for the normalized vertical velocity fluctuations,  $WW = \overline{w'w'}/w^{*2}$ , as a function of normalized height  $Z = z/z_i$ , where  $w^*$  is the characteristic convective velocity and  $z_i$  is the depth of the mixed layer. Model predictions are for the two-scale model (—) and the single-scale model (----). The solid data points are for laboratory observations given by Willis and Deardorff (1974).

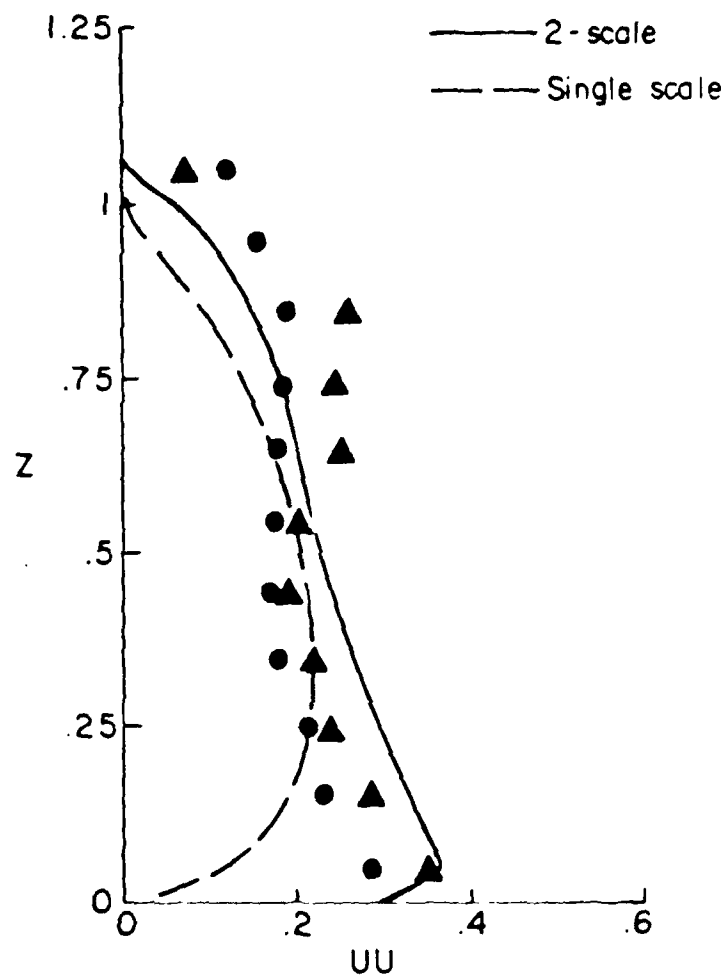


Figure 9. Comparison for the normalized horizontal velocity fluctuations  $UU = \overline{u'u'}/w_*^2$  as a function of normalized height  $Z = z/z_i$  with data and predictions as described in Figure 8.

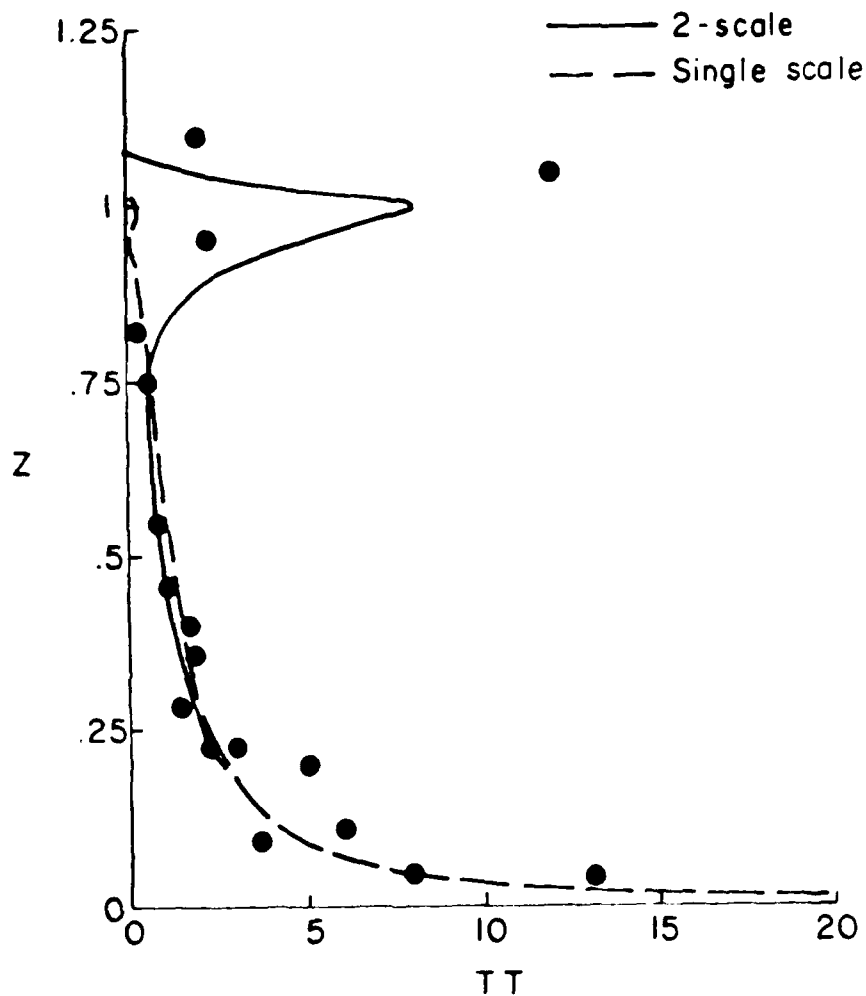


Figure 10. Comparison for the normalized temperature fluctuations  $TT = \overline{T'T'w'^2}/(\overline{w'T_0'})^2$  as a function of normalized height  $Z = z/z_i$ . Data points and predictions are described in Figure 8.

## 6. CONCLUDING REMARKS

Although the comparisons between model and data shown here suggest some further adjustments in scale modeling and/or more sophisticated diffusion modeling are desirable, they do indicate that the use of a two-scale model has the potential for significantly improving model predictions. This is particularly true for the correlations involving fluctuations parallel to a surface.

Other applications of turbulence closure models to the free convection problem may be found in the work of Mellor and Durkin (1975), Garwood (1977), Zeman and Lumley (1976), Lumley, Zeman and Siess (1978), Wyngaard (1979), and Warn-Varmas and Piacsek (1979). The last four of these attempt to improve upon the modeling by bringing in more information about the triple velocity correlation. This assumes that the basic difficulties in the modeling are due to inadequate representation of the local single-point higher correlations on the local value of the lower order correlations and their derivatives. We have chosen the alternative approach of bringing in more information about the macroscale flow. Due to the existence of large eddies in the flow, we believe it is more important to bring in some rough information about the nature of the two-point correlations than it is to delve more deeply into the intricacies of the relationships between the single-point higher order correlations and the derivatives of the single-point lower order correlations.

## REFERENCES

1. Reynolds, W. C.: Computation of Turbulent Flows, Annual Review of Fluid Mechanics, Vol. 8, 183-208, 1976.
2. Launder, B. E. and Spalding, D. B.: Mathematical Models of Turbulence, Academic Press, London and New York, 1972.
3. Lewellen, W. S.: Use of Invariant Modeling. In Handbook of Turbulence (W. Frost and T.H. Moulden, eds), Plenum Press, 237-280, 1977.
4. Mellor, G. L. and Yamada, T.: A Hierarchy of Turbulence Closure Models for Planetary Boundary Layers, J. Atmos. Science, Vol. 31, 1327-1339, 1973.
5. Rotta, J. C.: Statistische Theorie Nichthomogener Turbulenz, Z. Physik, 129, 547-592, 1951.
6. So, R. M. C. and Peskin, R. L.: Comments on Extended Pressure-strain Correlation Models, ZAMP, 31, 56-65, 1980.
7. Kaimal, J. C.: Horizontal Velocity Spectra in an Unstable Surface Layer, J. of Atmospheric Sciences, 35, 18-24, 1978.
8. Wyngaard, J. C.: The Atmospheric Boundary Layer - Modelling and Measurements, Proc. of the 2nd Symposium on Turbulent Shear Flow, Imperial College, London, pp. 13.25 - 13.30, 1979.
9. Panofsky, H. A.: The Atmospheric Boundary Layer Below 150 Meters, Annual Reviews of Fluid Mechanics, 6, 147-177, 1974.
10. Champagne, F. H, Harris, V. G., and Corsin, S.: Experiments on Nearly Homogeneous Turbulent Shear Flow, J. Fluid Mechanics, 41, 81-139, 1970.
11. Hinze, J. O.: Turbulence, McGraw Hill, 522-523, 1959.
12. Donaldson, C. duP.: Atmospheric Turbulence and the Dispersal of Atmospheric Pollutants, AMS Workshop on Micrometeorology (D. A. Haugen, ed.), Science Press, pp. 313-390, 1973.
13. Lewellen, W. S., Teske, M. E., and Donaldson, C. duP.: Variable Density Flows Computed by a Second-Order Description of Turbulence, AIAA J. 14, 382-387, 1976.
14. Willis, G. E. and Deardorff, J. W.: A Laboratory Model of the Unstable Planetary Boundary Layer, J. Atm. Sci. 31, 1297-1307.
15. Mellor, G. L. and Durkin, P. A.: The Structure and Dynamics of the Ocean Mixed Layer, J. Phys. Ocean., 5, 718 - 728, 1975.

16. Garwood, R. W.: An Oceanic Mixed Layer Model Capable of Simulating Cyclic States, J. Phys. Ocean., 7, 455 - 468, 1977.
17. Zeman, O. and Lumley, J. L.: Modeling Buoyancy Driven Mixed Layers, J. Atmos. Sci., 33, 1974 - 1988, 1976.
18. Lumley, J. L., Zeman, O., and Siess, J.: The Influence of Buoyancy on Turbulent Transport, J. Fluid Mech., 84, 581 - 597, 1978.
19. Warn-Varmas, A. C. and Piacsek, S. A.: An Investigation of the Importance of the Third-Order Correlations and Choice of Length Scale in Mixed Layer Modelling, Geophys. and Astrophys. Fluid Dynamics, 13, 225 - 243, 1979.
20. Hanjalic, K., Launder, B. E., and Schiestel, R.: Multiple-Time-Scale Concepts in Turbulent Transport Modeling, Proc. of the 2nd Symposium on Turbulent Shear Flows, Imperial College, London, 10.37 - 10.42, 1979.
21. Sandri, G.: Recent Results Obtained in the Modeling of Turbulent Flows by Second-Order Closure, AFOSR-TR-78-0650, 1978.
22. Businger, J.A., Wyngaard, J.C., Izumi, Y. and Bradley, E.F.: Flux-Profile Relationships in the Atmospheric Surface Layer, J. Atmos. Science, 28, 181-189, 1971.
23. Lewellen, W. S. and Teske, M. E.: Predictions of the Monin-Obukhov Similarity Functions from an Invariant Model of Turbulence, J. Atmos. Sciences, 30, 1340-1345, 1973.
24. Wyngaard, J.C., Coté, O.R., and Izumi, Y.: Local Free Convection, Similarity, and the Budgets of Shear Stress and Heat Flux, J. Atmos. Sciences, 28, 1171 - 1182, 1971.



APPENDIX B

Transport of Water Vapor through the  
Atmospheric Boundary Layer

by  
W. S. Lewellen

(Presented at the Workshop on Atmospheric Water Vapor  
at Vail, Colorado, September 11-13, 1979.)

PRECEDING PAGE BLANK-NOT FILMED

TRANSPORT OF WATER VAPOR THROUGH THE  
ATMOSPHERIC BOUNDARY LAYER\*

by

W. S. Lewellen

Aeronautical Research Associates of Princeton, Inc.  
50 Washington Road, P.O. Box 2229  
Princeton, New Jersey 08540

(Presented at the Workshop on Atmospheric Water Vapor  
at Vail, Colorado, September 11-13, 1979.)

ABSTRACT

The interdependence between the transport of water vapor through the atmospheric boundary layer and its distribution within the layer is reviewed. The problem is approached using second-order closure, turbulent transport modeling with the results related to simple mass transfer coefficients. The dependence of moisture fluctuations on such parameters as wind speed, thermal stability, and surface roughness is summarized. The results of example calculations are used to illustrate such phenomena as: the influence of water vapor flux on boundary layer stability; the interaction of water vapor with a strong temperature inversion at the top of the boundary layer; the interaction between thermal radiation, condensation, and turbulence when phase change occurs in the boundary layer; and the relative role of different size eddies in transporting water vapor across the boundary layer.

---

\*This work was supported in part by the Naval Air Systems Command, Contract No. N00019-79-C-0366.

## INTRODUCTION

The atmospheric boundary layer, which consists of approximately the lowest 1 km of the atmosphere, plays a key role in controlling the cycling of water thru the atmosphere. On a global average basis, the turbulent transport of water vapor thru this atmospheric layer must balance the average precipitation of liquid water, about 1 m per year (Coantic, 1978). This transport is achieved by turbulent eddies mixing the air with high relative humidity next to the surface with dryer air above it. Thus the distribution of water vapor within the boundary layer is inherently dependent upon the transport of water vapor thru it. It is equally dependent upon the dynamics of the turbulent air motion in this layer.

Although it is the turbulent eddies which drive the transport of vapor, it is just as valid to note that the latent energy transported thru the boundary layer with the water vapor is ultimately responsible for fueling most of the atmospheric motions producing the turbulence. As pointed out in the previous paper by Klemp, the intensity of an atmospheric storm can depend critically upon the water vapor content of the boundary layer air which feeds into the storm.

To understand the transport of water vapor it is necessary to understand the dynamics of the turbulent eddies ranging in scale from approximately 10  $\mu$ m to 100 m next to the surface. The smallest eddies dominate the transport close to the surface. At increasing altitudes, the scale of the eddies most responsible for vapor transport will also increase. Since we are limiting our attention to a boundary layer thickness of order 1 km or less, the largest scale eddy of interest is of order of a few 100 m. Larger scale motions must be broken down to smaller scales by shear production before it enters directly into the vertical transport of vapor close to the surface.

In the next section, a review of turbulent transport modeling is given using a second-order closure approach. This allows some of the physics of the production and decay of turbulence to be incorporated into a semi-empirical framework for investigating the sensitivity of vapor transport to such variables as wind speed, thermal stability, surface roughness, etc. These turbulent transport equations can also be integrated to indicate to which parameters the simple bulk mass transfer coefficient is sensitive. Results of several example calculations are reviewed in later sections.

## MODEL EQUATIONS

The ensemble-averaged, Eulerian equation of mass continuity for a species concentration may be written as

$$\frac{DC}{Dt} = -\frac{\partial \overline{u_i c}}{\partial x_i} + D \frac{\partial^2 C}{\partial x_i^2} + S \quad (1)$$

where  $C$  is the mean value of the concentration of a species such as water vapor,  $c$  is the fluctuating value,  $u_i$  is the fluctuating velocity in direction  $x_i$ ,  $D$  is the molecular diffusion coefficient and  $S$  any source term. Equation (1) is exact but undetermined even if the mean velocity  $U_i$  is known because of the presence of the additional variable  $\overline{u_i c}$  representing the ensemble average of the correlation between the fluctuating velocity  $u_i$  and concentration fluctuations at a point. The vertical component of this turbulent transport of species is the primary variable of interest to us here.

An exact equation can be written for this variable (e.g., Donaldson, 1973).

$$\begin{aligned} \frac{D\overline{wc}}{Dt} = & -\overline{wu_i} \frac{\partial C}{\partial x_i} - \overline{u_i c} \frac{\partial W}{\partial x_i} + \frac{g}{T_0} \overline{c\theta_v} - \frac{\partial \overline{wu_i c}}{\partial x_i} \\ & - \frac{\overline{c}}{\rho} \frac{\partial \overline{p'}}{\partial z} + D\overline{w} \frac{\partial^2 \overline{c}}{\partial x_i^2} + \overline{wc} \frac{\partial^2 \overline{w}}{\partial x_i^2} \end{aligned} \quad (2)$$

The first two terms on the right-hand side are production terms due to the interaction of correlations and the mean concentration or velocity gradients. The third term is a buoyancy term representing the direct effect of a correlation between the species and virtual potential temperature fluctuation  $\theta_v$ . The coefficient to this latter term is the ratio of the gravitational acceleration  $g$  to the reference temperature  $T_0$ .

The last four terms on the right-hand side introduce variables other than second-order correlations and they leave the system of

equations undetermined. The task of second-order closure is to model these terms as functions of the second-order correlations and the mean flow variables. A simple modeled form appropriate for high Reynolds number flow and providing, at least, the minimum information needed to close the system may be written as (Lewellen, 1977)

$$\frac{D\overline{wc}}{Dt} = -\overline{wu_i} \frac{\partial C}{\partial x_i} - \overline{u_i c} \frac{\partial W}{\partial x_i} + \frac{g}{T_0} \overline{c\theta_v} + 0.3 \frac{\partial}{\partial x_i} (q \frac{\partial \overline{wc}}{\partial x_i}) - \frac{0.75q}{\Lambda} \overline{wc} \quad (3)$$

The coefficients to the last two terms are carried over from modeling the velocity and temperature correlation equations, while  $q$  and  $\Lambda$  represent velocity and length scales of the turbulence. When dealing with a plume, it appears necessary to recognize that the velocity and length scales for the species fluctuations can be quite different from those of the velocity or temperature fluctuations (Lewellen and Teske, 1976), but for the spatially homogeneous case of most interest here, this problem will not arise.

We do not expect that the last two modeled terms in Eq. (3) used to replace the complex terms of the exact equation will faithfully represent all of the information present. However, for most problems, we are interested in only a small part of the information contained in the complete turbulent spectrum. We believe that the two modeled terms provide at least the minimum amount of desired information needed to close the system at the second order. The first modeled term introduces diffusion to prevent excessive gradients in the species flux. The other modeled term, a tendency-towards-isotropy term, introduces the required feedback which permits the flux to reach an equilibrium level even in the presence of large production contributed by the first three exact terms on the right-hand side of Eq. (3).

The effect of buoyancy on transport comes into Eq. (3) in two ways: through its influence on the stability of the velocity fluctuations, and through the buoyant term involving the cross

correlation of the species and the virtual potential temperature,  $\overline{c\theta_v}$  which appears directly in Eq. (3). This term is not a result of our closure modeling but arises directly from the buoyant term in the momentum equation. However, modeled terms must appear in the equation derived for  $\overline{c\theta_v}$ . If these are treated in a similar fashion to those in Eq. (3), the equation for  $\overline{c\theta_v}$  may be written as

$$\begin{aligned} \frac{D\overline{c\theta_v}}{Dt} = & - \overline{u_j \theta_v} \frac{\partial C}{\partial x_j} - \overline{u_j c} \frac{\partial \theta_v}{\partial x_j} \\ & + 0.3 \frac{\partial}{\partial x_j} q \Lambda \frac{\partial \overline{c\theta_v}}{\partial x_j} - \frac{0.45 q \overline{c\theta_v}}{\Lambda} \end{aligned} \quad (4)$$

With the velocity and temperature fields specified or calculated from similarly modeled equations (Lewellen, 1977), Eqs. (1), (3), and (4) form a closed set to determine  $C$ ,  $\overline{wc}$ , and  $\overline{c\theta_v}$  when appropriate boundary conditions are applied.

The humidity transport can influence the velocity and temperature fluctuations even in the absence of phase change through the buoyancy terms involving  $\theta_v$  since

$$\theta_v = T - T_o + \frac{gz}{c_p} + 0.61 T_o H = \theta + 0.61 T_o H$$

with  $H$  the mean water vapor mixing ratio,  $c_p$  the specific heat of air, and  $\theta$  the mean potential temperature. In the marine atmospheric boundary layer, the contribution of the moisture flux to buoyancy can sometimes exceed the contribution from the temperature difference. In terms of the Bowen ratio ( $\beta \equiv c_p \overline{w\theta} / L\overline{wH}$  with  $L$  the latent heat of evaporation)

$$\overline{w\theta_v} = \overline{w\theta} \left( 1 + \frac{0.61}{\beta} \frac{c_p T_o}{L} \right)$$

$$\overline{w\theta_v} \approx \overline{w\theta} \left( 1 + \frac{0.074}{\beta} \right)$$

Typical values of  $\beta$  for the air-sea interaction are  $\approx 0.05$ .

# INFLUENCE OF STABILITY IN THE SURFACE LAYER

For the steady state spatially homogeneous case which should be appropriate close to the surface, but above any sources or sinks of the surface elements themselves, Eq. (1), (3), and (4) reduce to

$$\overline{wc} = \text{const.} \quad (5)$$

$$0 = \overline{ww} \frac{\partial C}{\partial z} + \frac{g}{T_o} \overline{c\theta_v} - \frac{Aq\overline{wc}}{\Lambda} \quad (6)$$

$$0 = -\overline{w\theta} \frac{\partial C}{\partial z} - \overline{wc} \frac{\partial \theta_v}{\partial z} + 0.3 \frac{\partial}{\partial z} \left( q \frac{\partial \overline{c\theta_v}}{\partial z} \right) - \frac{0.45q}{\Lambda} \overline{c\theta_v} \quad (7)$$

When the diffusion term in Eq. (7) is neglected on the basis that  $\overline{c\theta_v}$  is approximately constant, then Eqs. (5)-(7) can be manipulated to give

$$\overline{wc} = - \left[ \frac{\frac{4\overline{ww}}{3q^2} + \frac{g}{\theta_o} \frac{\Lambda \overline{w\theta_v}}{0.34q^3}}{1 + \frac{g}{\theta_o} \frac{\Lambda^2}{0.34q^2} \frac{\partial \theta}{\partial z}} \right] \Lambda q \frac{\partial C}{\partial z} \quad (8)$$

The term in the bracket is a function of the Monin-Obukhov similarity variable  $z/L$  ( $L = -T_o u_*^3 / kg \overline{w\theta_v}$  with  $u_*^2 = \overline{uw_o} + \overline{vw_o}$ ) only. In terms of the usual similarity variable  $\phi_c$ , Eq. 8 can after some manipulation be written as

$$\frac{u_* k z}{\overline{wc}} \frac{\partial C}{\partial z} = \phi_c(z/L) = \frac{-3kzu_*q/4\overline{ww}}{[1 - 11.3(u_*^3/q\overline{ww})(z/L)]} \quad (9)$$

with  $k$ , von Karman's constant, equal to the value necessary to make

$$\phi_m(0) = \frac{kz}{u_*} \frac{\partial u}{\partial z} \Big|_0 = 1$$

In Eq. (9)  $\partial \theta_v / \partial z$  has been replaced by  $(\overline{w\theta_v} / \overline{wc}) \partial C / \partial z$  in recognition of the fact the model treats  $\phi_c$  as identical to  $\phi_m$ . This function as obtained from the temperature data of Businger, et. al., 1971 is shown in Figure 1, along with the predictions using a second-order closure model with the diffusion terms included (Lewellen and Teske, 1973). In this



$$\epsilon = \frac{kz u_*' \partial \theta}{-w \theta \partial z}$$

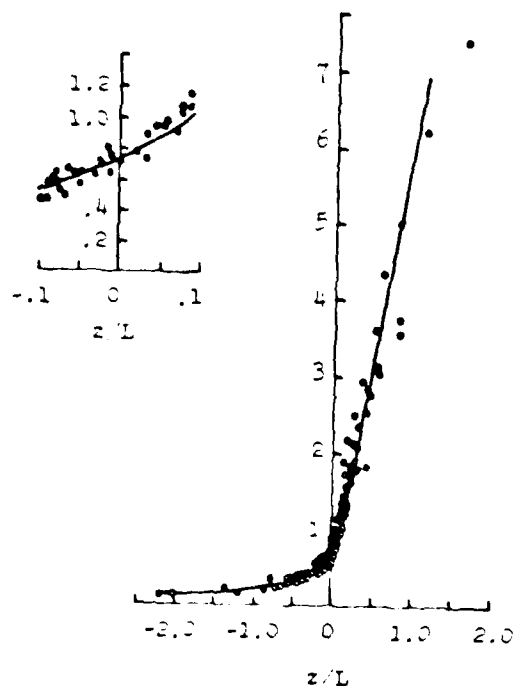


Figure 1. Normalized velocity gradient as a function of the Monin-Obukhov similarity variable: model predictions, Lowellen and Teske, 1973, solid lines; observations, circles.  
(Source: Businger et al (9))

calculation,  $\Lambda$  was taken equal to  $0.65z$  except on the stable side where it has an upper bound equal to  $0.2L$ . Most data appear to agree that  $\phi_c = \phi_\theta$ , although some data have been reported at variance with this theoretical result (e.g., Verma, Rosenberg and Bladd, 1978). Two factors which can sometimes allow the humidity to be transported by the eddies in a different manner from the temperature are thermal radiation at sufficiently low wind speeds and the possibility of the boundary conditions being introduced at different scales. These factors should be the exception rather than the rule.

Figure 1 shows that humidity gradients will be strongest where there is either strong transport of humidity, low winds, or where the flow is quite stable.

Humidity transport data are often reported in the form of a bulk transfer coefficient

$$C_q = U_r \frac{\overline{wh_s}}{(H_r - H_s)} \quad (10)$$

with  $U_r$  and  $H_r$  taken at some arbitrary reference height such as at 10m. Equation (9), in combination with a similar but quantitatively different function  $\phi_m$  for  $\partial U / \partial z$ , can be integrated from the effective surface roughness height  $z_0$  to  $z_r$  to yield  $C_q$  as a function  $z_0/z_r$  and  $z_r/L$ . However, attempts at correlating data in this fashion have only met with modest success as illustrated in Figure 2 from Smith, 1974. The relatively large scatter in the data is not adequately explained by the uncertainty involved in the effective  $z_0$  for a water surface with waves. It probably also represents some difficulty in measuring the true surface temperature of the water.

The problem of determining the bulk transfer coefficient for transport across the total boundary layer can be subdivided into the problem of transporting across the separate layers which make up the boundary layer. There are at least four separate regions which can usefully be defined: 1) the surface sublayer or canopy layer, 2) the surface constant flux layer,

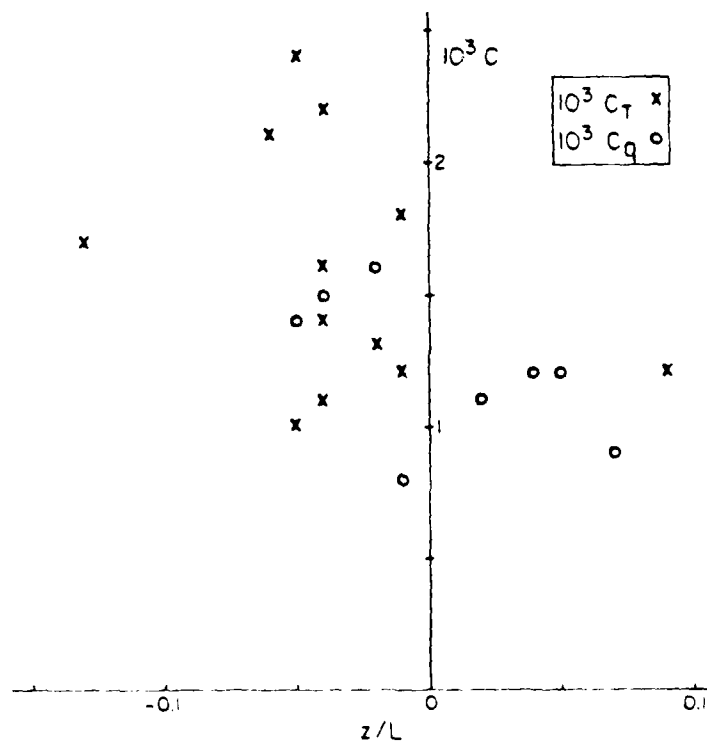


Fig 2. Heat flux (x) and evaporation coefficients (o) as a function of stability (Smith, 1974).

3) the main boundary layer, and 4) any capping stable inversion layer. Equation (10) can be rewritten for the total boundary layer as

$$C_q = (U_r \sum_i R_i)^{-1} \quad (11)$$

where  $R_i$  is defined as an individual layer resistance

$$R_i = \Delta H_i / \overline{w h_s} \quad (12)$$

The best defined region is Region 2 where  $R_2$  is a function of thickness and  $L$  only. For a neutral layer it is given simply by

$$u_* R_2 = 1.9 \ln(z/z_{S,L.}) \quad (13)$$

where  $z_{S,L.}$  is the top of Region 1. The influence of stability on  $R_2$  through the Monin-Obukhov length  $L$  is given in Figure 3.

The sublayer "Region 1" resistance is usually parameterized in terms of an effective roughness  $z_0$ . The effective roughness for momentum will not be equal to the effective roughness for mass transfer, in general.

To better understand the difference between the effective roughness for momentum and the effective roughness for moisture transport, it is necessary to look at the transition layer which generally consists of some canopy of vegetation over land and a wavy surface over water. Integration of the momentum and species equation across this transition or canopy layer of height  $h$  with appropriate source and sink terms proportional to the wetted area per unit volume,  $A_w$ , leads to

$$\left. \frac{C_q}{C_D} \right|_h = \frac{(\frac{D}{V}) \int_0^h C_f A_w q \left( \frac{C - C_s}{C_h - C_s} \right) dz}{(3/4)^{3/4} \left( 1 + \frac{D_p}{D_f} \right) \int_0^h C_f A_w q \frac{U}{U_h} dz} \quad (14)$$

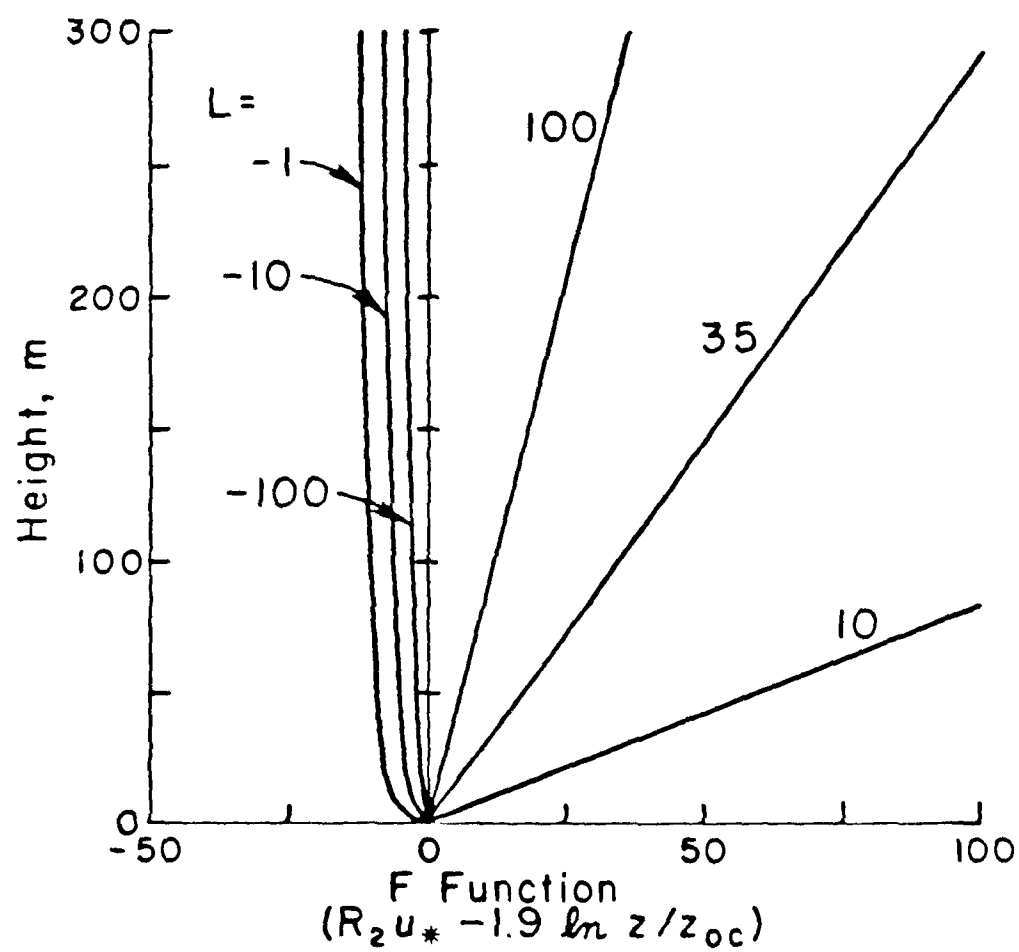


Figure 3. Incremental resistance to deposition as a function of height and stability as given by surface layer functions.

where  $D/\nu$  is the ratio of the molecular diffusivity of water vapor in air to the kinematic viscosity of air,  $D_p/D_f$  is the ratio of pressure-to-friction forces on the surface elements. The 1/4-power exponent appearing in Eq. (14) is only appropriate for  $D/\nu \geq 1$ . The ratio of the two integrals is a function of element shape,  $S$  and Reynolds number,  $Re$  so that

$$\left. \frac{C_q}{C_D} \right|_h = \frac{(D/\nu)^{1/4} G(Re, S)}{(3/4)^{3/4} (1 + D_p/D_f)} \quad (15)$$

Under standard conditions,  $D/\nu \approx 1.5$  for water vapor diffusing in air, so for a rough approximation setting  $G = 1$ ,

$$\left. \frac{C_q}{C_D} \right|_h \approx \frac{1.37}{1 + D_p/D_f} \quad (16)$$

The ratio of pressure drag to friction drag should be expected to increase with wind until wave breaking occurs to greatly increase the contact surface area between air and sea. Thus,  $C_q/C_D$  should first decrease with wind speed and then increase as wave breaking occurs.

Within a vegetation canopy the drag ratio depends upon the structure of the canopy. It has values of 3 or greater for a typical forest canopy (Thom, 1975).

Examples of calculations of the resistance across the outer boundary layer and the upper inversion layer will be given in the following sections.

In considering transport thru the main boundary layer we will concentrate on conditions leading to an unstable mixed layer capped by a stable temperature inversion. Three reasons for this biased treatment are: 1) that on the average the boundary layer is unstable; 2) the majority of water vapor transport occurs under unstable conditions since  $R_2$  is sufficiently large under stable conditions to impede transport; and 3) it is simpler than for stable conditions. The reader interested in second-order

closure model results of the inherently unsteady, stable layer is referred to Lewellen et al. 1974, Yamada and Mellor 1975, or Borst and Wyngaard 1978. Simple parameterized models of the stable layer have been recently given by Zeman, 1979 and Yamada, 1979.

## TRANSPORT THRU THE UNSTABLE MIXED LAYER

Typical profiles of potential temperature and water mixing ratio in an unstable mixed layer are given in Fig. 4. The data shown here were taken from the Air Mass Transportation Experiment (AMTEX) as reported by Wyngaard, et al. 1978. The surface layer relations hold to altitudes of approximately  $0.2 Z_i$  and then the layer is essentially uniformly mixed up thru approximately  $0.9 Z_i$ . The moisture content in the mixed layer is a function of time but  $C_q$  remains a function of  $z/L$  and  $z_0/L$  only.

The top portion of the mixed layer and the capping inversion layer introduce additional parameters into the problem, namely temperature, humidity, and velocity jumps across this thin sharp gradient region. As long as phase change does not occur, the similarity between temperature and humidity transport should remain valid in the form

$$\frac{\overline{hw}}{\overline{\theta w}} = \frac{\Delta H}{\Delta \theta} \quad (17)$$

Since  $\Delta H/\Delta \theta$  is generally negative the ratio of the fluxes must also be negative. Figures 5 and 6 show data on the moisture and heat flux variation within the mixed layer. The complementary temperature-humidity correlation is given in Fig. 7. The temperature-humidity correlation is positive at the bottom and negative at the top. The curves represent the results of A.R.A.P.'s model simulation of correlations approximating those reported.

The available data does not meet the conditions necessary for a rigorous model verification test (Lewellen et al. 1979). The model is started with the mean flow variables approximating those reported for 15 February and the turbulent fluctuations allowed to adjust to these mean distributions. The geostrophic wind was adjusted to give the reported value of the surface



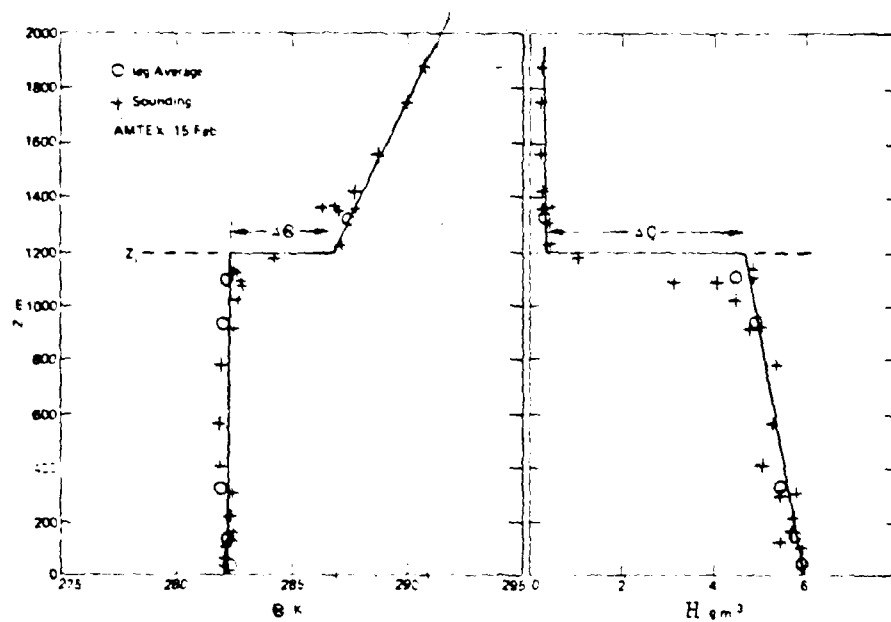


FIG. 4. Typical profiles of mean potential temperature  $\Theta$  and mean absolute humidity  $H$  during AMTEX. Note the well-defined inversion base at  $z_i$  and the jumps  $\Delta\Theta$  and  $\Delta H$  there. (Wyngaard et al. 1978).

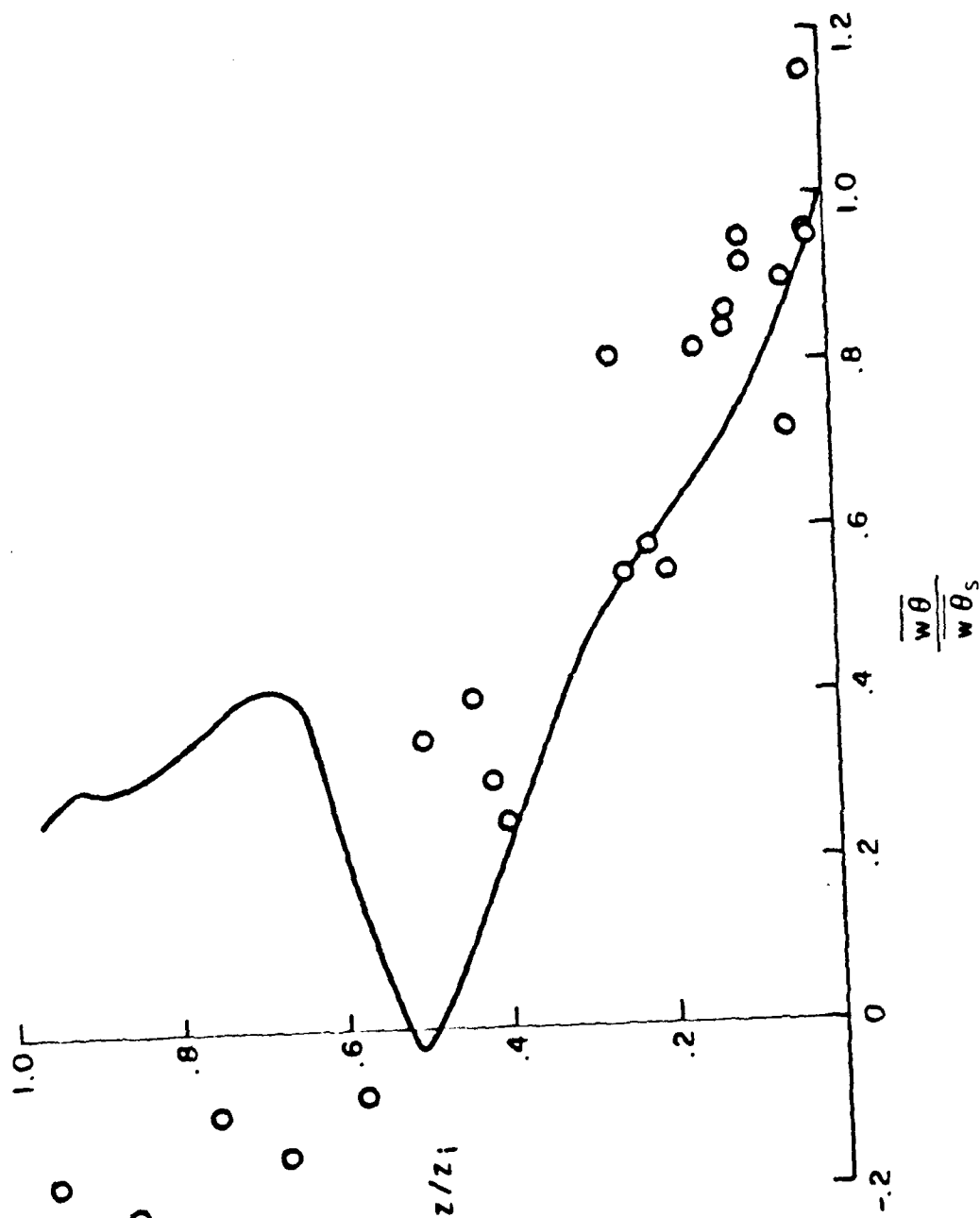


Figure 5. Vertical heat flux as a function of altitude for conditions simulating the Air Mass Transformation Experiment (AMTEX). o-data from Wynngaard et al 1978).

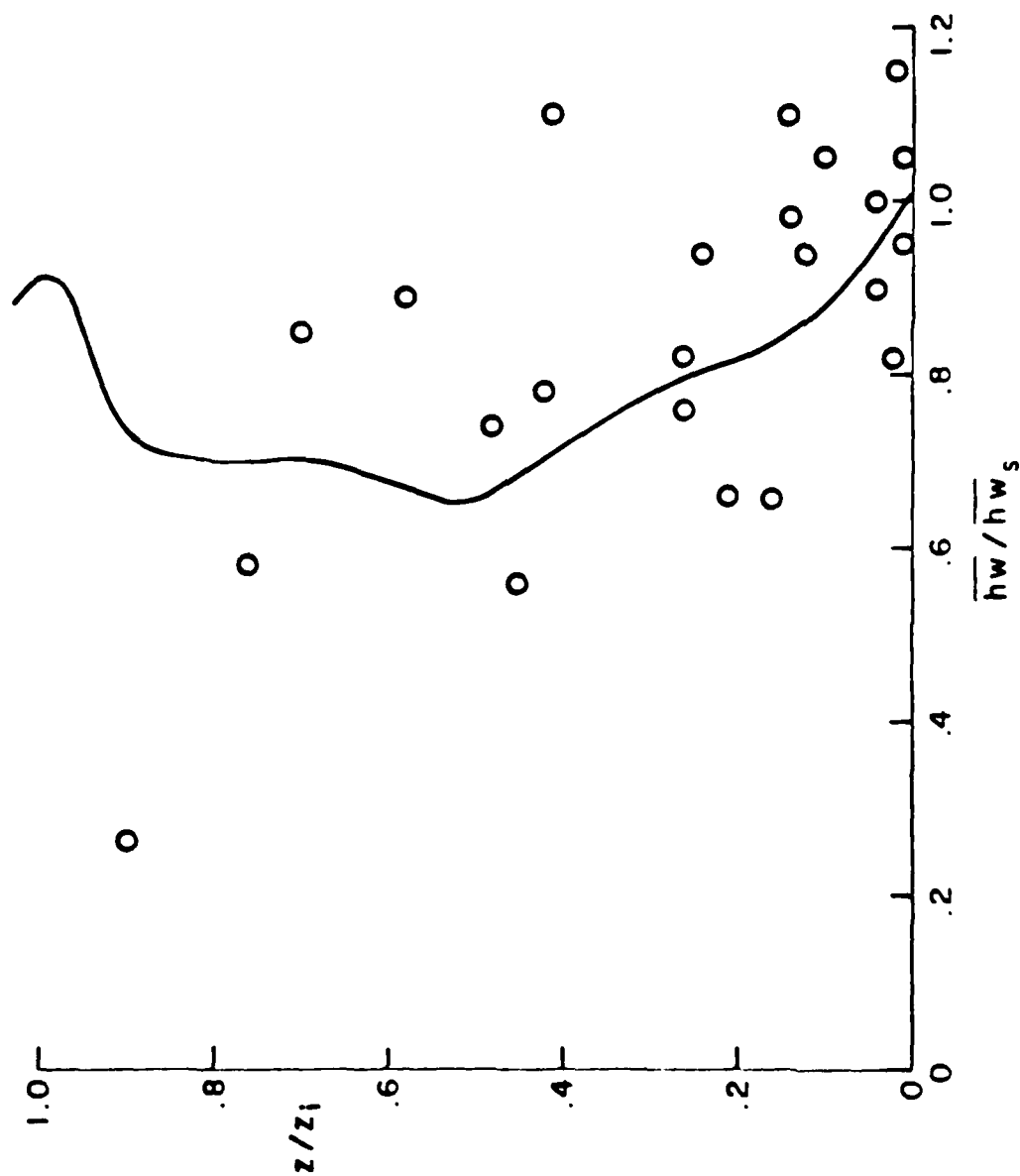


Figure 6. Vertical humidity flux as a function of altitude for conditions simulating the Air Mass Transformation Experiment (AMTEX). o-data, Wyngaard et al. 1978.

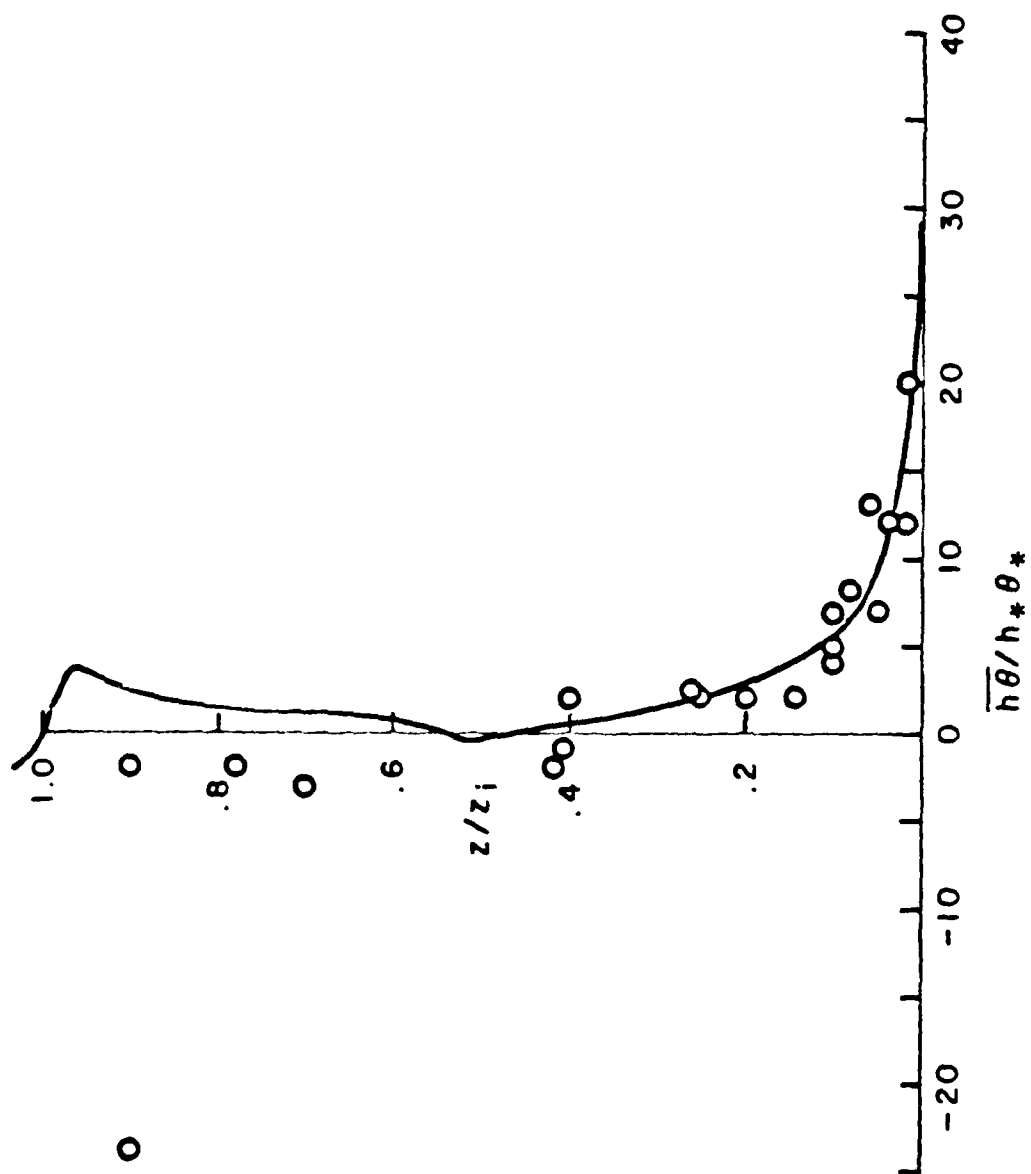


Figure 7. Temperature-humidity covariance as a function of altitude for conditions simulating the Air Mass Transformation Experiment (AMTEX). o-data, Wyngaard et al. 1978.

shear stress and the sea surface temperature was adjusted to yield the reported value of surface heat flux. These adjustments also fix the surface humidity flux which agrees with the reported value to within 10 percent.

In the lower half of the mixed layer, the model predictions fall well within the scatter of the data. There are marked disparities in the upper half of the mixed layer, but there appears to be a good reason for this disparity. The model predicts relatively dense scattered clouds between 800 m and 1355 m (maximum liquid water content equal to 0.69 gm/kg) and the authors of Ref. 23 report stratocumulus clouds over as much as 80 percent of the area in the upper five hundred meters of the mixed layer. Since cloud water affected their temperature and humidity measurements, they attempted to stay out of the clouds while taking the data. Thus the data points represent the profiles in the cloud-free environment between the clouds while the prediction line represents an ensemble average including the clouds.

When there are no clouds present  $\overline{h_w}$  is positive at  $z_i$  while  $\overline{w_e}$  is negative as predicted by Eq. 17. However when clouds form in the upper portions of the mixed layer thermal radiation becomes important and destroys the similarity between temperature and humidity profiles. The curves shown in Figs. 4-6 include water vapor condensation and thermal radiation as detailed by Oliver et al. 1978. The short absorption depth of the infrared radiation within a cloud ensures that cooling is confined to a relatively thin layer next to the top of the cloud. Turbulent transport delivers the heat from down in the cloud to the cloud top to balance the radiational cooling at the top. Thus in the presence of a cloud  $\overline{h_w}/\overline{w_e}$  is positive at  $z_i$  even when  $\Delta\theta/\Delta H < 0$ .

## BOUNDARY LAYER WITH STRATUS CLOUD

A boundary layer over a large expanse of water capped by a subsidence inversion will turbulently ingest moisture from the surface. Long-wavelength cooling of the water-vapor-laden air may then lead to condensation somewhere within the layer. In an expansive basin or region influenced only by advection in the form of a steady subsidence, a periodic steady state may form in which a solar driven diurnal cycle exists about a mean boundary layer state with a steady mean inversion height controlled by the radiative conditions (season and latitude), surface temperature, and upper conditions (wind, water content and subsidence) set by the larger circulation. Such an episode was illustrated by Oliver, et al. 1978 for conditions approximating the summer stratus layer along and off the coast of California.

The conditions for this illustration were selected to generally conform to the conditions described by Neiberger (1944) and more recently observed by Mack et al. (1974). Surface boundary conditions are established for a fixed temperature sea state of  $17^{\circ}\text{C}$ , surface water mixing ratio at saturation, and surface roughness determined by Froude scaling. Radiation conditions are for latitude  $40^{\circ}\text{N}$  at summer solstice. Geostrophic conditions set an upper level wind,  $U_g$ , of  $10 \text{ m s}^{-1}$  and subsidence whose characteristic value is  $0.5 \times 10^{-5} \text{ s}^{-1}$  (Neiberger et al., 1961; Lilly, 1968). Initial conditions (which will be lost after several days of simulation) were selected to correspond to a mildly stable temperature profile of lapse rate  $\partial\theta_v/\partial z = 0.003^{\circ}\text{C m}^{-1}$  and clear sky with an initial relative humidity of 0.9. The calculation is begun shortly before sunset the first day and runs for six days. Behavior during daylight hours must be considered somewhat approximate in the present illustration because droplet scattering of direct solar radiation would reduce solar penetration into the cloud interior.

The quasi-periodic evolution of cloudiness in the boundary layer is shown in Fig. 8. The stratus grows both downward and upward during nocturnal periods and thickens until sunrise when the solar heating begins to disperse the stratus. Radiative cooling is dominant at the cloud top and produces an unstable lapse rate within the cloud. A correspondingly enhanced turbulence production is also maximum in nocturnal periods and in the upper portion of the cloud. The radiation cooling at the cloud top strengthens the capping inversion which oscillates up and down over the period of the diurnal cycle.

We note that the predicted cloud base in these diurnal cycles is highest in late afternoon and lowest in early morning (Fig. 8) while cloud top is highest in early morning and lowest in late afternoon. Correspondingly the inversion height is highest in early morning and lowest in later afternoon - a result which is opposite to that for inversion height cycles driven by solar heating in the cloud-free boundary layer (Lewellen et al., 1974). This predicted result is in accord with the stratus observations of Neiberger (1944) as well as those of Mack et al. (1974) in which they detected a diurnal variation of inversion height in the presence of California coastal stratus which regularly showed maxima in the early morning. It is, of course, the radiative-turbulent drive of cloud-top cooling which allows the radiating layer to propagate condensation upward during the night while turbulence cools the cloud interior below.

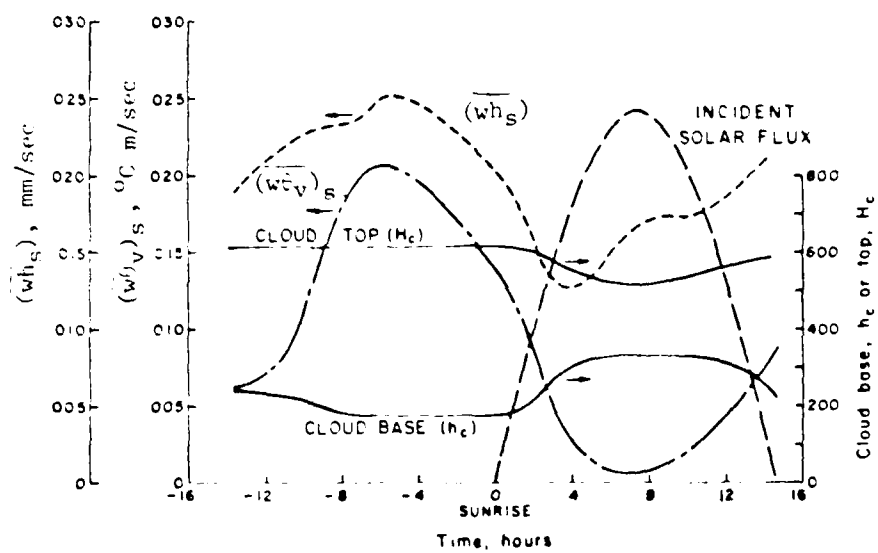


FIG 5 Diurnal variation of cloud base and top and heat and moisture fluxes at surface.  
(Oliver, Lewellen & Williamson 1978).



## RELATIVE CONTRIBUTION OF DIFFERENT SIZE EDDIES

The unstable boundary layer can often get organized into eddies which extend the full height of the mixed layer in the form of longitudinal roll vortices aligned close to the direction of the mean wind. An example of the clouds resulting from this motion are shown in Fig. 9. When the boundary layer is treated as spatially homogeneous then the motion of these roll vortices must appear as part of the turbulence. To examine the relative contributions of the smaller scale random turbulence and the relatively organized large scale rolls, a two dimensional calculation was performed in the  $(y,z)$  plane perpendicular to the axis of the rolls (Lewellen et al. 1979). Periodic boundary conditions were applied so that the domain covers a wavelength  $\lambda$  in the  $y$  direction. The vertical domain extended from the surface (represented by an effective roughness  $z_0$ ) to slightly above the capping inversion. The coordinate system permits the horizontal roll vortices to appear as part of the ensemble mean motion when calculating the unsteady flow in the unstable boundary layer.

The numerical code partitions the energy between the mean background motion which is a function of the vertical coordinate only; the mean quasi-periodic, two-dimensional, roll vortex motion which is a function of  $z$  and  $y$ ; and the more random turbulent motion which, although three-dimensional in character, is only a function of  $y$  and  $z$  in the mean. The energy in the organized roll motion varies with the ratio of the wavelength,  $\lambda$ , of the roll to the inversion height  $z_i$ , the instability of the layer as measured by the ratio of the Monin-Obukhov length,  $L$ , to  $z_i$ , and the angle,  $\alpha$ , between the roll axis and the geostrophic wind. Figure 10 illustrates the cross-sectional structure of the stream function of the roll motion for an angle of  $-10^\circ$ ,  $\lambda/z_i = 3$  and  $L/z_i \approx -0.1$

AD-A090 576

AERONAUTICAL RESEARCH ASSOCIATES OF PRINCETON INC NJ F/G 4/2  
1980 STATUS REPORT ON LOW-LEVEL, ATMOSPHERIC TURBULENCE MODEL F--ETC(U)  
JUL 80 W S LEWELLEN, D A OLIVER, R D SULLIVAN N00019-79-C-0366  
ARAP-420 NL

UNCLASSIFIED

2 of 2  
AD  
A090576



END  
DATE  
FILMED  
11 80  
DTIC



Plate 3 Apollo photograph of Georgia Coast, 1700Z, from 125 miles high. (From Brown 1974).

Fig. 9

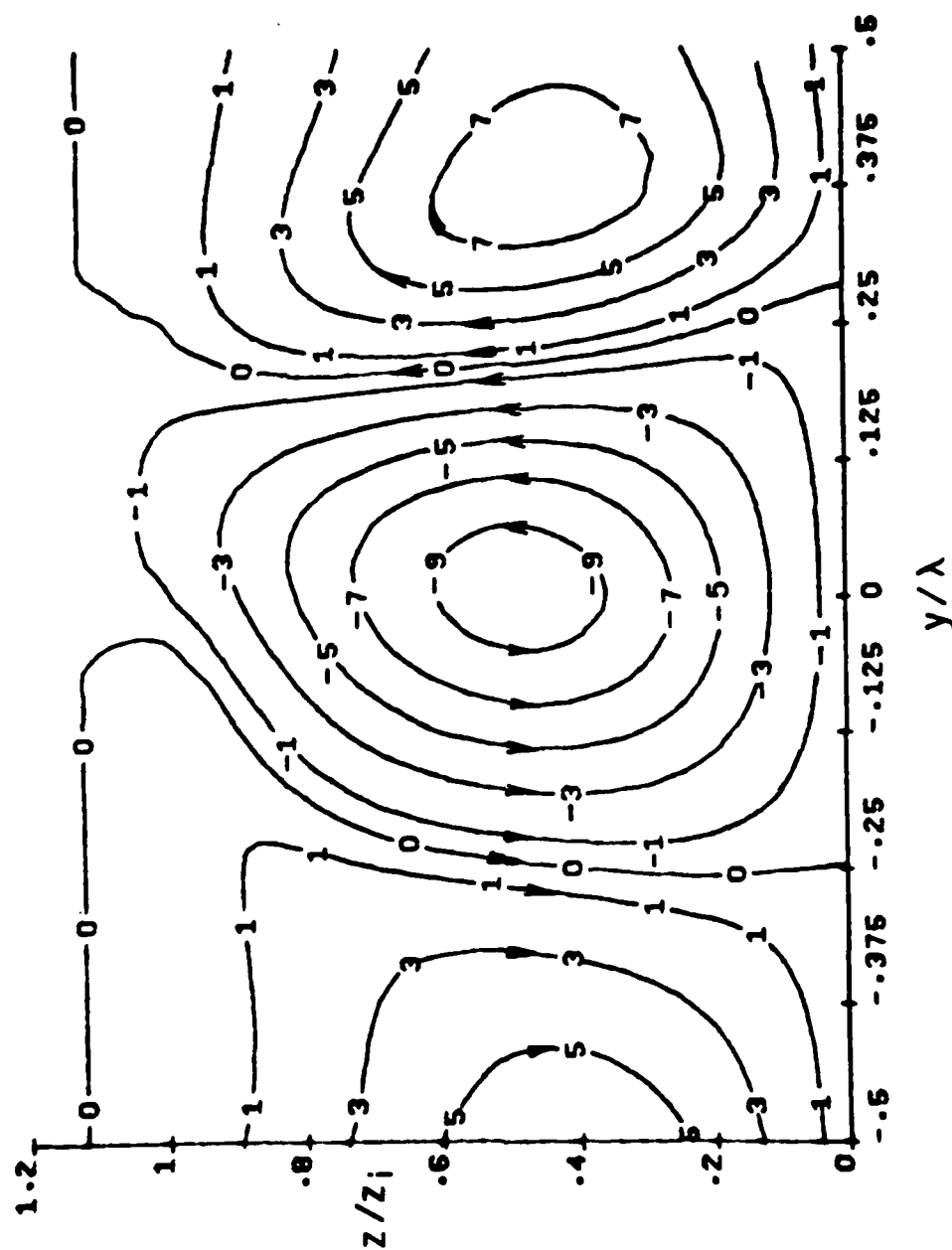


Fig. 10. Roll stream function contours for the example case of  $\alpha = -10^\circ$ ,  $\lambda/z_i = 3$ ,  $L/z_i = -0.1$ . The profiles are normalized by a maximum value  $\Delta\psi_{\max}/w_* z_i = 0.287$  ( $\Delta\psi = \psi - \langle \psi \rangle$ ), with  $\pm 9$  denoting  $\pm 90\%$  of maximum value;  $\pm 7$ ,  $\pm 70\%$ , etc. The arrows indicate flow direction.

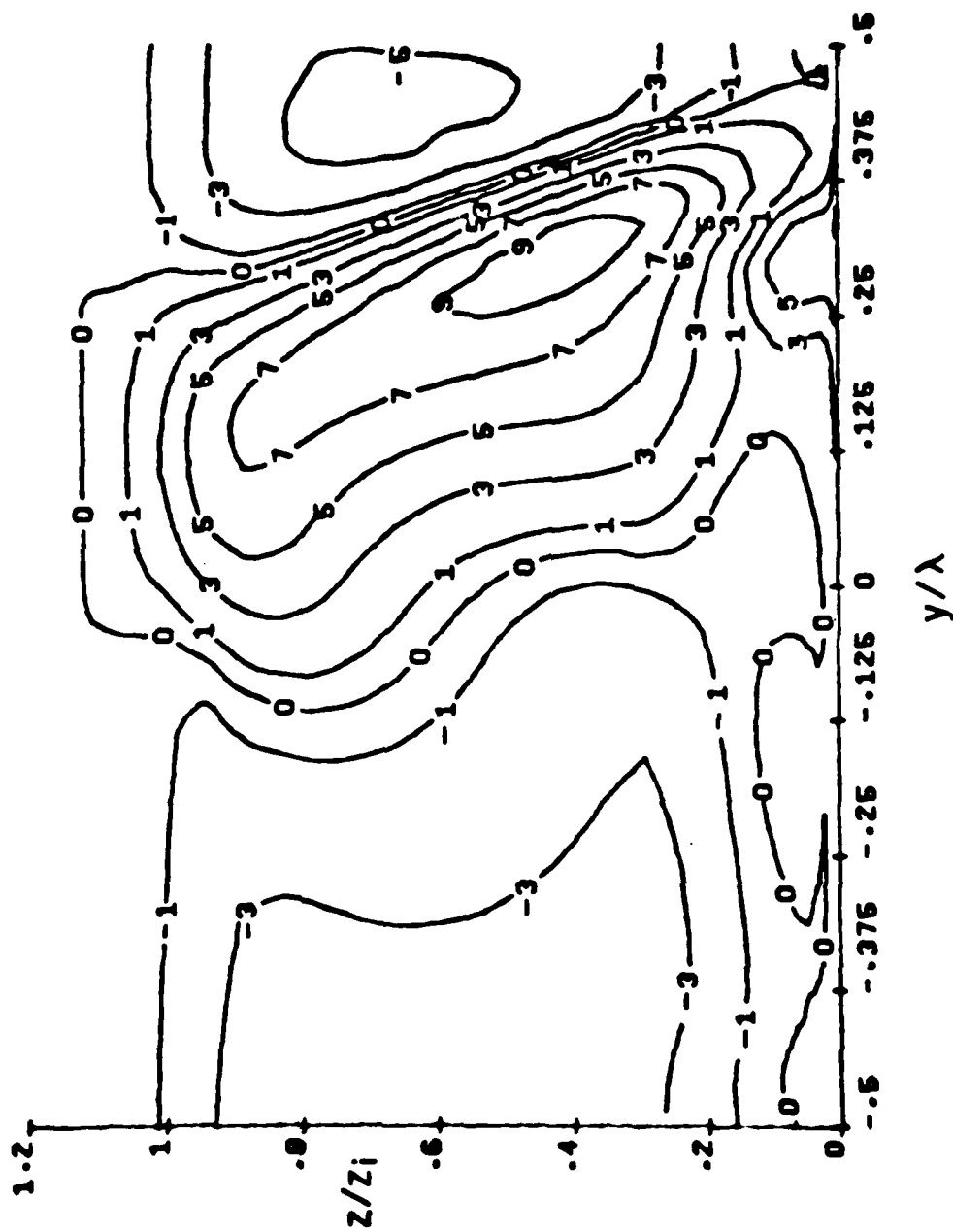


Fig. 11. Perturbation turbulence contours for the conditions given in Figure 10. Here  $\Delta q_{\max}^2/w_{*}^2 = 0.4$  is the normalizing maximum value.

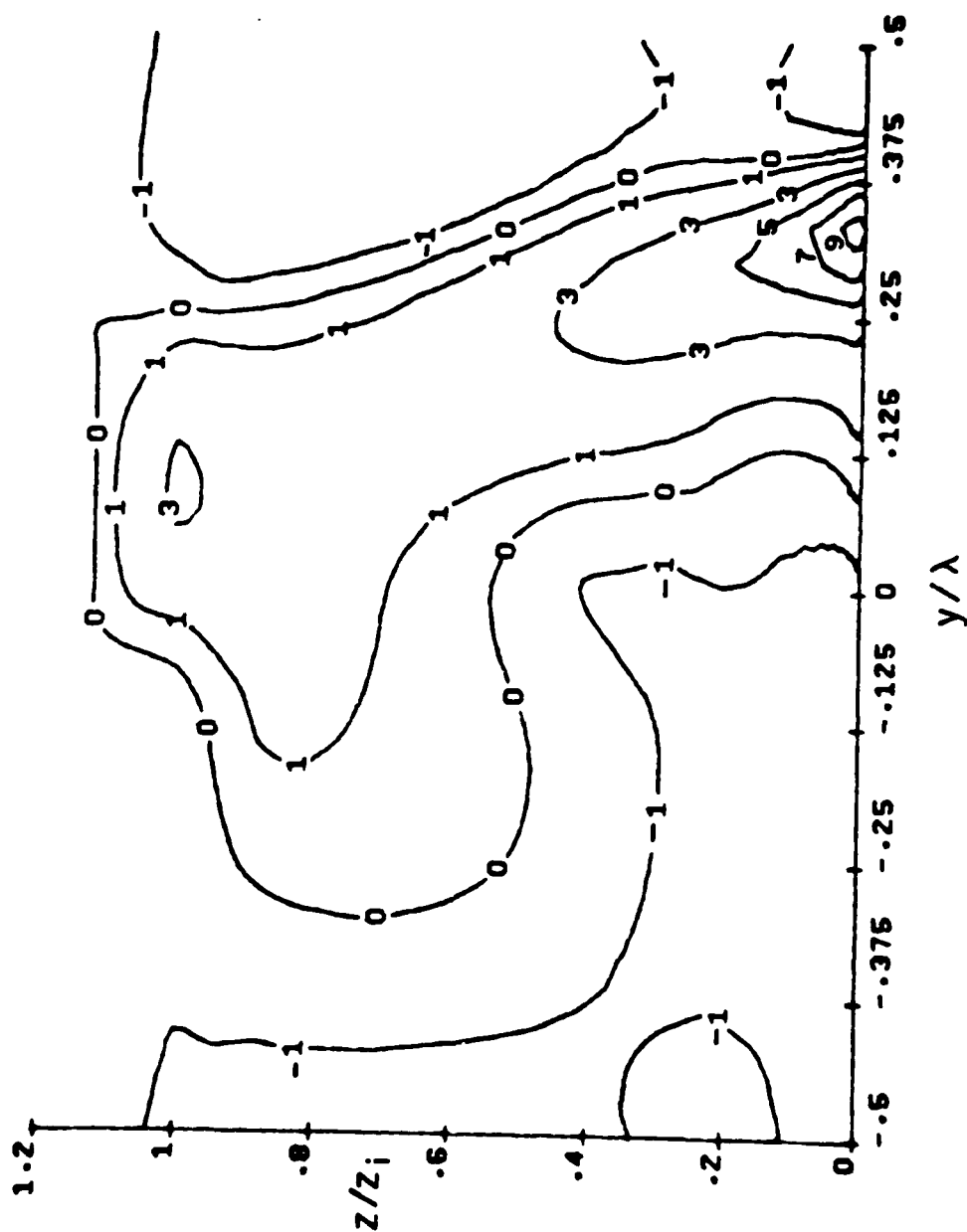


Figure 12. Roll species contours for the conditions of Figure 10. The normalizing maximum value is  $\Delta C_{w*}/cw_0 = 6.62$ .

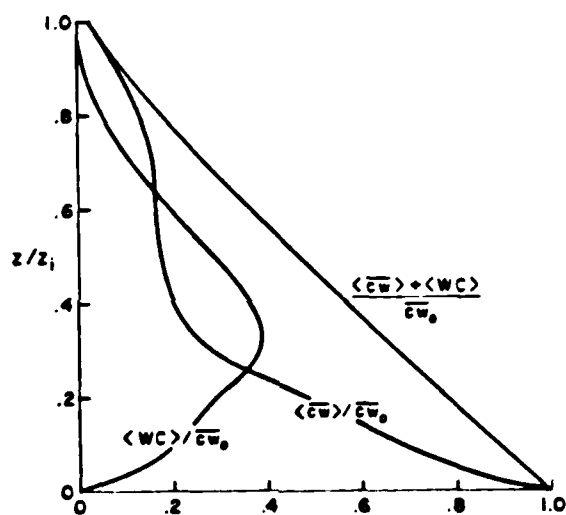


Figure 13. Composite  $y$ -averaged variation of the vertical species flux in the rolls  $\langle wC \rangle$  and the turbulence  $\langle \bar{c}w \rangle$  for the conditions of Figure 10. Here  $\bar{c}w_0$  is the species flux at  $z_0$ .

to approximate observations. Surface conditions are chosen appropriate for a sea surface at constant temperature. Results are scaled in terms of the characteristic velocity

$$w_* = \left( \frac{g}{T_0} \langle \overline{w\theta}_s \rangle z_i \right)^{1/3}$$

to minimize the influence of changes in  $\overline{w\theta}_s$ . (The angled bracket represents an average over  $y$ .) The geostrophic velocity is held at  $U_G = 10$  m/s throughout the calculations.

The corresponding cross-sectional structure of the turbulent kinetic energy and the humidity are shown in Figs. 11 and 12. The numerical results for the relative contributions of the mean roll motion and the roll modulated turbulence to the transport of momentum and heat compare reasonably (Lewellen et al. 1979) with the observations of LeMone (1976).

In Figs. 11 and 12 the background levels have been removed; hence  $\Delta q^2$  shows some regions of negative values. The updraft region shown in Fig. 10 produces a band with a spread of about  $0.25 \lambda$  which has greater than background  $C$  and  $q^2$ . The rest of the  $q^2$  region is dominated by a much broader area of less than average values of  $\Delta q^2$ . Figure 12 shows a noticeable, almost jet-like character to  $\Delta C$ . The heat flux is concentrated upward in the same region also, producing a temperature overshoot.

The vertical structure of the flux of a species such as humidity from the surface is shown in Fig. 13. At the surface the vertical transport is all carried by the small scale turbulence designated by  $\langle \overline{wc} \rangle$  but at  $z/z_i \approx 0.4$  approximately 2/3 of the vertical flux is contained in the mean roll motion designated by  $\langle WC \rangle$ . The heat flux structure is similar



(Lewellen, et al. 1979) except for an undershoot in  $\langle W \rangle$  above  $z/z_i \approx 0.75$  forced by the capping inversion.

As illustrated in Fig. 9, the most common way of visualizing the organization of the mixed layer into a longitudinal roll-vortex structure is the observation of cloud streets. Figure 14 shows the relationship between liquid-water-content contours and streamlines of the roll motion. The case shown in Figure 14 is somewhat different from that detailed in Figs. 10-13. In the calculation for the earlier figures the species  $C$  transported from the surface is treated as a passive tracer. For the calculation of Fig. 14, the species was interpreted as humidity and allowed to condense under appropriate conditions. The subsequent energy release is responsible for the minor change in streamline appearance between Fig. 10 and Fig. 14.

When radiative cooling was added to the computation illustrated in Fig. 14, the cloudiness increased to a complete stratus condition. The subsequent strong increase in cooling from the top of the mixed layer forced a marked change in the roll structure. The wavelength decreased sharply and the resulting mismatch between the computational domain periodic conditions and the desired wavelength of the phenomenon destroyed most of the organization of the simulation.

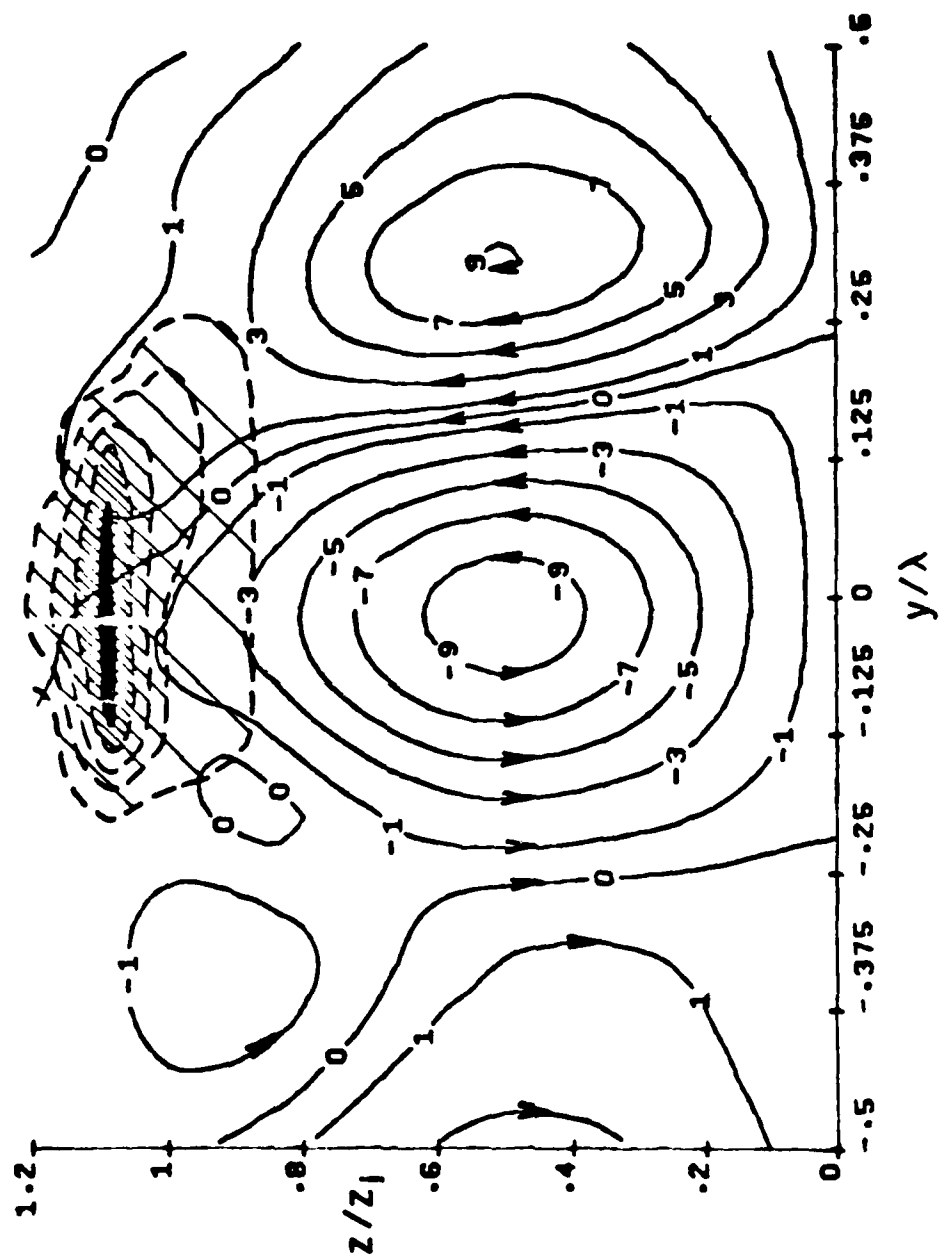


Figure 14. Longitudinal roll streamlines with liquid-water-content contours superimposed.

## REFRACTIVE INDEX FLUCTUATIONS

The basic turbulent correlations predicted by the model can be used to predict fluctuations in the refractive index for the propagation of electromagnetic waves. A parameter of major concern to the engineer is the Refractive Index Structure Function,  $C_n^2$ , which describes the intensity of refractive index fluctuations over the inertial subrange of turbulent eddies. The combination of primary variables, temperature and humidity variances and covariances required to compute  $C_n^2$  depends upon the wavelength being refracted. A formula for radar  $C_n^2$  was derived by Lewellen and Teske (1975).

$$C_{n(\text{radar})}^2 = 7.3 \times 10^{-3} \Lambda^{-2/3} \frac{p^2}{T^4} \left\{ \left( 1 + \frac{2B\bar{H}}{T} \right) \overline{e_V' e_V'} + \right. \\ \left. - 2 \left( 1 + \frac{2B\bar{H}}{T} \right) (0.61T_\infty + B) \overline{e_V' H'} + \right. \\ \left. \left[ B^2 + \left( 1 + \frac{2B\bar{H}}{T} \right) \left[ (0.61T_\infty)^2 + 2(0.61T_\infty)B \right] \right] \overline{H' H'} \right\}$$

where  $B = 7,730$ ,  $p$  is in atmospheres,  $T$  is  $^{\circ}\text{K}$  and  $\bar{H}$  is water vapor mixing ratio. It includes the influence of mean humidity level which is often important in the marine boundary layer, but was neglected by Wesely (1976). Burk (1979) deals with the prediction of acoustic, optical and microwave  $C_n^2$  throughout the planetary boundary layer using a model (Burk, 1977) similar to that presented here.

Figure 15 gives the contours of  $C_n^2$  predicted by our model for one set of conditions. (Sea surface temperature =  $20^{\circ}\text{C}$ ,  $U_g = 10$  m/sec,  $\alpha = 10$ ,  $z_i/L = 10$ ,  $\partial\theta/\partial z$  (above mixed layer) =  $.01^{\circ}/\text{m}$ ,  $H_\infty = 2.5$  g/Kg.) This set of conditions differs from that given in Figure 14 because we wished to show a cloud-free case. The figures show that the highest values

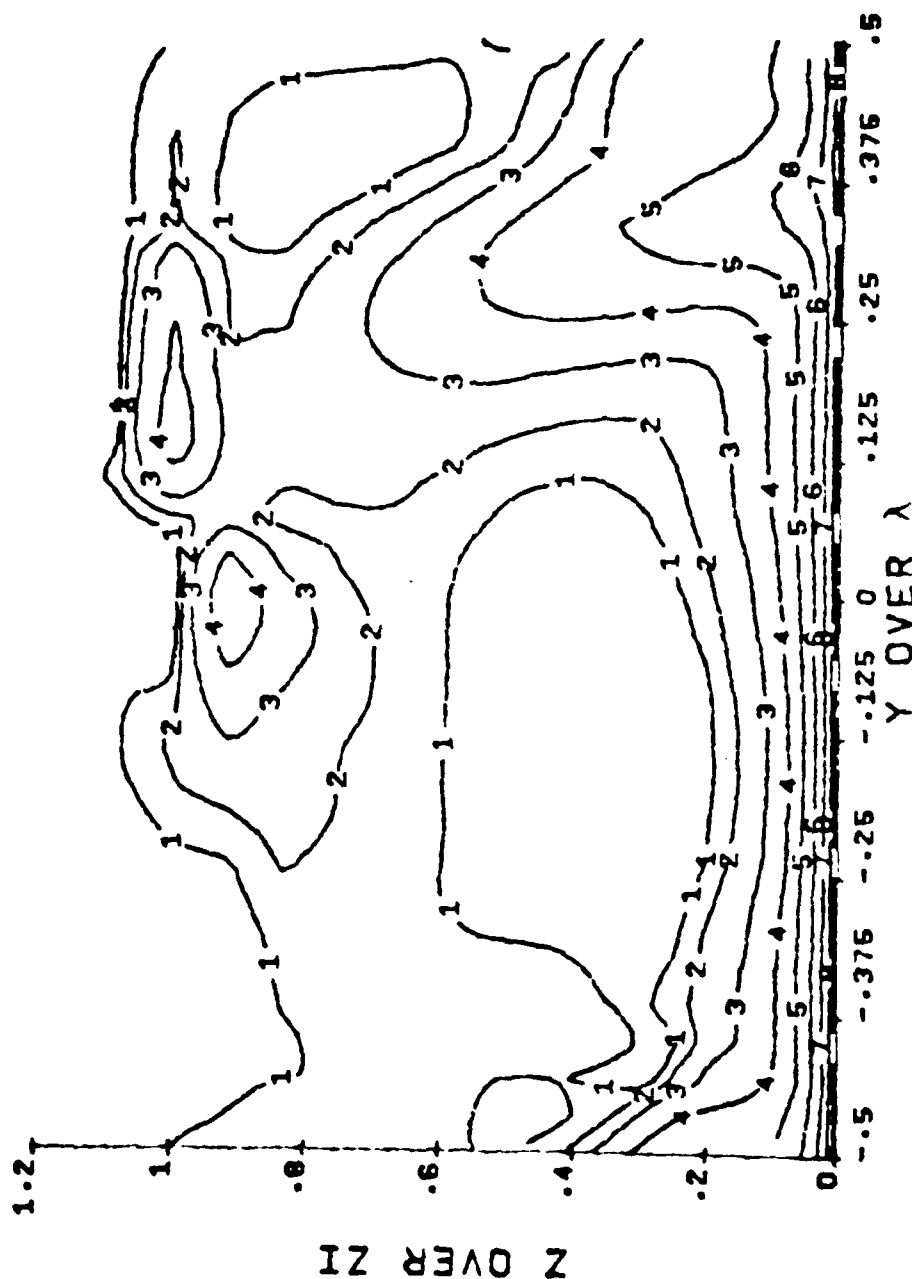


Figure 15. Contours of the radar refractivity structure function ( $C_n^2$ ) within the roll vortices predicted by a model run with  $T(\text{sea surface}) = 20^\circ\text{C}$ ,  $U_g = 10 \text{ m/sec}$ ,  $z_i/L \approx -10$ ,  $\alpha = 10^\circ$ ,  $\partial\theta/\partial z(\text{above inversion}) = .01 \text{ } ^\circ\text{C/m}$ ,  $\Delta h(\text{inversion}) \approx 2.5 \text{ g/Kg}$ . Contours labeled as  $2 \{ \frac{C_n^2}{\text{factor}} \}$  so that there is a factor of 2 difference between each of the contours.

of  $C_n^2$  occur near the surface and in the vicinity of the inversion. There is also considerable variation across the roll.

A comparison between one-dimensional and two-dimensional temperature and humidity variances shows that the major difference between one-dimensional and two-dimensional predictions occurs in the region of the inversion.

## CONCLUDING REMARKS

Viable means are available for estimating the distribution of water vapor and its variance in the atmosphere boundary layer. However, the techniques discussed in previous papers in this volume for observing water vapor in the atmosphere should provide the means for obtaining data which can be used to improve these models. This is particularly true in the neighborhood of the capping inversion and for the stable boundary layer. Although a number of simple entrainment models have been published for mixing across the inversion (e.g., Deardorff 1979 and Yamada and Berman 1979) none of these are very accurate for predicting the temperature and humidity fluctuations which occur there. A need exists for sufficiently complete data sets which can be used to either provide empirical correlations of mixing across this layer or to test the validity of second-order closure models such as the one described herein.

Comparisons between the results of two-dimensional and one-dimensional simulations of the same mixed layer problem (Lewellen et al., 1979) lead to ideas as to how the one-dimensional model may be improved by incorporating some features of an anisotropic length scale. We are currently attempting to complete this model modification. Alternative approaches to improving the model are being pursued by others (e.g., Lumley et al, 1978; Wyngaard, 1979; Gibson and Launder, 1978).

## REFERENCES

- Brost, R.A. and Wyngaard, J. C., 1978: A Model Study of the Stably Stratified Planetary Boundary Layer, *J. Atmos. Sci.*, 35, 1427-1440.
- Brown, R. A., 1974: Analytical Methods in Planetary Boundary-Layer Modeling, Halsted Press, New York.
- Burk, S. D., 1977: The Moist Boundary Layer with a Higher Order Turbulence Closure Model, *J. Atmos. Sci.*, 34, 629-638.
- Burk, S. D., 1979: Use of a Second Moment Turbulence Closure Model for Computation of Refractive Index Structure Coefficients, NAVENPREDRSCHFAC Tech. Report No. TR-78-04, 58 pp.
- Businger, J. A., Wyngaard, J. C., Izumi, Y., and Bradley, E. F., 1971: Flux-profile Relationships in the Atmospheric Surface Layer, *J. Atmos. Sci.*, 28, 181-189.
- Coantic, M. F., 1978: An Introduction to Turbulence in Geophysics and Air-Sea Interactions, AGARDograph #232.
- Deardorff, J. W., 1979: Predictions of Convective Mixed-Layer Entrainment for Realistic Capping Inversion Structure, *J. Atmos. Sci.*, 36, pp. 424-436.
- Donaldson, C. duP., 1973: Atmospheric Turbulence and the Dispersal of Atmospheric Pollutants, (EPA-R4-73-016a).
- Gibson, M. M. and Launder, B. E., 1978: Ground Effects on Pressure Fluctuations in the Atmospheric Boundary Layer, *J. Fluid Mechanics*, 86, pp. 491-511.
- Lemone, M. A., 1976: Modulation of Turbulence Energy by Longitudinal Rolls in an Unstable Planetary Boundary Layer, *J. Atmos. Sci.* 33, pp. 1308-1320.
- Lewellen, W. S., 1977: Use of Invariant Modeling, Handbook of Turbulence, Ed. Walter Frost and Trevor H. Moulden, (Plenum Publishing Corporation), Vol. 1, pp. 237-280.
- Lewellen, W. S. and Teske, M., 1973: Prediction of the Monin-Obukhov Similarity Functions from an Invariant Model of Turbulence, *J. Atmos. Sci.*, 30, No. 7, pp. 1340-1345.
- Lewellen, W. S. and Teske, M. E., 1975: Development of a Low Level Atmospheric Turbulence Model for Marine Environments, A.R.A.P. Report No. 255.
- Lewellen, W. S. and Teske, M. E., 1976: Second-Order Closure Modeling of Diffusion in the Atmospheric Boundary Layer, *JBLM*, 10, 69-90.

- Lewellen, W. S., Teske, M., Donaldson, C. duP., 1974: Turbulence Model of Diurnal Variations in the Planetary Boundary Layer, Proceedings 1974 Heat Transfer and Fluid Mechanics Institute (L. R. Davies and R. E. Wilson, eds.), Stanford University Press, Stanford, California, pp. 301-319.
- Lewellen, W. S., Teske, M. E., Oliver, D. A., Sheng, Y. P., and Segur, H., 1979: 1979 Status Report on Low-Level Atmospheric Turbulence Model for Marine Environments, A.R.A.P. Report No. 385.
- Lilly, D. K., 1968: Models of Cloud-Topped Mixed Layers Under a Strong Inversion, Quart. J. Roy. Meteor. Soc., 94, pp. 292-309.
- Lumley, J. L., Zeman, O., and Siess, J., 1978: The Influence of Buoyancy on Turbulent Transport, J. Fluid Mechanics, 84, pp. 581-597.
- Mack, E. J., Katz, U., Rogers, C., and Pilié, 1974: The Microstructure of California Coastal Stratus and Fog at Sea, Rep. CJ-5405-M-1, Calspan Corp.
- Neiburger, M., 1944: Temperature Changes During Formation and Dissipation of West Coast Stratus, J. Meteor., 1, pp. 29-41.
- Neiberger, M., Johnson, D. S., Ehnien, C., 1961: Studies Over the Eastern Pacific Ocean in Summer, I, the Inversion Over the Eastern North Pacific Ocean, Univ. Calif. Publ. Meteor., No. 1.
- Oliver, D. A., Lewellen, W. S., and Williamson, G. G., 1978: The Interaction Between Turbulent and Radiative Transport in the Development of Fog and Low-Level Stratus, J. Atmos. Sci., 35, No. 2, pp. 301-316.
- Smith, S. D., 1974: Eddy Flux Measurements Over Lake Ontario, JBLM, 6, pp. 235-253.
- Thom, A. S., 1975: Momentum, Mass and Heat Exchange of Plant Communities, Vegetation and the Atmosphere, 2, pp. 57-109.
- Verma, S. S., Rosenberg, N. J., and Bladd, B. L., 1978: Turbulent Exchange Coefficients for Sensible Heat and Water Vapor under Advective Conditions, J. Applied Meteorology, 17, 330-338.
- Wesely, M. L., 1976: The Combined Effect of Temperature and Humidity Fluctuations on Refractive Index, J. Appl. Meteor., 15, pp. 43-49.



Wyngaard, J. C., 1979: The Atmospheric Boundary Layer-Modeling and Measurements, Proceedings of the Second Symposium on Turbulent Shear Flows, Imperial College, London, pp. 13.25 - 13.30.

Wyngaard, J. C., Pennell, W. T., Lenschow, D. H., and LeMone, M. A., 1978: The Temperature-Humidity Covariance Budget in the Convective Boundary, J. Atmos. Sci., 35, pp. 47-58.

Yamada, T., 1979: Prediction of the Nocturnal Surface Inversion Height, J. Appl. Meteor., 18, pp. 526-531.

Yamada, T. and Berman, S., 1979: A Critical Evaluation of a Simple Mixed-Layer Model with Penetrative Convection, J. Applied Meteorology, 18, pp. 781-786.

Yamada, T. and Mellor, G. L., 1975: A Simulation of the Wangara Atmospheric Boundary Layer Data, J. Atmos. Sci., 32, pp. 2309-2329.

Zeman, O., 1979: Parameterization of the Dynamics of Stable Boundary Layers and Nocturnal Jets, J. Atmos. Sci., 36, pp. 792-804.

APPENDIX C

Micrometeorological Applications of a  
Second-Order Closure Model of  
Turbulent Transport

by

W. S. Lewellen, M. E. Teske, and Y. P. Sheng

(To appear in Published Proceedings of 2nd Turbulent Shear  
Flows Symposium.)

PRECEDING PAGE BLANK-NOT FILMED

# Micrometeorological Applications of a Second-Order Closure Model of Turbulent Transport

W. S. Lewellen, M. E. Teske, and Y. P. Sheng

Aeronautical Research Associates of Princeton, Inc.  
50 Washington Road, P. O. Box 2229, Princeton, N. J. 08540, USA

## Abstract

Recent applications of the turbulent transport model originally developed by Donaldson to some problems of practical importance in micrometeorology are discussed. Four particular examples considered are the local boundary layer gust front emanating from a thunderstorm, the low-level wind and turbulent distributions of a tornado, the transport of momentum, heat and species within a surface layer canopy, and longitudinal roll vortices in the unstable planetary boundary layer. Results for the last example are discussed in some detail. Comparisons are made between a one-dimensional and a two-dimensional computation of this phenomenon.

## List of Symbols

$C$	Mean species concentration	$x, y$	Horizontal coordinates
$c$	Species fluctuation	$z$	Vertical coordinate
$g$	Gravitational acceleration	$z_1$	Height of mixed layer
$H$	Height of vegetation canopy	$z_0$	Surface roughness height
$h$	Height of numerical grid	$\alpha$	Angle between the roll axis and the geostrophic wind
$L$	Monin-Obukhov length	$\delta_{ij}$	Kronecker delta
$P$	Mean pressure	$\epsilon_{ijk}$	Alternating tensor
$q$	Root-mean velocity fluctuation	$\Lambda$	Turbulent macroscale
$r$	Radius	$\lambda$	Wavelength of the roll
$R$	Radius at which maximum swirl occurs	$\Theta$	Mean temperature
$t$	Time	$\theta$	Temperature fluctuation
$U_i, U_j, U_k$	Mean velocity components	$\theta_s$	$-\overline{w\theta}/U_s$
$u_i, u_j, u_k$	Fluctuating velocity components	$\sigma_u$	Standard deviation of longitudinal wind velocity
$U_G$	Geostrophic wind	$\sigma_w$	Standard deviation of vertical wind velocity
$U_f$	Friction velocity	$\nu$	Kinematic viscosity
$U$	Mean longitudinal velocity	$\rho$	Density
$u$	Fluctuating longitudinal velocity	$\psi$	Stream function
$V$	Mean transverse velocity	$\Omega$	Earth's rotation
$v$	Fluctuating transverse velocity		
$W$	Mean Vertical velocity		
$w$	Fluctuating vertical velocity		
$w_s$	Characteristic velocity for free convection		

## Introduction

The basic turbulent transport model used in these applications is that outlined by *Donaldson* [1] and described in detail by *Lewellen* [2]. Simple closure approximations were made to the equations for the ensemble-averaged, single-point, second-order moments of the fluctuating variables. The theme of the present paper is to discuss the various applications rather than to rederive the model. Since invariance is an essential feature of the model, the same modeling coefficients are used for all the applications. The basic modeled equations are given in the Appendix. Although this simple closure cannot be expected to faithfully represent all of the information present in complex micrometeorological turbulent flows, the added physics incorporated in the second-order correlation equations permits an influence of such phenomena as buoyancy and rotation to be calculated directly without resorting to ad hoc eddy viscosity fixes.

The first three examples will only be discussed very briefly, but the fourth will be presented in greater detail because it not only helps to illuminate the influence that roll vortices exert on the turbulent transport of momentum, heat and species, but also the strong and weak points of the basic turbulence closure model.

## Thunderstorm Gust Front

The gust front caused by the cold outflow emanating from a thunderstorm has been modeled with an axisymmetric implementation of our turbulence model [3]. The simulated flowfield is illustrated in Fig. 1. We idealize the outflow from the thunderstorm as a cold jet of temperature ( $\theta$ ) impinging normal to the ground, released at a height  $z_{max}$  with vertical velocity ( $w$ ). The temperature defect below the ambient temperature is caused by evaporation of falling rain by relatively dry air at some altitude  $z > z_{max}$ .

The primary variables in this simulation are the temperature defect (below ambient) of the jet, its diameter, and the height at which it is released. The larger scale updraft within which the downdraft is embedded will play a role in retarding the late-time gust front within the computational domain, but should not be a critical factor as long as the inflow velocity is smaller than the resulting internal simulated velocities. The other critical parameters are the surface temperature, the surface roughness, and the stability of the ambient atmosphere. In an effort to evaluate hazardous conditions for aircraft operations, a sensitivity analysis has been performed on the gust front as a function of five different dimensionless physical parameters [4,5].

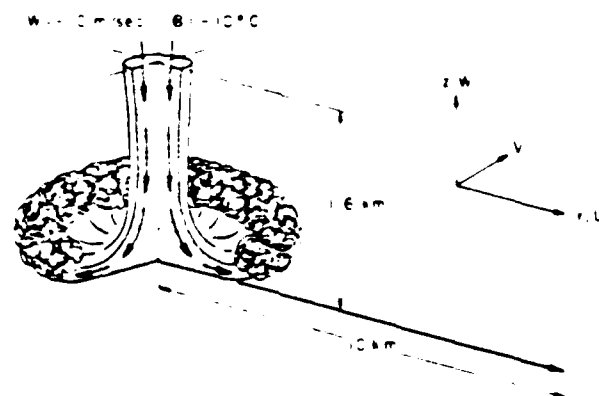


Fig. 1. Coordinate system for the axisymmetric radial thunderstorm gust front simulation

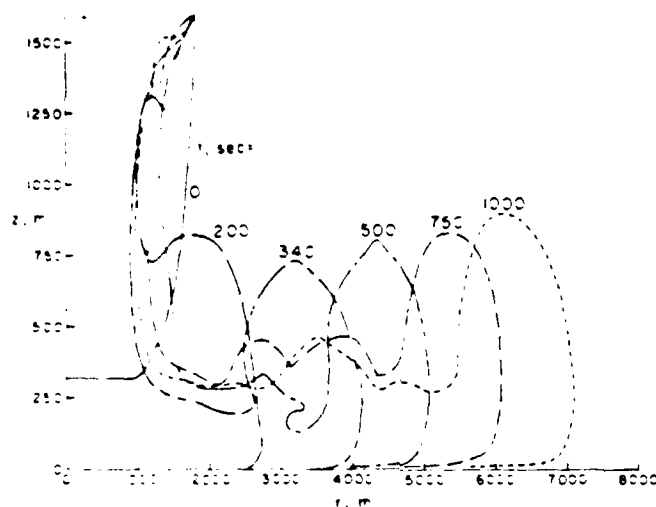


Fig. 2. Isotherms of constant temperature defect ( $\Theta = -2^\circ\text{C}$ ) at several times after initialization

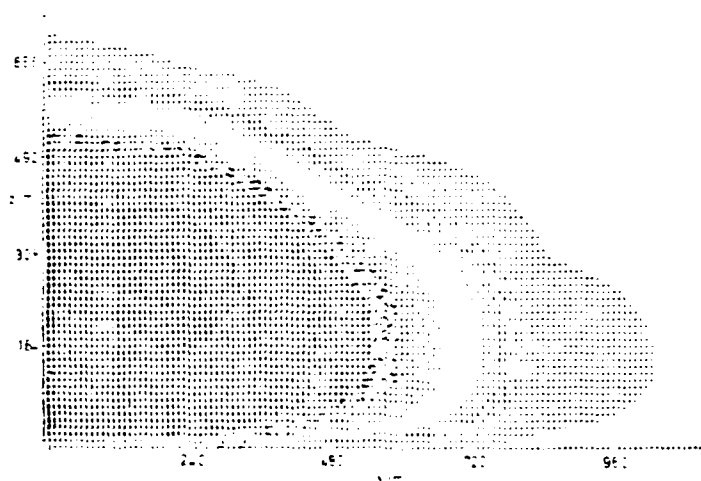


Fig. 3. Model simulation of the leading edge of a gust front when visualized in terms of temperature defect intensity

One way to follow the structure of the developing gust is to observe the movement of a fixed temperature value line, in this case  $\Theta = -2^\circ\text{C}$ , as shown in Fig. 2 for the simulation sketched in Fig. 1. At  $t = 0$  the initial linear profile is shown, but by  $t = 200$  s the structure has developed into a moving front. At  $t = 340$  s the front has torn away from the downdraft region. At later times the strength of the gust decreases as the effect of the area change becomes more important. However, the height of the gust appears to grow slowly, so that by  $t = 1,000$  s the  $\Theta = -2^\circ\text{C}$  line reaches nearly 1 km in altitude at a distance of nearly 8 km



Fig. 4. The leading edge of a thunderstorm gust front as marked by dust (Photo by Andrew Watson, Miami, Florida, 1975)

from the source centerline. The front is still quite strong at this point, and is moving outward at approximately 2.6 m/s.

When our numerically simulated front is visualized in terms of the temperature defect intensity, the leading edge appears as shown in Fig. 3. There is a very strong qualitative similarity between this picture and the gust front as visualized by dust in Fig. 4 (also see picture in [6]). The quantitative predictions of maximum mean velocity, velocity shear and variance also appear consistent with available observations.

### Tornado Boundary Layer

The strongest winds occurring in nature are those in a tornado. In order to estimate wind loads on structures, we have modeled the tornado boundary layer [7] again using the axisymmetric version of our basic turbulent transport model. Here we have chosen a computer simulation which shows a resemblance to the 1974 Xenia, Ohio tornado. The domain's outer radius and top are both placed at 400 m. The surface roughness is taken to be large (0.4 m) to correspond

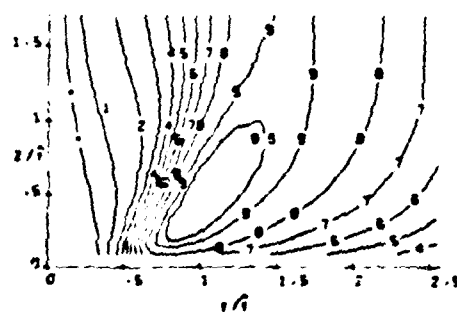


Fig. 5. Mean tangential velocity contours as predicted by an axisymmetric tornado model. Contours labeled in tenths of maximum  $V'$ , and radial and vertical coordinate normalized by the radius at which  $V'_{max}$  occurs

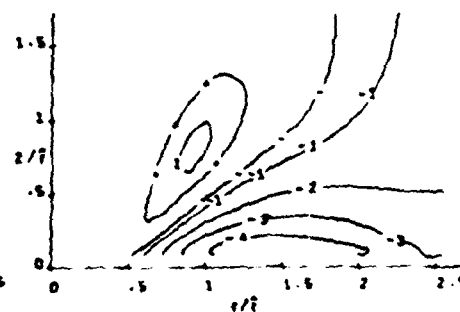


Fig. 6. Mean radial velocity contours for the same conditions as Fig. 5

to a relatively urban area. All components of the velocity are specified at the outer radius in-flow boundary and relatively free zero slope conditions applied at the top of the domain.

The mean tangential and radial velocity field is given in Figs. 5 and 6. The velocities are normalized by the maximum tangential velocity which occurs at  $r \approx 180$  m,  $z \approx 100$  m. Currently, boundary conditions are not known precisely enough for the absolute value of the maximum velocity to be predicted by the model. However, from photogrammetric analyses, it appears the tangential velocity should be scaled by a maximum value of approximately 100 m/s.

A dominant feature of the flowfields computed to date [8, 9] is that the maximum winds occur at quite low altitudes. The surface layer plays the rather paradoxical role of increasing the velocity in the neighborhood of the ground at small radii, before actually reducing the velocity to zero at the surface. The strong radial inflow in the surface layer permits the streamlines to penetrate to smaller radii here than at higher altitudes. Even without total conservation of angular momentum, this permits higher swirling velocities to develop. The simulation also predicts that the r.m.s. average of the velocity fluctuations reaches values as high as  $0.3 U_{\max}$ . This large magnitude of the fluctuating velocities indicates that they should be considered in setting design criteria. The maximum damage will most likely occur where the fluctuating velocities add to the mean velocity.

### Flow Within a Surface Canopy

A canopy of vegetation presents a complex lower boundary for atmospheric flows. For flow well above this canopy, it is usually adequate to characterize the boundary in terms of only an aerodynamic roughness,  $z_0$ . But for flow within the canopy itself, a more detailed representation is required. Our motivation for detailing this flow is to aid in the prediction of the dry deposition of gaseous  $\text{SO}_2$  and particulate sulfate.

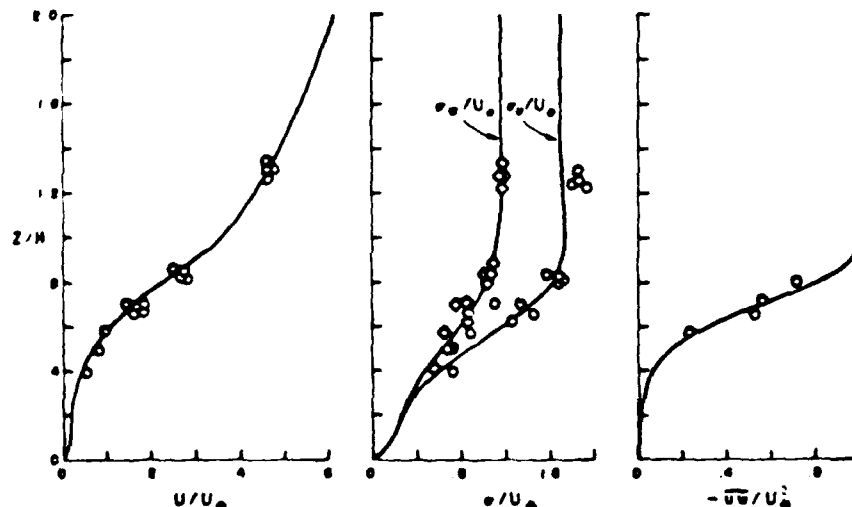


Fig. 7. Comparison of A.R.A.P. model prediction with data from Shaw et al. [11, 12] in and above a corn canopy, where  $H$  is canopy height,  $U_0$  the friction velocity above the canopy,  $U/U_0$  the normalized mean longitudinal wind velocity,  $\sigma_u/U_0$  and  $\sigma_w/U_0$  the dimensionless standard deviations of the longitudinal and vertical velocities, and  $(-uw/U_0^2)$  the dimensionless Reynolds stress.

A second-order closure model for canopy flow has recently been presented by Wilson and Shaw [10]. The principal difference between their model and ours is that we consider heat and species transport as well as momentum transport. We also use a somewhat more general representation of the drag per unit volume of the vegetation. The comparison of the mean distributions of velocity, Reynolds stress and velocity variance predicted by our model are compared with some limited data for a corn canopy [11, 12] in Fig. 7. Although detailed plant area densities must be given for any type of vegetation, the model can predict the variation in surface layer heat and species transport as a function of surface Reynolds number ( $U_s z_0/\nu$ ), Prandtl number and Schmidt number for any given plant area density distribution [13].

### Roll Vortices in the Planetary Boundary Layer

The final example, which we will discuss in more detail, is that of computing the longitudinal roll vortices which often occur in the unstable planetary boundary layer [14]. This boundary layer feature can often be visualized as in Fig. 8 by the streets of clouds which occur at the top of the upflow region between the roll vortices. The simulation is performed on a two-dimensional grid, stretching over a wavelength  $\lambda$  in the  $y$  direction, and from the surface (represented by an effective hydrodynamic roughness  $z_0$ ) to the total height  $h$  of the numerical grid. At a position  $z_i < h$ , the temperature profile is damped back to its background gradient, capping the domain and forcing  $z_i$  to become the inversion height. All mean variables and turbulence quantities are initialized with profiles from a compatible boundary layer solution of our one-dimensional code. The spatially homogeneous one-dimensional code necessarily treats the motion arising from the roll vortices as a part of the turbulence. Periodic boundary conditions are applied to the two-dimensional Cartesian version of our model. This permits horizontal roll vortices to appear as part of the ensemble mean motion when calculating the unsteady flow in the unstable boundary layer.

The numerical code is free to partition the energy between the mean background motion which is a function of the vertical coordinate only; the mean quasi-periodic, two-dimensional, roll vortex motion which is a function of  $z$  and  $y$ ; and the more random turbulent motion which, although three-dimensional in character, is only a function of  $y$  and  $z$  in the mean. The energy



Fig. 8. View of cloud streets over the coast of Georgia as seen by Apollo [14]



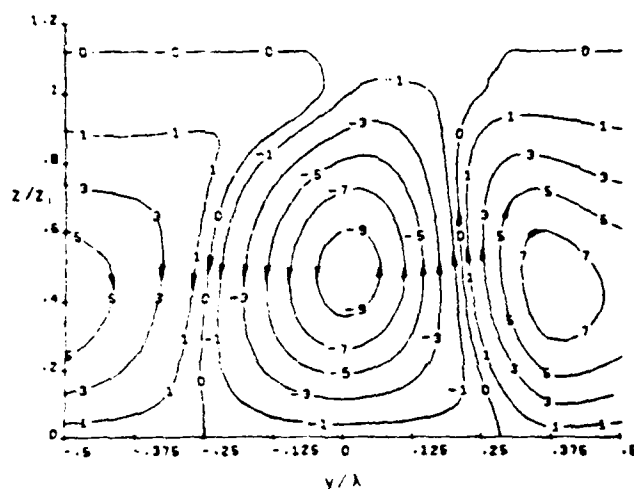


Fig. 9. Roll stream function contours for the example case of  $\alpha = -10^\circ$ ,  $\lambda/z_i = 3$ ,  $\Delta_{\max}/z_i = 0.1$ . The profiles are normalized by a maximum value  $\Delta_{\max}/w_* z_i = 0.28$  ( $\Delta_{\max} = 1.0$ ), with  $\pm 9$  denoting  $\pm 90^\circ$  of maximum value,  $\pm 7$ ,  $\pm 70^\circ$ , etc. The arrows indicate flow direction.

in the organized roll motion varies with the ratio of the wavelength,  $\lambda$ , of the roll to the inversion height  $z_i$ , the instability of the layer as measured by the ratio of the Monin-Obukhov length,  $L$ , to  $z_i$ , and the angle between the roll axis and the geostrophic wind. Figure 9 illustrates the typical cross-sectional structure of the stream function of the roll motion for an angle of  $-10^\circ$ ,  $\lambda/z_i = 3$  and  $L/z_i \approx -0.1$ . Surface conditions are chosen appropriate for a sea surface at constant temperature. Results are scaled in terms of the characteristic velocity

$$w_* = \left| \frac{g}{\Theta_0} \langle w \bar{\theta}_0 \rangle z_i \right|^{1/3}$$

to minimize the influence of changes in  $w \bar{\theta}_0$ . (The angled bracket represents an average over  $y$ .) The geostrophic velocity is held at  $U_G = 10$  m/s throughout the calculations. To maintain the roll structure, we impose periodic boundary conditions on all variables at  $y = \pm \lambda/2$ , so that whatever goes out one side will enter the other.

The corresponding cross-sectional structure of temperature, velocity, turbulent kinetic energy, and passive species released from the surface perturbations are shown in Figs. 10 through 13. The numerical results for the relative contributions of the mean roll motion and the roll modulated turbulence to the transport of momentum and heat compare reasonably (15) with the observations of LeMone [16].

Figures 10 through 13 show strongly similar results for differences above background average for  $U$ ,  $\Theta$ ,  $q^2$ , and  $C$ . Here the background levels have been removed; hence  $\Delta q^2$  shows some regions of negative values. What is obvious from all four plots is that the updraft region shown in Fig. 9 produces a band of less than background  $U$  and greater than background  $\Theta$ ,  $q^2$  and  $C$ . The typical spread of this region is about  $0.25 \lambda$ . The rest of the  $q^2$  region is dominated by a much broader area of less than average values of  $\Delta q^2$ . Figure 7 shows a noticeable, almost jet-like character to  $U$ , although it must be realized that  $\Delta U_{\max} = 0.096 \langle U \rangle_{\max}$  and may not be that easily detected. Consistent with this undershoot in  $\Delta U$  is an overshoot in  $\Delta \Theta$  (Fig 10), although there is also an overshoot coming down from near the inversion height on the downward side of the roll. A very broad region exists where  $\Delta \Theta$  is nearly zero, implying little variation of  $\Theta$  in  $y$ . These results are all consistent with LeMone's observation that the turbulence was largest where the vertical flux was upward. The heat flux is concentrated upward in the same region also, producing the temperature overshoot.

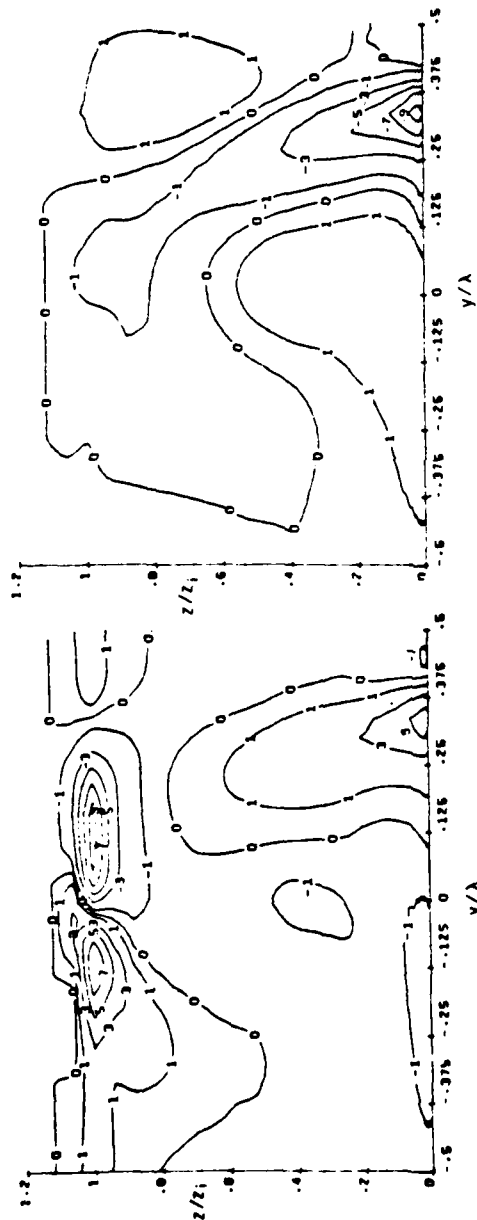


Fig. 10. Perturbation temperature contours for the conditions of Fig. 9. The normalizing maximum value is  $\Delta\theta_{\max}/w_0 = 10.4$

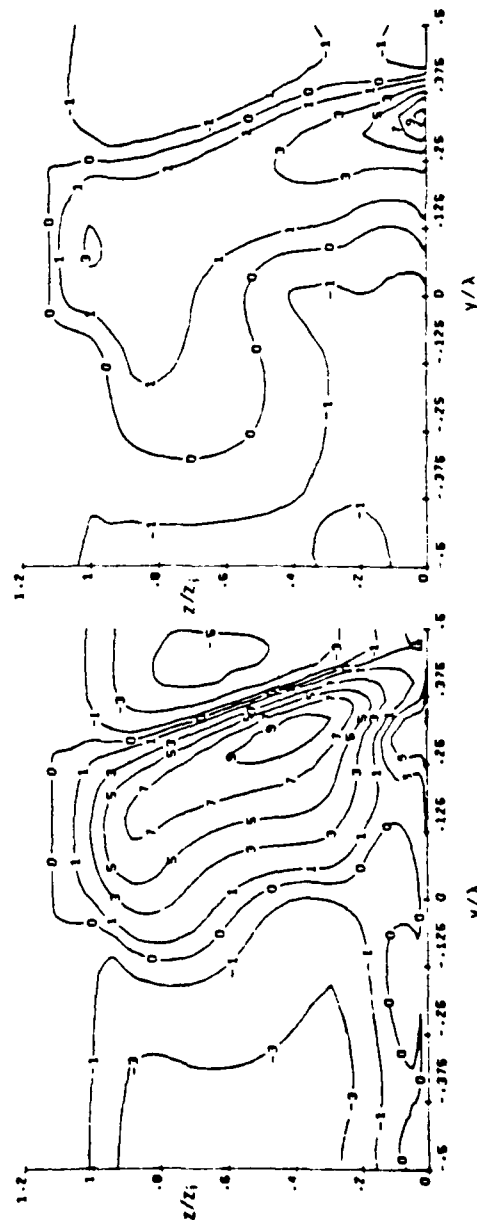


Fig. 11. Perturbation axial velocity contours for the conditions of Fig. 9. The normalizing maximum value is  $\Delta U_{\max}/w_0 = 1.09$

Fig. 12. Perturbation turbulence contours for the conditions given in Fig. 9. Here  $\Delta q_{\max}^2/w_0^2 = 0.4$  is the normalizing maximum value

Fig. 13. Roll species contours for the conditions of Fig. 9. The normalizing maximum value is  $\Delta C_{\max} w_0/\bar{w} = 6.62$

Fig. 13 shows the contour pattern of the roll-averaged  $\Delta C$ , showing it to be qualitatively similar to the transport of  $\Delta \Theta$  off the surface. No return transport exists, since  $C$  is assumed to go to a small value at the top. LeMone observed clouds near the top of the updraft regions of flow, but this observation should not be confused with our species results. The passive species is fairly uniform across the domain ( $\Delta C_{\max} = 0.050 \langle C \rangle_{\max}$ ).

If the closure modeling were exact, the one-dimensional (horizontally homogeneous) analysis of this problem, which averages over the periodic large eddy roll structure and treats the roll energy as part of the turbulent kinetic energy, would yield the same answer as obtained by horizontally averaging over the two-dimensional result. Since the two-dimensional computation allows the dominant large eddy structure to be determined, the closure modeling should be less critical in this computation than it is in the analogous one-dimensional computation. For this phenomenon, which has a strong two-dimensional character, our model represents an intermediate step between depending completely on closure modeling and depending on sub-grid

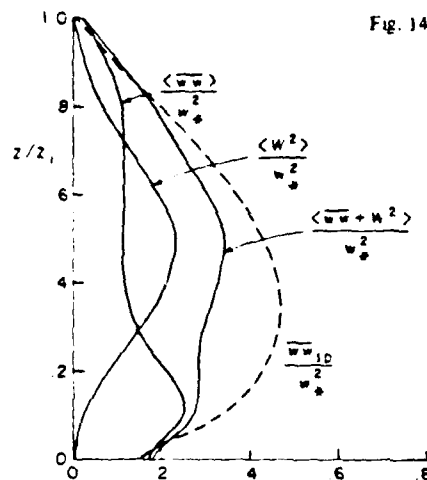


Fig. 14

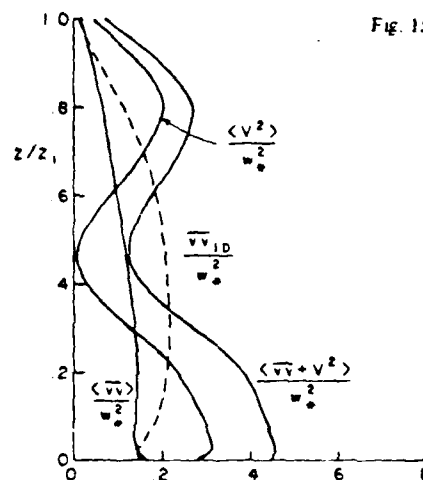


Fig. 15

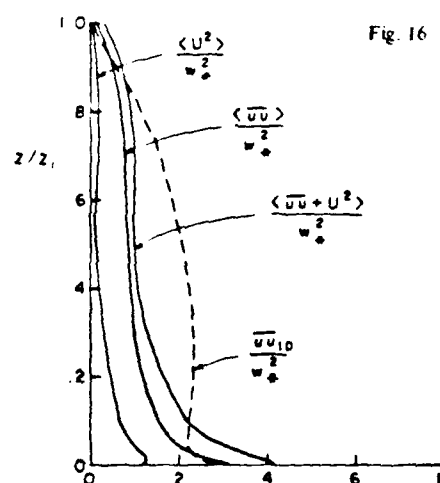


Fig. 16

Fig. 14. Comparison between the one-dimensional and two-dimensional predictions for vertical velocity variance. For the two-dimensional calculation, the y-averaged, large scale roll contribution is denoted by  $\langle \overline{w^2} \rangle$  and the smaller scale turbulence by  $\overline{w'^2}$ .

Fig. 15. Comparison between the one-dimensional and two-dimensional predictions for transverse velocity variance. For the two-dimensional calculation, the y-averaged, large scale roll contribution is denoted by  $\langle \overline{v^2} \rangle$  and the smaller scale turbulence by  $\overline{v'^2}$ .

Fig. 16. Comparison between the one-dimensional and two-dimensional predictions for longitudinal velocity variance. For the two-dimensional calculation, the y-averaged, large scale roll contribution is denoted by  $\langle \overline{u^2} \rangle$  and the smaller scale turbulence by  $\overline{u'^2}$ .

closure modeling [17]. Thus, the two-dimensional result can be used to check strengths and weaknesses of the one-dimensional model.

The separate components of the velocity variance are shown in Figs. 14 through 16. There is a reasonable comparison between the vertical variance predicted by the one-dimensional model and the spatial average of the two-dimensional results. But the other two components show significant differences.

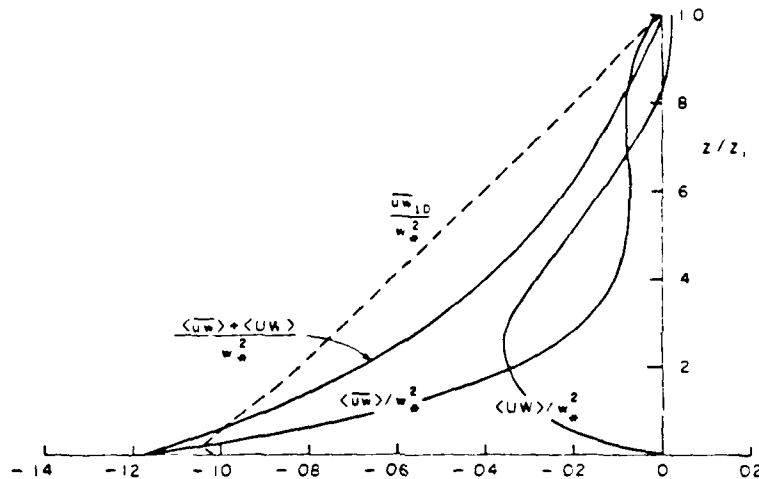


Fig. 17. Comparison between the one-dimensional and two-dimensional predictions for the vertical longitudinal momentum flux. The y-averaged roll contribution is denoted by  $\langle u w \rangle$  and the turbulent transport by  $\overline{u w}$ .

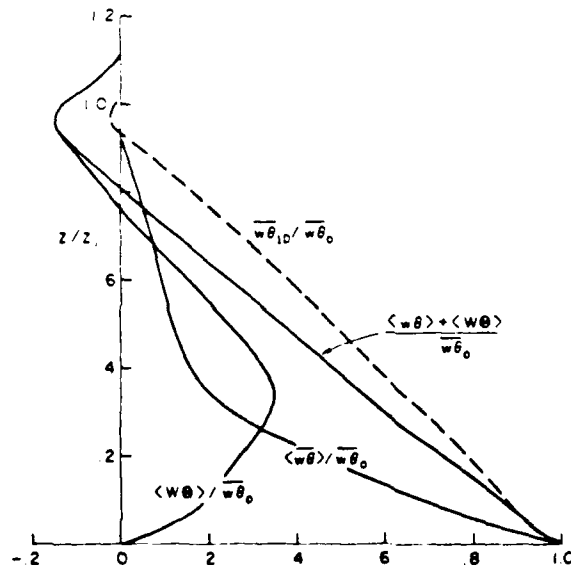


Fig. 18. Comparison between the one-dimensional and two-dimensional predictions for the vertical heat flux. The y-averaged roll contribution is denoted by  $\langle w \theta \rangle$  and the turbulent transport by  $\overline{w \theta}$ .

The analogous comparisons of the vertical momentum flux and the vertical heat flux are shown in Figs. 17 and 18. In the middle of the mixed layer, a major portion of the turbulent transport is carried by the large roll structure. In spite of this, the one-dimensional model is able to model the turbulent transport reasonably well except in the vicinity of the upper inversion. Both the one-dimensional and two-dimensional models predict a heat flux which is counter gradient over approximately one-half of the mixed layer depth. The two-dimensional model predicts a larger undershoot in the heat flux near the inversion. This seems to be associated with the fact that the two-dimensional model can account for more influence of the wave motion in the stable region than is represented in the one-dimensional model. This is perhaps shown better in Fig. 19 which shows the temperature variance. By far, the largest contribution to temperature variance at the top of the mixed layer is the wave motions induced by the large rolls. However, even the small scale turbulent variance is approximately a factor of 2 larger than that predicted by the one-dimensional model at  $z/z_i = 1$ .

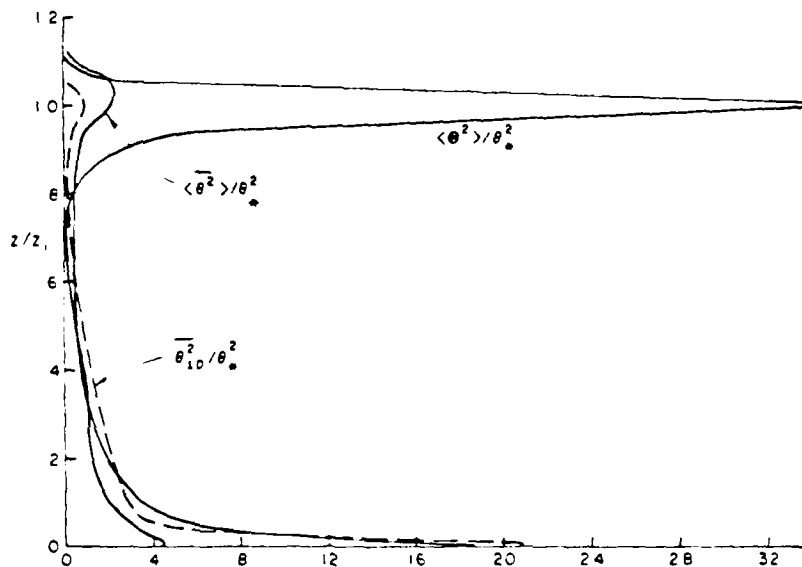


Fig. 19. Comparison between the one-dimensional and two-dimensional predictions for the temperature variance. The  $y$ -averaged roll contribution is denoted by  $\overline{\theta^2}$  and the turbulent contribution by  $\overline{\theta_{10}^2}$ .

Figures 14 through 19 show that although the turbulent transport compares quite favorably for these two models, there is considerably more kinetic energy near the surface and near the inversion in the more correct two-dimensional model. The deficiencies of the one-dimensional model appear to reflect the difficulty of modeling with an isotropic turbulent macroscale. It is clear from the two-dimensional simulation as it is from field observations [18] that at both the top and bottom of the domain, the characteristic horizontal scale of the turbulence is much larger than the characteristic vertical scale. It appears that the next step in improving the model calls for incorporating some structural shape in the scale representation [19].

## Appendix

### Model Equations

The model equations of motion for an incompressible fluid in the presence of both a gravitational and a Coriolis body force, with the mean variables denoted by capitals and the turbulent fluctuations by lower-case, may be written in general tensor notation as follows.

$$\frac{\partial U_i}{\partial t} + U_j \frac{\partial U_i}{\partial x_j} = - \frac{\partial \overline{u_i u_j}}{\partial x_j} - \frac{1}{\rho} \frac{\partial P}{\partial x_i} + g_i \frac{(\Theta - \Theta_0)}{\Theta_0} - 2 \epsilon_{ijk} \Omega_j U_k$$

$$\frac{\partial U_i}{\partial x_i} = 0$$

$$\frac{\partial \Theta}{\partial t} + U_j \frac{\partial \Theta}{\partial x_j} = - \frac{\partial \overline{u_j \theta}}{\partial x_j}$$

$$\begin{aligned} \frac{\partial \overline{u_i u_j}}{\partial t} + U_k \frac{\partial \overline{u_i u_j}}{\partial x_k} = & - \overline{u_i u_k} \frac{\partial U_j}{\partial x_k} - \overline{u_j u_k} \frac{\partial U_i}{\partial x_k} + g_i \frac{\overline{u_j \theta}}{\Theta_0} + g_j \frac{\overline{u_i \theta}}{\Theta_0} \\ & - 2 \epsilon_{ikl} \Omega_k \overline{u_l u_j} - 2 \epsilon_{jlk} \Omega_k \overline{u_l u_i} \\ & + 0.3 \frac{\partial}{\partial x_k} \left( q \Lambda \frac{\partial \overline{u_i u_j}}{\partial x_k} \right) - \frac{q}{\Lambda} \left( \overline{u_i u_j} - \delta_{ij} \frac{q^2}{3} \right) - \delta_{ij} \frac{q^3}{12 \Lambda} \end{aligned}$$

$$\begin{aligned} \frac{\partial \overline{u_i \theta}}{\partial t} + U_j \frac{\partial \overline{u_i \theta}}{\partial x_j} = & - \overline{u_i u_j} \frac{\partial \Theta}{\partial x_j} - \overline{u_j \theta} \frac{\partial U_i}{\partial x_j} + g_i \frac{\overline{\theta^2}}{\Theta_0} - 2 \epsilon_{ijk} \Omega_j \overline{u_k \theta} \\ & + 0.3 \frac{\partial}{\partial x_j} \left( q \Lambda \frac{\partial \overline{u_i \theta}}{\partial x_j} \right) - \frac{0.75 q}{\Lambda} \overline{u_i \theta} \end{aligned}$$

$$\frac{\partial \overline{\theta^2}}{\partial t} + U_j \frac{\partial \overline{\theta^2}}{\partial x_j} = - 2 \overline{u_j \theta} \frac{\partial \Theta}{\partial x_j} + 0.3 \frac{\partial}{\partial x_j} \left( q \Lambda \frac{\partial \overline{\theta^2}}{\partial x_j} \right) - \frac{0.45 q \overline{\theta^2}}{\Lambda}$$

$$\begin{aligned} \frac{\partial \Lambda}{\partial t} + U_j \frac{\partial \Lambda}{\partial x_j} = & 0.35 \frac{\Lambda}{q^2} \overline{u_i u_j} \frac{\partial U_i}{\partial x_j} + 0.75 q + 0.3 \frac{\partial}{\partial x_i} \left( q \Lambda \frac{\partial \Lambda}{\partial x_i} \right) \\ & - \frac{0.375}{q} \left( \frac{\partial q \Lambda}{\partial x_i} \right)^2 + \frac{0.8}{q^2} q_i \frac{u_i \theta}{\Theta_0} \end{aligned}$$

The overbar represents an ensemble average, and  $q^2 = \overline{u_i u_i}$ .

Along with the differing boundary conditions for the individual problems, an upper bound is placed on  $\Lambda$  depending upon the spread of the region of turbulence.

For the canopy flow example, variation with respect to one coordinate only is permitted. Also extra sink terms must be added to the equations for the mean variables, and both source and sink terms added to the Reynolds stress and heat flux equations (13). The other three examples permit dependence of variables on two coordinates. The flow may be either planar or axisymmetric.

**Acknowledgment** The example investigations discussed in this paper have been supported by the National Aeronautics and Space Administration, the Nuclear Regulatory Commission, the Electric Power Research Institute and the Naval Air Systems Command.

## References

1. C. duP. Donaldson: "Atmospheric Turbulence and the Dispersal of Atmospheric Pollutants", in *Proceedings of Workshop on Micrometeorology*, American Meteorological Society, ed. by D. A. Haugen (Science Press, 1973) pp. 313-390.
2. W. S. Lewellen: "Use of Invariant Modeling", in *Handbook of Turbulence*, Vol. I, ed. by W. Frost, T. H. Moulden (Plenum Publishing Corp., 1977) pp. 237-280.
3. M. E. Teske, W. S. Lewellen: "Turbulent Transport Model of a Thunderstorm Gust Front", in *Proceedings of 10th Conference on Severe Local Storms*, American Meteorological Society, Omaha, NE, Oct. 18-21 (1977).
4. W. S. Lewellen, M. E. Teske, H. Segur: "Turbulent Transport Model of Wind Shear in Thunderstorm Gust Fronts and Warm Fronts", NASA CR 3002 (1978).
5. M. E. Teske, W. S. Lewellen: "The Prediction of Turbulence and Wind Shear Associated with Thunderstorm Gust Fronts", in *Proceedings of Conference on Atmospheric Environment of Aerospace Systems and Applied Meteorology*, American Meteorological Society, New York, NY, Nov. 14-16 (1978).
6. J. S. Turner: *Buoyancy Effects in Fluids* (Cambridge University Press, Great Britain 1973).
7. W. S. Lewellen, M. E. Teske: "Turbulent Transport Model of Low-Level Winds in a Tornado", in *Proceedings of 10th Conference on Severe Local Storms*, American Meteorological Society, Omaha, NE, Oct. 18-21 (1977) pp. 291-298.
8. W. S. Lewellen, M. E. Teske, Y. P. Sheng: "Wind and Pressure Distributions in a Tornado", *Fifth International Conference on Wind Engineering*, Colorado State University, July 8-13 (1979).
9. W. S. Lewellen, Y. P. Sheng: "Influence of Surface Conditions on Tornado Wind Distributions", in *Proceedings of the 11th Conference on Severe Local Storms*, American Meteorological Society, Kansas City, Missouri, Oct. 2-5 (1979).
10. N. R. Wilson, R. H. Shaw: A higher order closure model for canopy flow, *J. Appl. Meteorol.* 16, 1197-1205 (1977).
11. R. H. Shaw, G. den Hartog, K. M. King, G. W. Thurtell: Measurements of mean wind flow and three-dimensional turbulence intensity within a mature corn canopy, *Agric. Meteorol.* 13, 419-425 (1974).
12. R. H. Shaw, R. H. Silversides, G. W. Thurtell: Some observations of turbulence and turbulent transport within and above plant canopies, *Boundary-Layer Meteorol.* 5, 429-449 (1974).
13. W. S. Lewellen, Y. P. Sheng: "Modeling of Dry Deposition of SO<sub>2</sub> and Sulfate Aerosols", A.R.A.P. Rpt. No. 410, (1979).
14. R. A. Brown: *Analytical Methods in Planetary Boundary-Layer Modeling* (Wiley and Sons, New York, NY, 1974) pp. 94-108.
15. M. E. Teske, W. S. Lewellen: "Horizontal Roll Vortices in the Planetary Boundary Layer", in *Proceedings of Fourth Symposium on Turbulence, Diffusion, and Air Pollution*, American Meteorological Society, Reno, NE, Jan. 15-18 (1979) pp. 456-463.
16. R. A. LeMone: Modulation of turbulence energy by longitudinal rolls in an unstable planetary boundary layer, *J. Atmos. Sci.* 33, 1308-1320 (1976).
17. J. W. Deardorff: Numerical investigation of neutral and unstable planetary boundary layers, *J. Atmos. Sci.* 29, 91-115 (1972).
18. J. C. Kaimal: Horizontal velocity spectra in an unstable surface layer, *J. Atmos. Sci.* 35, 18-24 (1978).
19. G. Sandri: "Recent Results Obtained in the Modeling of Turbulent Flows by Second-Order Closure", A.R.A.P. Rpt. No. 332 (1978).